

Diffuse Reflectance Spectroscopy of Human Colon Tissue

by

George I. Zonios

B.S., Physics (1990)
University of Ioannina, Greece

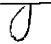
SUBMITTED TO THE DEPARTMENT OF
PHYSICS
IN PARTIAL FULFILLMENT OF THE
REQUIREMENTS FOR THE DEGREE OF
DOCTOR OF PHILOSOPHY

at the



Massachusetts Institute of Technology
June, 1998

© 1998 Massachusetts Institute of Technology
All rights reserved

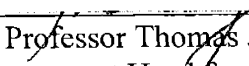
Signature of Author:

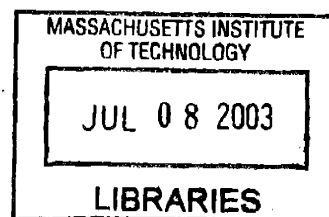
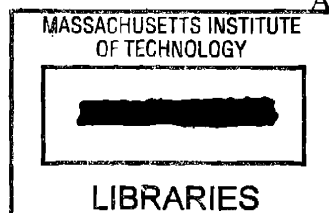
 Department of Physics
May 14, 1998

Certified by:

 
Michael S. Feld
Professor of Physics
Thesis Supervisor

Accepted by:


Professor Thomas J. Greytak
Associate Department Head for Education



ARCHIVES

Diffuse Reflectance Spectroscopy of Human Colon Tissue

by

George I. Zonios

Submitted to the Department of Physics
on May 1, 1998
in partial fulfillment of the requirements for the Degree
of Doctor of Philosophy in Physics

ABSTRACT

Diffuse reflectance spectroscopy can provide quantitative biochemical and morphological information for the analysis of biological tissue epithelium and the detection of precancerous lesions. To investigate this, diffuse reflectance spectra were collected from adenomatous colon polyps (cancer precursors) and normal colonic tissue of patients undergoing colonoscopy. To analyze the data, an analytical model was developed based on the diffusion of light in tissue. The model was formulated in terms of the absorption and scattering properties of tissue. In the case of absorption, hemoglobin was identified as the major absorber of light, and scattering was modeled as a homogeneous collection of spherical microparticles using Mie scattering theory.

The validity and accuracy of the analytical model was tested and validated on a physical tissue model (phantom) composed of polystyrene beads and hemoglobin and it was found that it is suitable for application to the tissue data. Four parameters were obtained by analyzing the tissue data using the model: hemoglobin concentration, hemoglobin oxygen saturation, effective scatterer density and size. Normal and adenoma tissue sites exhibited differences in hemoglobin concentration and effective scatterer size, in agreement with other studies which employ standard methods. These results demonstrate that diffuse reflectance can be used to obtain tissue biochemical and morphological information *in vivo*.

Thesis Supervisor: Michael S. Feld

Title: Professor of Physics

Acknowledgments

I would like to thank Michael Feld for his continuous guidance, and extraordinary enthusiasm and passion with which he has supported my activities during the course of this work. I have also benefited greatly by Lev Perelman's unique perspective and insight into the physics of this work. Thanks to Jacques Van Dam who made acquisition of the clinical data possible during several months of intensive effort. Ramachandra Dasari with his remarkable ability for "common sense" has also helped in every day life matters in the lab.

Renato Zangaro and Landulfo Silveira have helped with the instrumentation and the data acquisition process. Jim Crawford and Maryann Fitzmaurice provided the necessary advise and feedback for tissue pathology. Ramasamy Manoharan has also helped at various stages of this work.

Many others have provided help and support during my stay at the Spec Lab. Thanks to Jim Brennan for his friendship and support, especially during my first years in the lab, as well as to the other students, Nada Boustany, Marta Dark, Jun Wu, Andrew Berger, Changhuei Yang and Vadim Backman.

Finally, I would like to extend my gratitude and thanks to all those who have contributed to this work and I have neglected to mention here.

Contents

1. Introduction

1.1 Background & significance	7
1.2 Histology vs. spectroscopy.....	8
1.3 Biomedical spectroscopy & diffuse reflectance spectroscopy.....	10
1.4 Colon tissue histology.....	13
1.5 Basic physics & key elements of approach.....	18
1.6 Objectives & thesis outline.....	20

2. Tissue optics

2.1 Scattering.....	22
2.2 Refractive index.....	26
2.3 Absorption.....	27
2.4 Colon tissue optical parameters.....	31
2.5 Sampling depth.....	33

3. Instrumentation

3.1 Diffuse reflectance spectroscopy system.....	36
3.2 Optical probe.....	37
3.3 Data acquisition protocol.....	40

4. Diffuse reflectance theory

4.1 Diffuse reflectance.....	41
4.2 Radiative transfer equation & diffusion approximation.....	43
4.3 Exponential model.....	46
4.4 Photon migration model.....	52
4.5 Path integral formulation.....	53
4.6 Monte-Carlo method.....	55
4.7 Diffusion approximation – method of images.....	57
4.8 Model comparison.....	61
4.9 Optical fiber probe model.....	65

5. Investigations on tissue phantoms

5.1 Phantom construction.....	72
5.2 Absorption range.....	74
5.3 Scattering range.....	77
5.4 Optical probe response.....	79
5.5 Delivery/collection geometry.....	85
5.6 Angular dependence.....	87
5.7 Radial dependence.....	92
5.8 Hemoglobin oxygen saturation.....	96
5.9 Sampling depth.....	98

6. Data analysis

6.1 Exponential model.....	101
6.2 Optical probe model.....	106
6.3 Statistical analysis of model parameters.....	111
6.4 Discussion.....	114

7. Conclusions & future directions

7.1 Conclusions and thesis accomplishments.....	119
7.2 Application to other tissue types.....	120
7.3 Real time data acquisition & analysis - imaging techniques.....	121
7.4 Additional tissue information.....	123
7.5 Probe geometry.....	124
7.6 Fluorescence spectroscopy.....	125

Appendix

Derivation of the diffusion equation.....	126
---	-----

References	129
-------------------------	-----

CHAPTER 1

INTRODUCTION

1.1 Background & significance

Optical spectroscopy may be used to examine biomolecules and probe biological tissues and the collected spectra can be used to study a variety of issues. For instance, one can investigate the influence of the environment on molecular structure, identify a particular compound and its concentration in a mixture, or observe the dynamics of a biological system by tracking the movement of labeled cells or particles. The information obtained by spectroscopic techniques can have significant biomedical impact since it can provide clinically useful results.

The present study employs an optical spectroscopic method and was motivated by a key problem in medicine, namely the detection of morphological and biochemical alterations in biological tissues (especially the epithelial surfaces of the hollow body organs) which are related to the early stages of cancer formation. In the medical terminology, these alterations are often referred to as “Dysplasia” or “Neoplasia” and they constitute the stage that tissue undergoes before becoming frank cancer. The occurrence of these alterations is well-described in the internal (mucosal) surfaces of the hollow organs, including the gastrointestinal tract, the oral cavity, the urinary bladder, the cervix and the lungs. Development of methods to identify dysplasia is important because cancer is treated most effectively by abrogation of precancerous lesions. Cancer is currently the second leading cause of death in the US, with cancers originating in the surfaces of the hollow organs accounting for a quarter million deaths each year. It is

estimated that more than 90% of these could be prevented by early detection and treatment [American Cancer Society 1998]. As cancer is “invisible” at the earliest stages, it is important to develop efficient and reliable methods for detecting such early lesions. Diffuse reflectance spectroscopy has the potential to provide the means to identify precancerous lesions. In a broader sense, tissue information obtained through a spectroscopic technique could be useful in tissue classification and in the detection and characterization of a large number of pathologic disorders, including cancer.

1.2 Histology vs. spectroscopy

The most widely used method for the detection and classification of precancerous lesions in tissue is microscopic examination, i.e. histology. The process begins with biopsy, in which a few cubic mm of the tissue or organ are removed from the body with a specialized forceps. The biopsy sample is fixed in formaldehyde, embedded in paraffin, sliced into sections typically 5 microns thick, and stained with special dyes. The pathologist then analyzes these tissue sections under a microscope, looking for clues in architecture and cytology. The evaluation process relies heavily on pattern recognition. In the case of cancer diagnosis, features considered include the extent of structural (dis)organization, the size and shape of cell nuclei, the mitotic index (indicative of the rate of cell reproduction), and the presence of tumor necrosis.

Histology has become the gold standard for analysis of diseased tissue: it provides the “final” diagnosis, and is a key element in determining the therapeutic plan of action. However, the process is not without its limitations. First, biopsy involves removal of tissue, which breaches tissue barriers and is therefore quite invasive. Biopsy carries a certain risk of complications and, in addition, limits the amount of tissue available for study. Furthermore, once removed the tissue can undergo biochemical changes which can lead to artifacts. Sampling errors can be also significant. In many diseases, tissue involvement is non-uniform. In other cases, the diseased tissue is “invisible” to the physician taking the biopsies, which must then be taken at random locations. In such cases, only a tiny fraction of the suspected area is sampled, and the tissue obtained may

not be representative of the diseased area. In addition, there are issues of time and expense. Sample preparation takes hours at best, and can introduce artifacts. This severely constrains on-line applications, such as providing feedback during the course of an operation. And analyzing the specimens is manpower intensive -- the services of highly-trained histology technicians and MD pathologists are costly. But perhaps the most fundamental limitation of pathological evaluation is its largely qualitative nature -- it is partly science and partly art, even though in some instances quantitative information is available through histological techniques such as morphometry [Eide 1986, Tipoe and White 1995], or DNA ploidy analysis [Robey-Cafferty *et al* 1990]. Histological findings are inherently prone to interpretation bias, and expert pathologists evaluating the same tissue sample do not always come to the same conclusion. Needless to say, this is potentially disastrous, in view of the fact that pathological findings are crucial in making therapeutic decisions.

Spectroscopy has the potential to provide important information about tissue and thus become an important supplement to standard histological techniques. Light signals can be delivered and collected via optical fibers, so that all parts of the body can be accessed remotely through catheters, needles, cannulas and endoscopes. Information can thus be gathered *in situ*: instead of bringing the tissue to the instrument, a part of the instrument can be brought to the tissue. Healthy tissue can be left in place and only diseased tissue need be removed. Furthermore, data can be collected and analyzed in a fraction of a second, allowing the possibility of real-time feedback. In addition, spectroscopic signals can indicate biochemical changes, which often precede the morphological changes observed in histology. Moreover, spectroscopic techniques are amenable to creation of two and three dimensional images. But perhaps most important of all, the information provided by spectroscopy is quantitative, and thus it can bring an added degree of objectivity to the process of diagnosing disease.

1.3 Biomedical spectroscopy & diffuse reflectance spectroscopy

Various techniques of light spectroscopy can be used to study biologically tissue, and in particular the surfaces of the various parts and organs of the human body. Many of these techniques such as fluorescence, Raman, and diffuse reflectance have already been employed to study biological systems and tissues *in vitro* and *in vivo*. Each one has its own special features, advantages, and potential applications.

Fluorescence spectroscopy offers the advantage that it can directly probe the biochemical composition of tissues by means of detecting specific biomolecules (“fluorophores”) which emit characteristic fluorescence signals. One promising result from this type of spectroscopy is the observation of characteristic red fluorescence emission, reported for precancerous lesions and tumors [Cothren *et al* 1996, Panjehpour *et al* 1996, Loh *et al* 1993]. However, the origins of this red fluorescence and its connection to the pathologic state of tissue are not yet well understood. In addition, numerous biochemicals contribute to fluorescence generation in tissue, a fact that makes the task of decomposing the observed spectrum into its original components formidable. Furthermore, fluorescence is very sensitive to factors such as pH, temperature in addition to other uncontrollable physiological factors that introduce wide variability to the data.

Raman spectroscopy detects characteristic signatures of biomolecules using the principle of Raman scattering. This is an inelastic scattering process which depends on the vibrational energy level configurations of the biomolecule under study [Campbell and Dwek 1984]. Raman spectroscopy has the advantage that it is much more specific than fluorescence, with the tradeoff that the signal is several orders of magnitude weaker. Nevertheless, there is a considerable number of biomedical applications of this technique reported (see [Manoharan *et al* 1996] for a recent review) and it has been applied to perform quantitative histochemical analysis of normal and atherosclerotic human coronary artery with great success [Brennan 1995].

Diffuse reflectance spectroscopy is probably the simplest spectroscopy type of the three. Unlike the two types already mentioned, it does not probe the biochemical nature of tissue in a direct way, but it can be thought as an advanced way of doing a color

analysis, something that the human eye is capable of doing in a less sophisticated way. Color is a central quality through which we perceive the world, and it is also very important in routine medical practice where color is often used for diagnosis of disease. For instance, bright red skin may be indicative of burn or other inflammation, black stool may be indicative of bleeding, yellow in the skin and the eyes may be indicative of abnormal liver functioning etc. Since color depends on the scattering and absorption properties, diffuse reflectance yields information about these properties of the medium under study. Scattering and absorption information can be made available through the utilization of one of the other two spectroscopy methods mentioned earlier, but in that case it is entangled with additional biochemical information (i.e. fluorescence or Raman scattering spectra). In that sense, a good understanding of diffuse reflectance spectroscopy is important for the better understanding of more complicated techniques such as Raman or fluorescence.

Diffuse reflectance spectroscopy has therefore been chosen as the spectroscopic technique to be employed in this study, because of its simplicity, the direct way it probes tissue absorption and scattering, and the fact that the basic physics involved is an essential part of several other more elaborate spectroscopic techniques such as Raman and fluorescence. In diffuse reflectance spectroscopy, light is delivered to tissue and after several successive scattering and absorption events it re-emerges from the tissue surface where it may be collected and analyzed. Analysis of the collected light provides information regarding the optical properties of the medium under study, which can then be correlated with the morphology and the biochemical composition to provide information about the state of biological tissue.

To benefit from the advantages diffuse reflectance spectroscopy offers, a methodology is needed to connect the characteristic features of the measured spectra to the tissue biochemical and morphological information. Such a methodology would typically consist of two parts: (a) collection of the reflectance spectra with an optical probe with defined geometry, and (b) a model to parametrize the data and obtain quantitative information about the tissue. Several researchers have used steady-state diffuse reflectance spectroscopy in the study of biological tissues. Reports have been

published on the investigation of a variety of human and animal tissues, both *in vivo* and *in vitro*. Semi-empirical models have been utilized to measure blood content and hemoglobin oxygen saturation, in rat gastric mucosa [Sato *et al* 1979], and rat pancreas [Knoefel *et al* 1996]. Differences in the diffuse reflectance of rat brain were characterized on a purely empirical basis [Ikeda and Matsushita 1980], and empirical analysis was also employed in the study of human tissues *in vivo*, such as skin [Marchesini *et al* 1991], bladder [Mourant *et al* 1995], and colon [Mourant *et al* 1996]. The results of these studies are encouraging and render the technique a very promising tool, but none of these employed an analytical physical model to describe light propagation in tissue and to obtain calibrated quantitative information.

The simple physical principles upon which diffuse reflectance spectroscopy is based, facilitates the development of physical models to analyze the data. Such models, often based on the diffusion approximation to the radiative transfer equation, have been employed to provide quantitative results in blood oximetry [Schmitt 1991, Takatani and Ling 1994], and in the study of the optical properties of various animal tissues such as rat prostate [Arnfield *et al* 1988], chicken breast [Kienle *et al* 1996], and canine gut [Takatani and Graham 1979]. The main characteristic of these models is their mathematical complexity which makes inversion difficult -- a process which is nevertheless required to obtain the tissue optical parameters from the measured diffuse reflectance spectra.

This study employs a physical model which is capable of providing quantitative information regarding the basic biological tissue optical properties i.e. light scattering and absorption. The model is based on the diffusion approximation to the radiative transfer equation, and is formulated in such a way so that it can be easily inverted to obtain the tissue optical properties, using the diffuse reflectance spectra as input. The validity and accuracy ranges of the model were investigated on tissue phantoms with known optical properties, prior to the analysis of tissue data. This insured that the results present a realistic picture of the optical properties of the tissues under study.

The goal of this work was to assess the potential of diffuse reflectance spectroscopy to provide information which can be used for biochemical and morphological analysis of

mucosal tissues *in vivo*. To investigate this premise, we have studied normal colon mucosa, and adenomatous colon polyps which are precursors of colon cancer. These polyps are usually readily identifiable by visual inspection, but histologically they are similar to visually undetectable precancerous lesions such as flat dysplasia, and thus we have chosen them as a test ground for this spectroscopic technique. We examine here how the results of our analysis correlate with standard histological examination, how they may be ultimately useful for the early detection of disease, and most importantly, how a spectroscopic tool can be applied *in vivo* to obtain morphological and biochemical information.

The following section briefly presents basic information about the histology and morphology of the colon tissues studied. This information is key to interpreting the information that the tissue diffuse reflectance spectra provide.

1.4 Colon tissue histology

The human colon develops a polypoid form of dysplasia known as adenoma, which is considered the precursor of most colon cancers. Colonic adenomas, whose morphology is illustrated in figure 1.1 [Haggitt *et al* 1985] are readily identifiable during endoscopic surveillance and can be used as a test ground to evaluate the potential of diffuse reflectance spectroscopy to diagnose disease. Colon cancer is the second largest cause of cancer-related deaths in the US (about 50,000 per year [American Cancer Society 1993]). Early detection of the precancerous lesions could lead to the effective prevention of most of these deaths.

Since the objective of the work is to obtain histological information based on the analysis of the diffusely reflected spectroscopic signals of tissue, a brief review of colon morphology is presented here, which is found in more detail standard gastroenterology texts [Ming and Goldman 1992, Fenoglio-Preiser *et al* 1989]. The various layers of the colon wall, including the top three, which are the mucosa, the underlying submucosa, and the muscularis propria, are shown in figure 1.1. The total combined thickness of the normal colon wall is approximately 5 mm. Since at wavelengths of interest (visible)

light penetrates about 0.5 mm into the tissue, the analysis presented in this thesis will be mostly concerned with the top two layers: the mucosa and submucosa.

The mucosal layer is a castellated surface containing “crypts”, tubular structures of narrow diameter and considerable length lined with epithelial cells (illustrated in the

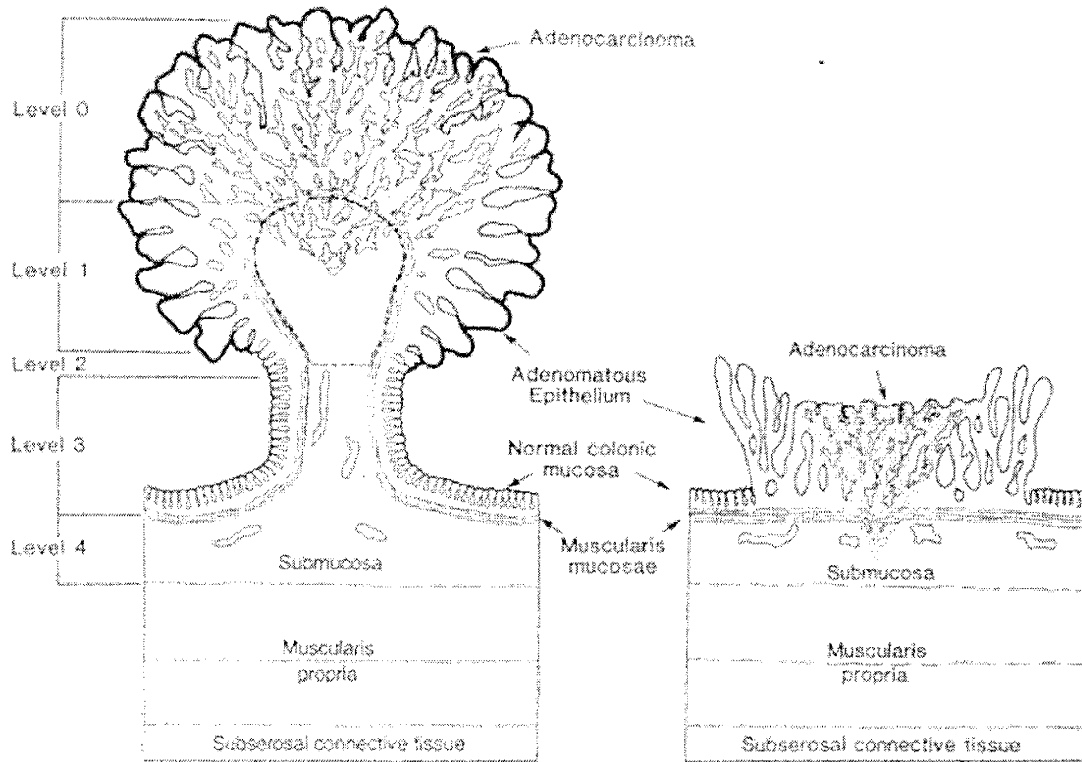


Figure 1.1: Microscopic architecture of human colon tissue (from [Haggit *et al* 1985]). Two types of precancerous formations are shown: pedunculated adenomatous polyp (left) and sessile adenoma (right). Normal colonic mucosa is also shown near the root of the adenomas. In addition, the various layers of the colon are illustrated. Adenomas, which can be in a benign state for several years, cause eventually cancer (marked as adenocarcinoma near the top). The size of the pedunculated polyp is approximately 7 mm in this figure, and the thickness of the mucosa layer approximately 0.5 mm. Only pedunculated adenomas were examined in this study.

“Normal Colonic Mucosa” region of figure 1.1). The crypts are supported by a matrix called the lamina propria, largely composed of a delicate framework of collagen-rich connective tissue containing interstitial fluid, a normal complement of inflammatory cells, fibroblasts and smooth muscle cells, eosinophils (a type of white blood cell frequently found in tissue), and arterioles, capillaries, and venules. The submucosa layer is also composed of a more dense collagenous connective tissue, but is admixed with

blood vessels, fat, and nerves, and contains no epithelial cells. A thin horizontal layer of smooth muscle cells, the muscularis mucosa, separates the mucosa and submucosa.

Normal mucosa has a thickness of approximately 0.5 mm. As dysplasia develops, the neatly arranged crypts become disorganized and irregular in shape and size (area marked as “Adenomatous Epithelium”). The crypts proliferate and crowd out the connective tissue. In addition, in response to the increased demand for oxygen, new microvessels are generated. Mucosal dysplasia manifests itself in two forms, pedunculated (polypoid) and sessile (flat) (Both shown in figure 1.1). The term “adenoma” is applied to both forms of dysplastic foci. In an adenoma, the crypt cells usually proliferate upwards (or vertically), creating a small lesion which can grow to several millimeters in diameter as diagrammed in figure 1.1. In a pedunculated adenoma, the lesion develops a stalk and literally “hangs” into the bowel lumen. In a sessile adenoma, the lesion remains bulky and flat, and proliferates sideways (radially). Except for this, the two forms are histologically identical and eventually lead to cancer (area marked “Adenocarcinoma” in figure 1.1). However, flat dysplasia is macroscopically similar to normal mucosa, and hence is extremely difficult to detect by endoscopy. Surveillance of flat dysplasia would be an important application of a spectroscopic technique such as diffuse reflectance. This study, investigated the diffuse reflectance spectroscopy of pedunculated polyps which can be identified easily and employed these as a test site for flat dysplasia.

Within the mucosal layer, exists a dense network of capillary blood vessels which surround the crypts and provide the necessary oxygen to the cells. The capillary vessels contain red blood cells, which in turn contain hemoglobin, a protein capable of transporting oxygen. Hemoglobin exhibits strong light absorption bands in the visible range of the spectrum, and its presence in tissue will be a key factor in the formulation of a physical model for diffuse reflectance. It is therefore important to briefly describe the blood vessel configuration in normal colon mucosa, and the changes occurring when adenomatous polyps form.

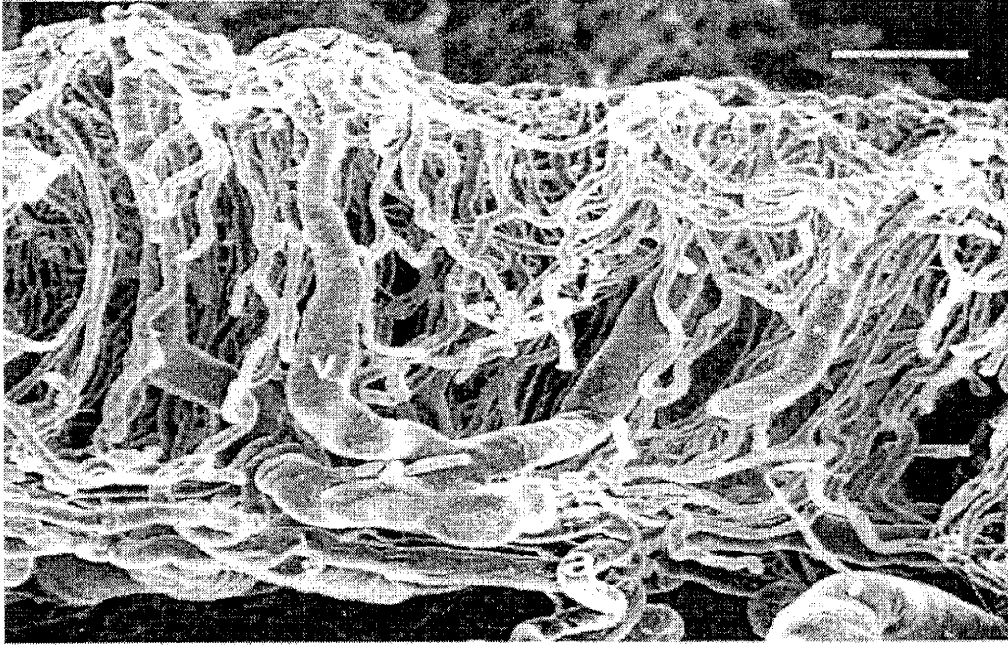


Figure 1.2: Scanning electron microscope picture of the blood vessel network of the normal human colon mucosa (cross section), made possible using vascular casting techniques (from [Skinner and O'Brien 1996]). Approximately 50% of the vessel volume is occupied by red cells containing hemoglobin. This high concentration and characteristic absorption bands in the visible, make hemoglobin the most significant absorber of light for this tissue. Note the vessels becoming wider deeper in tissue (bar in upper right, 100 μm).

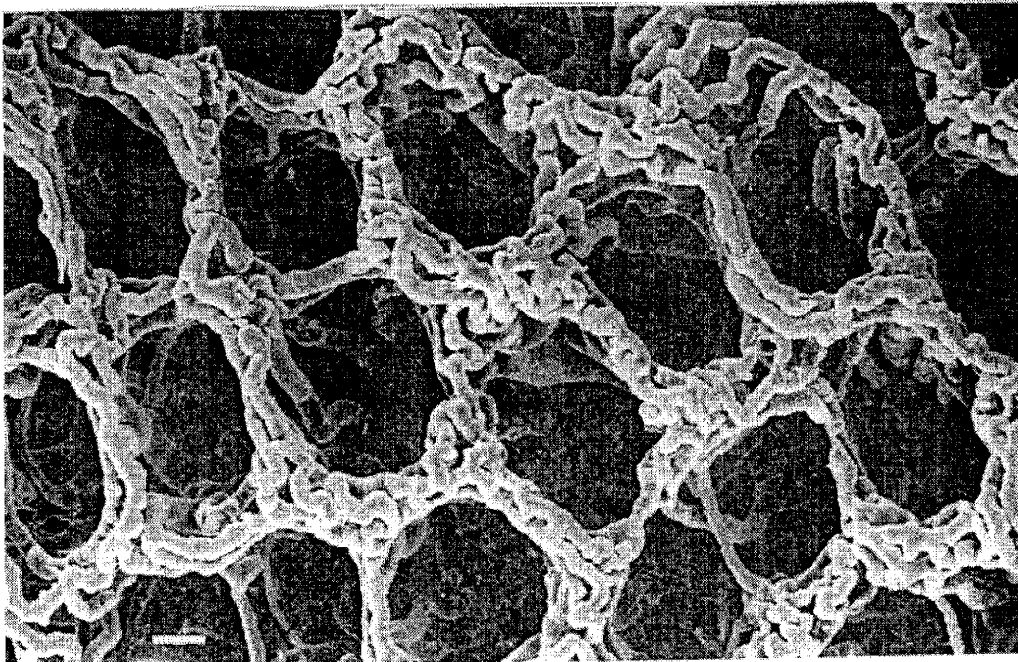


Figure 1.3: Top view of the capillary blood vessel network of normal human colon as viewed from the tissue surface [Skinner and O'Brien 1996]. The capillaries form a regular pattern around the crypts which contain the cells (bar, 40 μm).

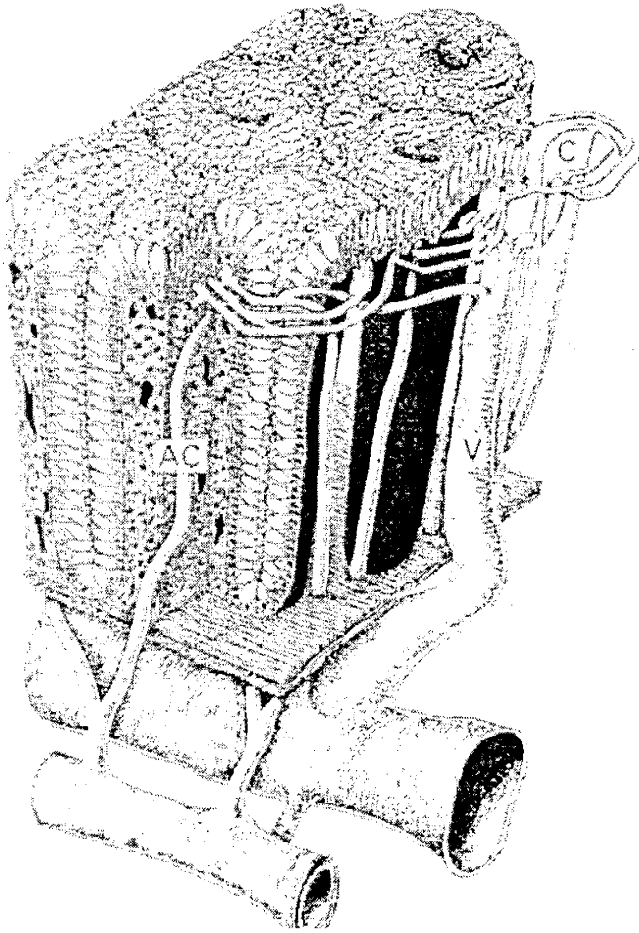


Figure 1.4: Schematic representation of the normal colon mucosa, showing the long narrow structure (crypts which contain the cells), and part of the blood vessel network (from [Araki *et al* 1996]). The thicker blood vessels are located in the submucosa layer.

wide so that red blood cells just fit inside, and usually travel in a sequence, one after the other (this facilitates transport of oxygen to surrounding tissue through diffusion). Blood vessels become larger deeper in tissue in the submucosa layer. Since light mostly propagates in the top two layers, it will be greatly affected by the hemoglobin absorption. Figure 1.3 [Skinner and O'Brien 1996] shows a top view the capillary vessel network. Capillaries form a periodic pattern surrounding the crypts which contain the cells.

Figure 1.4 [Araki *et al* 1996] shows a side view schematic of the normal colon mucosa. The structure of the capillary network is illustrated, together with the crypt

Figure 1.2 [Skinner and O'Brien 1996] shows a side view of the capillary network of the normal colon mucosa and submucosa. This is a scanning electron microscope picture, with the blood vessel network isolated by employing vascular casting techniques according to which blood is drained from tissue and the blood vessels are filled with a resin at pressure equal to that of blood under physiological conditions. After the resin hardens, the surrounding tissue is removed with chemical treatment, leaving a 3-dimensional cast of the blood vessel network, including the capillaries. The bar in the upper left corner indicates a scale of 100 μm . The majority of the capillary vessels in the mucosa are approximately 10 μm

configuration in the mucosal layer. This nice arrangement and configuration begins to break down in adenomatous polyps where blood vessels become disorganized and variable in size and shape [Skinner *et al* 1995] and are characterized by increased density and diameter. The same holds true, in general, for the crypts and other structures found in the mucosa. One the objectives of this study was to quantitatively measure some aspects of this organization/disorganization using diffuse reflectance spectroscopy.

1.5 Basic physics & key elements of approach

Based on the material and the discussion presented so far, it has become clear that there is a tremendous need for a methodology that can analyze human tissue, avoiding the standard drawbacks and disadvantages of techniques commonly employed. Moreover, diffuse reflectance spectroscopy has been identified as such a methodology, which probes the basic optical properties of tissue, namely elastic scattering and absorption. To further utilize this type of spectroscopy and arrive at the desired objective, which is the extraction of tissue information, a physical model is needed to describe the diffuse reflectance spectra measured on tissue.

To describe the diffuse reflectance, we are going to use the radiative transfer equation which describes light propagation in turbid media. In particular, because we are going to deal with diffusive light, we are going to employ the well-studied diffusion approximation to the radiative transfer equation which, along with the appropriate boundary condition, is capable of describing diffuse reflectance from tissues. Nevertheless, as is common practice in physics, straightforward application of theory does not always solve the problem. A key part of the model-building process is the careful examination of the fundamental aspects of the physical system under study, and the identification of the appropriate approximations which will enable a simple and effective description. This is particularly true in the case of biological tissue where the enormous biological complexity makes the task of building an explicit and detailed model based on direct application of theory, formidable.

Because of this overwhelming complexity, empirical and qualitative analysis techniques are often employed in the field of tissue light spectroscopy. In this study, which examines human colon tissue, we have made two fundamental approximations which formed the foundation of our analysis technique and served as the connection between diffusion theory and basic tissue biochemical and morphological parameters. The first approximation was the important new observation which identified hemoglobin as the only significant absorber in the visible range. This permitted the parametrization of the model in terms of the total hemoglobin concentration and the hemoglobin oxygen saturation which are both important physiological indicators. Secondly, the scattering properties of tissue were modeled as if due to a homogeneous system of spherical particles with known refractive index. This allowed (through the use of Mie scattering theory) the characterization of the tissue scattering properties by means of two parameters: an effective scatterer size, and an effective scatterer density.

Another important physical aspect of our approach, is the use of an optical fiber probe with a particular delivery/collection effective separation. Due to the basic physics of the problem, the particular choice of the probe diameter acted as a “ruler” which enabled the successful independent determination of the scattering and absorption coefficients of tissue. The fact that the characteristic spectrum of the only tissue absorber was known, was also a key element of the analysis which enabled this independent determination. This was implemented by noting that the tissue scattering spectra and the hemoglobin absorption spectrum (which was assumed known), were characterized by significantly different spectral features.

This simple physical picture allowed the analysis of the spectra and the determination of four parameters which were then quantitatively related to tissue biochemical and morphological characteristics. Furthermore the parameters were then related to the presence of disease.

1.6 Objectives & outline of thesis

As it has become evident from the above discussion, diffuse reflectance spectroscopy is a promising tool for the investigation of biological tissues. The objective of this work is twofold: (a) to investigate the optical properties of normal and precancerous colon tissues *in vivo*, and (b) to examine how the knowledge of the optical properties can be used in obtaining biochemical and morphological information about the tissue. The strategy adopted to achieve the above objectives is outlined below in four basic steps.

(i) Diffuse reflectance spectra were collected *in vivo* using an optical probe for delivery and collection of the light. The probe provided a fixed geometry and enabled collection of data in a controlled and reproducible way.

(ii) An analytical model was subsequently developed, based on light diffusion in tissue, to parametrize the data in terms of basic optical properties of the tissues under study, and to enable measurement of these parameters in a quantitative way. The using an analytical model of diffuse reflectance based on diffusion of light in tissue. To facilitate this task, some fundamental approximation were made regarding the origins of scattering and absorption in colon tissue.

(iii) The analytical model was validated and calibrated on materials which simulated the optical properties of tissue (tissue phantoms). Construction of the tissue phantoms followed the basic approximation made regarding the origins of colon tissue scattering and absorption.

(iv) Following validation on tissue phantoms, the model was applied to the clinical data and was used to measure the absorption and scattering coefficients of colon tissue which were then connected with morphological and biochemical properties such as hemoglobin concentration and oxygenation and average scatterer density and size. These results were finally correlated with standard histological examination of tissue, in order to assess the ability of the parameters obtained, to classify and characterize tissue.

The thesis is structured in the following way: In chapter 2 the basic concepts regarding optics of biological tissues are introduced. These include a brief review of

realistic tissue optical parameter ranges, and a small introduction to the nature and origins of absorption and elastic scattering processes in biological tissues. In particular, hemoglobin will be identified as the only significant absorber of light in the visible range of the spectrum, where this study was conducted. Chapter 3 describes the experimental methods, procedures, and protocols employed in collecting the data on human subjects *in vivo*, including the diffuse reflectance spectroscopy instrumentation, and the specially designed fiber optic probe. Chapter 4 discusses the various modeling approaches for describing light propagation and diffuse reflectance emission from tissue, as well as the development of the particular model which will be used to analyze the data. Chapter 5 describes the testing and validation of the model on tissue phantoms which were constructed from hemoglobin and polystyrene beads, based on the two fundamental assumptions made regarding diffuse reflectance i.e. (a) hemoglobin is the only significant absorber in colon mucosa, and (b) scattering can be modeled using a model of spherical scatterers. Chapter 6 presents the results obtained by applying the model to analyze the data. Finally chapter 7, discusses future directions and further developments stemming from the present study.

CHAPTER 2

OPTICAL PROPERTIES OF TISSUE

The optical behavior of biological tissue is in general characterized by significant elastic scattering and absorption. The magnitude of the scattering and absorption depends on the wavelength of light and can vary greatly across different wavelength ranges, especially in the case of absorption. This work is concerned with the optical properties of tissue mainly in the visible range of the electromagnetic spectrum (360-700 nm). The following sections provide more details on the nature and origins of the three most important optical properties of biological tissues: scattering, absorption, and refractive index. In addition, some relevant aspects of the basic physics related to scattering and absorption processes of visible light in tissue are briefly reviewed, and concepts such as the penetration and sampling depth of light are discussed. Finally, a brief review of the literature on the colon tissue optical parameters is given.

2.1 Scattering

Elastic scattering is probably the most prominent optical property of tissue. Typical values for the scattering coefficient, μ_s , for soft tissues, which can be thought of as the average number of scattering events per unit length, are in the range of $\mu_s = 10\text{-}100 \text{ mm}^{-1}$. This range of values indicates that light is scattered several tens of times per millimeter of path length traveled in tissue, and hence it quickly becomes diffusive. The angular dependence pattern of the scattering depends on the scatterer size/wavelength ratio.

Rayleigh scattering occurs when the scatterers are much smaller than the wavelength of light. In this case, the scattering pattern is isotropic i.e. independent of the scattering angle. When the scatterer size is much larger than the wavelength, scattering is highly forward directed. Scattering from tissue exhibits patterns falling in the middle of these two extremes, but it clearly shows a definite forward scattering pattern. This is probably characteristic of scattering arising from structures with an average size comparable to the wavelength of light.

The exact origins of scattering in tissue are not well known. Biological tissue is a complex and highly heterogeneous material, especially in a microscopic scale with typical dimensions comparable to the wavelength of visible light. Scattering arises from the microscopic variations and inhomogeneities of the refractive index which correspond to various scattering centers present in tissue. There are a number hypotheses identifying contributions to tissue scattering from various biological and biochemical microstructures, both extracellular such as collagen fibers [Ferdman and Yannas 1993, Leonard and Meek 1997], as well as intracellular such as mitochondria [Beauvoit *et al* 1994], cell nuclei [Perelman *et al* 1998], and possibly a large variety of other structures such as cell membranes [Meyer 1979].

The angular distribution of the scattering is described by the scattering phase function, $p(\theta)$, which gives the probability of a photon to be scattered at an angle θ , with respect to the initial direction of incidence. The phase function is normalized in a way such that $\int_{4\pi} p(\theta)d\omega = 1$ (with $d\omega$ denoting integration over solid angle ω). Several investigators [Van Gemert *et al* 1989, Jacques *et al* 1987] have reported that the Henyey-Greenstein (HG) phase function (equation (2.1.1)), originally introduced to describe scattering of light by interstellar matter [Henyey and Greenstein 1941], provides a satisfactory description of the angular patterns arising from tissue scattering,

$$p(\theta) = \frac{1}{4\pi} \frac{1 - g^2}{(1 - g^2 + 2g \cos \theta)^{3/2}} \quad (2.1.1)$$

with g being is the average cosine of the scattering angle, defined as follows:

$$g = 2\pi \int_0^\pi p(\theta) \cos\theta \sin\theta d\theta. \quad (2.1.2)$$

Even though the HG phase function has been extensively used for modeling light scattering in biological tissues, it should be kept in mind that it was used on a purely empirical basis and it is only an approximation to the real phase function whose exact form is not well known. Researchers often use with success other types of phase functions to describe biological tissue scattering such as that of gaussian type [Perelman *et al* 1994].

The parameter g is very frequently used to indicate how strongly forward directed the scattering is. Typical values for tissue are in the range $g=0.7-0.95$ corresponding to average scattering angles between 45 and 20 degrees respectively. Figure 2.1 shows the angular scattering patterns of the Henyey-Greinstein function with $g=0.0$ (isotropic) and $g=0.90$ (typical for tissue). The scattering pattern becomes more forward directed as $g \rightarrow 1$.

One other important parameter which is often used to indicate the amount of scattering present in tissue, is the reduced scattering coefficient, μ'_s , which is defined as $\mu'_s = \mu_s(1 - g)$, and thus incorporates effects introduced by the anisotropic nature of scattering. It essentially remaps the anisotropic scattering to the isotropic scattering case, since modeling of an anisotropic scattering process (such as the

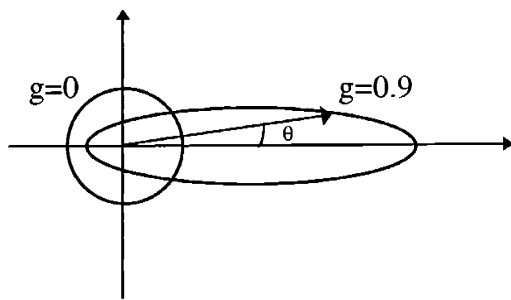


Figure 2.1: Henyey-Greinstein scattering phase function showing the angular pattern of scattering in polar coordinates. Two different patterns are shown corresponding to isotropic scattering ($g=0$), and strongly forward directed scattering ($g=0.9$). The latter case is representative of scattering in biological tissues.

total diffuse reflectance – discussed in chapter 4) in a medium with scattering coefficient, μ_s , and anisotropy g , is equivalent to modeling an isotropic

scattering process with scattering coefficient $\mu'_s = \mu_s(1-g)$. In this way, scattering anisotropy does not explicitly appear in the equations, but it is combined together with the scattering coefficient μ_s in one quantity, the reduced scattering coefficient, μ'_s . This is very appropriate and convenient for modeling multiple scattering processes, where light quickly becomes diffusive and information about the scattering anisotropy of isolated scattering events is therefore lost. Modeling of diffuse reflectance is one such example. The entire discussion in this thesis will not be explicitly concerned with the anisotropy effects of scattering; these effects will be implicitly included in the reduced scattering coefficient, μ'_s , which will be the main parameter of interest in terms of scattering. Typical values of μ'_s for soft biological tissue are in the range $0.5 < \mu'_s < 5.0 \text{ mm}^{-1}$.

As mentioned earlier, tissue scattering is thought to arise from microstructures with characteristic size. The problem of scattering of a plane electromagnetic wave by homogeneous spherical objects is known as Mie theory, and has been well studied [Born and Wolf 1975, Wiscombe 1979]. Mie theory will be used in the following chapters to model tissue scattering, and also to calculate the scattering properties of tissue phantoms consisting of spherical polystyrene particles. Mie theory provides an exact solution for scattering of light with wavelength, λ , by a spherical object with diameter, d , and refractive index, n , placed in a surrounding medium with refractive index n_o . While the vast majority of tissue scatterers are not expected to be spherical, both intuition and experimental evidence [Zerull 1976] indicate that with averaging over orientation and/or size, nonspherical particles scatter very much like “equivalent” spheres, so that Mie theory can be applied. This observation will be of major importance in modeling tissue scattering as we will see in chapter 4.

The final Mie solution which is an expression for the differential scattering cross section, is function of two independent quantities: (a) the ratio of the particle circumference to the wavelength of light $\pi d/\lambda$ (with λ measured in the surrounding medium), and (b) the ratio of the particle refractive index to the refractive index of the surrounding medium, n/n_o . Evaluation of the solution requires in general numerical

calculations. A published numerical code was used in all the Mie calculations reported in this thesis [Wiscombe 1979].

2.2 Refractive index

As mentioned above, microscopic scale variations of the refractive index, are responsible for the scattering properties of biological tissue. Tissue has an extremely complex biochemical composition, but its main component is water (typically 80% by volume [Woodward and White 1986]) which has a refractive index slowly varying from $n=1.331$ at 700 nm, to $n=1.339$ at 400 nm [Hale and Querry 1973], and thus sets the lower bound for the corresponding values expected for the refractive index of tissues. The refractive index of a wide variety of biological tissues (both animal and human) has been measured by employing an equally wide variety of techniques such as total internal reflection [Bolin *et al* 1989], phase contrast microscopy [Beuthan *et al* 1996], optical coherence tomography [Tearney *et al* 1995], and scattering goniometry [Ferdman and Yannas 1993]. In most cases, the refractive index, was found to be between 1.35 and 1.45, in the visible range [Bolin *et al* 1989, Duck 1990] except in some special cases such as tooth enamel for which it was found to be higher than 1.6. This indicates that scattering arises from refractive index variations within the 1.35-1.45 range i.e. relative refractive index changes (scatterer/background) usually smaller than 1.07.

Phase contrast microscopy techniques have enabled a research group [Schmitt and Kumar 1996] to show that the structure of the refractive index inhomogeneities in a variety of mammalian tissues resembles a pattern of frozen turbulence. Such an observation may be proven useful in the understanding of the origins and special properties of light scattering by tissue. Nevertheless, in this thesis, tissue will be assumed homogeneous, characterized by certain refractive index which represents in a way the average of all the real fluctuations.

2.3 Absorption

Absorption is measured by means of the absorption coefficient, μ_a , which represents the amount of absorption present in units of inverse length. Water, being the major component of soft tissues has negligible absorption in the visible range ($<10^{-4} \text{ mm}^{-1}$) [Hale and Querry 1973]. Tissue absorption, which is in general a function of the wavelength of light, is due to a number of characteristic biochemical molecules. Proteins and DNA exhibit strong absorption bands in the UV range (below 300 nm), but present negligible absorption in the visible range [Campbell and Dwek 1984], in which range tissue absorption is normally smaller than scattering and it is mainly due to hemoglobin. Typical values for the absorption coefficient in the visible range are $0.005 < \mu_a < 5 \text{ mm}^{-1}$. Note that this range spans three orders of magnitude in comparison to the scattering coefficient range spans one order of magnitude only.

Hemoglobin is omnipresent in almost all types of human tissue, because its main function is the transportation of oxygen from the lungs, which is essential for the metabolism and normal functioning of all living tissue. In addition to hemoglobin, melanin is also an important absorber in the visible range [Anderson *et al* 1981], but it is found only in the skin. Other biochemical compounds with characteristic light absorption in the visible range, such as bilirubin, β -carotene, cytochrome $\alpha\alpha_3$, and others [Campbell and Dwek 1984], are usually present in biological tissues in concentrations several orders of magnitude lower than that of hemoglobin so that their relative absorption is negligible. In this study, hemoglobin will be treated as the major absorber of light in colon tissue. Because of the central role of hemoglobin, the following paragraphs describe the most important properties of the hemoglobin molecule in more detail, with emphasis on the light absorption properties which are of central interest here.

The hemoglobin molecule [Stryer 1995] is a tetramer consisting of four folded amino acid chains, two α -chains 141 amino acids long, and two β -chains 146 amino acids long. It is packed in a box-like structure with dimensions 6.4x5.5x5.0 nm and has a molecular weight of approximately 64,400. Each chain contains a heme group (a type of porphyrin) with an iron atom attached, capable of binding one oxygen molecule in a reversible

manner. Hemoglobin transports oxygen, carbon dioxide, and hydrogen ions between the lungs and the tissues and is contained in the red blood cells (erythrocytes) which have a characteristic disk-like shape with a diameter of approximately 7 microns.

Since amino acids and proteins in general do not absorb visible light, the heme group is responsible for the characteristic light absorption properties of hemoglobin in the visible and IR ranges of the spectrum, and hence for its characteristic red color. Hemoglobin is encountered in both the oxygenated (HbO_2) and deoxygenated (Hb) forms. The light absorption properties of these two hemoglobin types have been well studied [van Assendelft 1970] and their molar extinction coefficient spectra $\epsilon_{\text{HbO}_2}(\lambda)$, $\epsilon_{\text{Hb}}(\lambda)$ are shown in figure 2.2 (the extinction coefficient, ϵ , is defined as, $\epsilon = \mu_a / (c \ln 10)$, where c is the concentration in mmoles/liter).

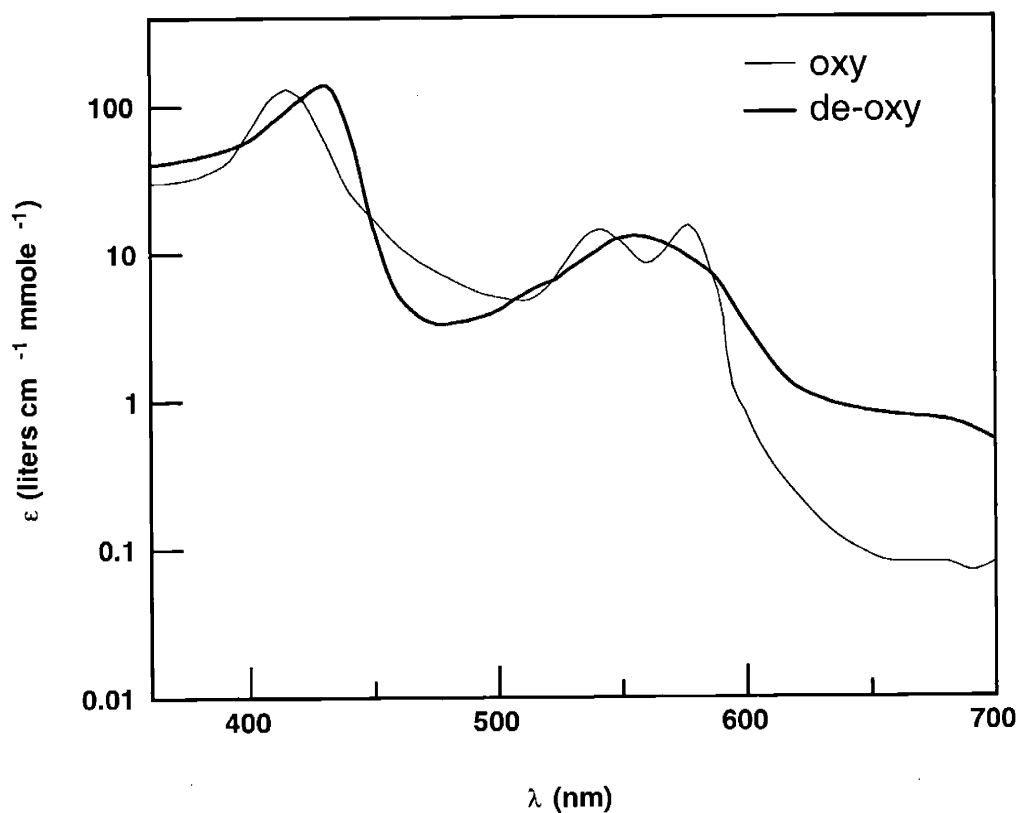


Figure 2.2: Molar extinction coefficient spectra per heme group of the oxygenated (thin line) and deoxygenated (thick line) hemoglobin molecule (from [van Assendelft *et al* 1970]). Note the characteristic peaks at 415, 542, and 577 nm (oxyhemoglobin) and at 430, 555 nm (deoxyhemoglobin).

Oxyhemoglobin absorption presents a maximum at 415 nm and two secondary maxima at 542 and 577 nm, while deoxyhemoglobin has an absorption maximum at 430 nm and only one secondary maximum at 555 nm. Both oxy and deoxy forms are present in tissue and the total absorption coefficient, $\mu_a(\lambda)$, can be expressed as a linear combination of the extinction spectra of the two hemoglobin types as follows:

$$\mu_a(\lambda) = 2.3c_{Hb}^* \left(\alpha \epsilon_{HbO_2}(\lambda) + (1 - \alpha) \epsilon_{Hb}(\lambda) \right) \quad (2.3.1)$$

where $\alpha = \frac{c_{HbO_2}}{c_{HbO_2} + c_{Hb}}$ is the hemoglobin oxygen saturation parameter, c_{HbO_2} and c_{Hb} are the concentrations of oxy and deoxy types respectively, and $c_{Hb}^* = c_{HbO_2} + c_{Hb}$, the total concentration of hemoglobin. In practice, other hemoglobin derivatives may be present (i.e. methemoglobin, carboxyhemoglobin etc.) but their concentrations are usually much smaller than those of the oxy and deoxy forms and can be safely ignored for the purposes of this study.

The hemoglobin oxygen saturation, α , which can be also defined as the fractional occupancy of all oxygen binding sites in a hemoglobin solution, is a function of the partial pressure of oxygen pO_2 . This is because the binding of oxygen by the hemoglobin molecule is a chemical equilibrium process obeying the following equation [Stryer 1995]



At very low oxygen pressure hemoglobin is mostly in the deoxygenated state, while at high oxygen pressure (typically > 100 torr) it is fully oxygenated. The dependence of the oxygen saturation on the partial pressure of oxygen is shown in figure 2.3, for hemoglobin contained in red blood cells under physiological conditions. The characteristic sigmoidal shape can be described by the Hill Equation (2.3.3) which follows from the chemical equilibrium expressed by equation (2.3.2) [Benedek and Villars 1974]

$$\alpha = \frac{(pO_2)^n}{(pO_2)^n + (p_{50})^n} \quad (2.3.3)$$

with p_{50} a constant. The exponent of $n=2.8$ is an empirical factor which depends on the cooperativity of the oxygen binding process by hemoglobin. If all four oxygen binding sites were operating independently, then the exponent n would be equal to 1. However, binding at one heme site facilitates oxygen binding at the other three sites, and this fact makes n larger (the maximum possible value is 4, equal to the total number of heme groups present in one hemoglobin molecule).

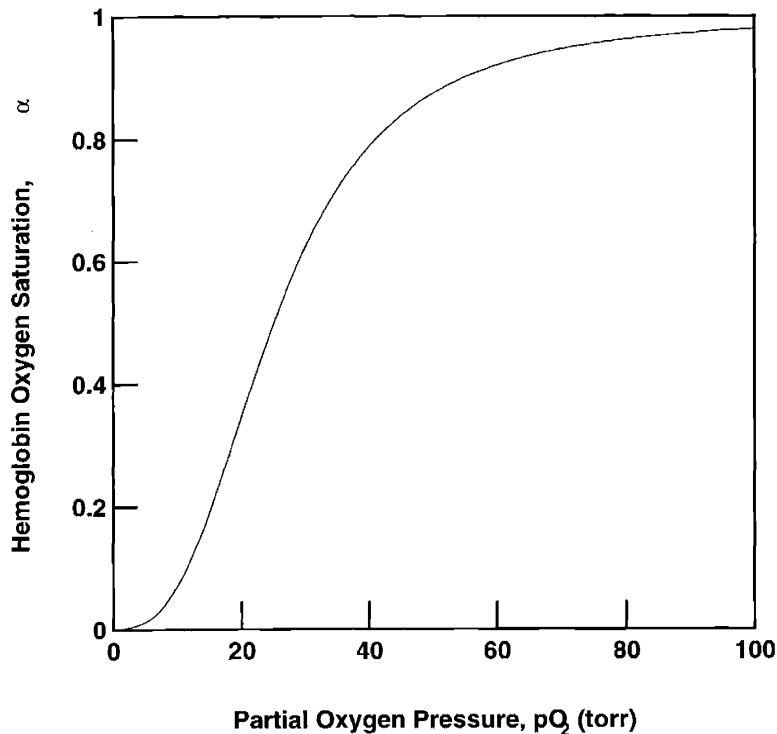


Figure 2.3: Oxygen saturation curve of hemoglobin (under physiological conditions). The ability of hemoglobin to bind oxygen depends on the partial pressure of oxygen present. Note the characteristic sigmoid shape of the curve.

The shape of the oxygen saturation curve shown in figure 2.3 also depends on a number of additional factors:

(i) pH: oxygen affinity increases with pH.

(ii) Temperature: oxygen affinity increases with decreasing temperature.

(iii) Organic Phosphates: approximately half of the total volume of the erythrocyte is occupied by 2,3 disphosphoglycerate which is an organic phosphate (DPG, also

known as BPG) which drastically reduces the oxygen affinity of hemoglobin. This reduction is proportional to the concentration of DPG, and because of the effect of DPG, hemoglobin oxygen affinity is much higher in free solution than it is when contained in red blood cells.

(iv) The presence of anions and carbon dioxide significantly affect the oxygen saturation curve.

Understanding of the hemoglobin oxygen saturation curve is important in the determination of the relative amounts of oxy and deoxy hemoglobin present in tissue, especially *in vivo*. Since these two hemoglobin forms present slightly different absorption spectra (figure 2.2), it is possible to distinguish them *in vivo* and determine their relative concentration by evaluating the total hemoglobin concentration, c_{Hb}^* , and the hemoglobin oxygen saturation SO_2 ($SO_2=100a$ %, $0 \leq a \leq 1$).

2.4 Colon tissue optical parameters

The optical parameters of colon tissue have not been previously investigated *in vivo*. There are however reports from two independent research groups who have measured the absorption and reduced scattering properties of colon tissue samples, *in vitro*. Such *in vitro* measurements are not necessarily similar to the ones expected *in vivo*, due to tissue sample preparation and handling (cutting, freezing/thawing, etc.), but it will be assumed here that they represent an acceptable ball-park estimate for the *in vivo* case. The *in vitro* results will thus be presented here as a first step in the exploration of the colon tissue optical properties.

The first group [Zonios *et al* 1996] measured the optical properties of both normal mucosa and adenomatous polyps. These measurements were performed by recording the total transmission and reflection spectra of 450 μm thick tissue samples in the range 300-700 nm, using a Shimadzu UV-265 spectrophotometer equipped with an integrating sphere (ISR-260, Shimadzu corp., Kyoto, Japan). The tissue optical properties were calculated by computing the Kubelka-Munk coefficients [Kubelka 1948], and by transforming these into transport theory absorption and reduced scattering coefficients, μ_a and μ'_s , respectively, using a model based on the solution of the 1-dimensional radiative transport equation [Van Gemert and Star 1987].

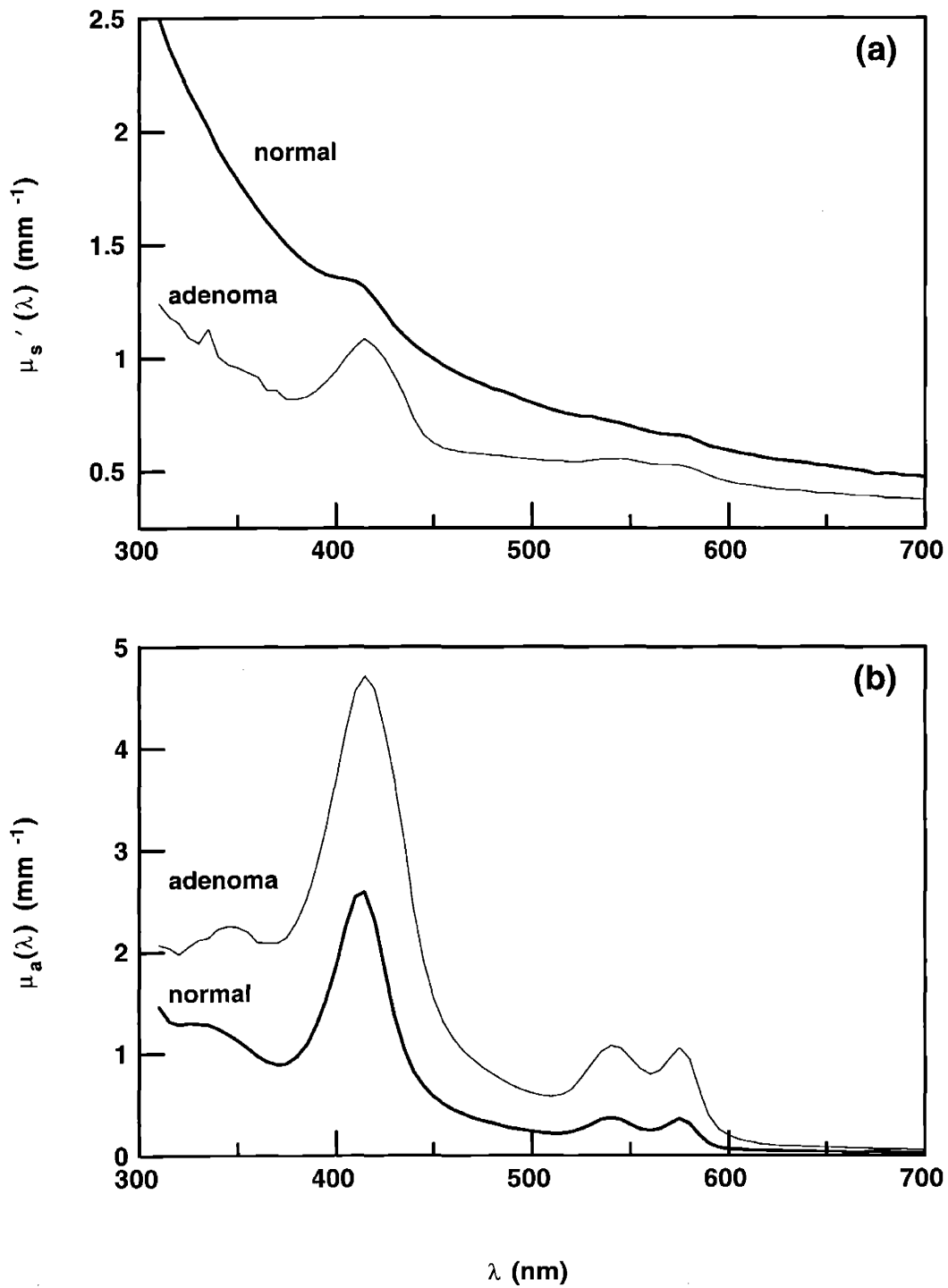


Figure 2.4: Average optical properties of normal colon mucosa and adenomatous polyps based on *in vitro* measurements (from [Zonios *et al* 1996]): (a) reduced scattering coefficient, (b) absorption coefficient. The absorption coefficient exhibits the characteristic features of hemoglobin absorption for both tissue types.

The results obtained are shown in figure 2.4. Figure 2.4(a) shows the average reduced scattering coefficient $\mu'_s(\lambda)$, and figure 2.4(b) the average absorption coefficient, $\mu_a(\lambda)$, for both tissue types. The shape of $\mu'_s(\lambda)$ is smooth, with no distinct peaks, with normal tissue exhibiting stronger scattering, and adenomatous polyps exhibiting stronger absorption. The absorption exhibits the characteristic peaks of oxyhemoglobin (main peak at 420 nm and two secondary peaks at 542 and 577 nm). The absorption peak at 420 nm exhibited by the adenomatous polyp scattering spectrum is a known artifact of the technique used to obtain these results [Van Gemert and Star 1987] which occurs when absorption is comparable to scattering.

The main observations from these results are as follows: (a) the reduced scattering spectra exhibit smooth spectral shapes with a relatively small (but nevertheless important) dependence on the wavelength, and (b) the absorption spectra exhibit the characteristic absorption bands of hemoglobin, along with a variation of approximately three orders of magnitude across the visible spectrum. These observations indicate that hemoglobin is probably the major absorber in both normal and adenomatous polyp colon tissues. In addition, absorption is consistently lower than scattering, and becomes comparable to scattering only near the peak of the hemoglobin absorption spectrum (~420 nm). These observations will be utilized as the starting point, in the development and formulation of the model to be applied for the analysis of the diffuse reflectance data, in the following chapters.

The second group [Marchesini *et al* 1994] studied normal colon mucosa only, employing similar methodology to calculate the optical properties. The results of that study are in good general agreement with the results of the first group and confirm the two main observation stated above.

2.5 Sampling depth

Knowledge of the penetration depth of light in tissue is very important because it signifies the tissue layers which diffusely reflected light probes, and therefore the

particular morphological and biochemical structures it interacts with. The penetration depth is extremely small in the far UV range (200-300 nm) where proteins and DNA exhibit strong absorption bands. In this range, absorption is much larger than scattering, which limits the penetration depth to within 10-50 μm below the tissue surface. In the visible range, which is the range employed in this study, scattering is the dominant optical property and the penetration depth is typically in the 0.1-0.5 mm range. This range is increased even more in the IR wavelength range (700-1000 nm), where absorption is minimal and light penetration is considerably increased.

The penetration of light in biological tissue is affected by the combined effects of scattering and absorption. Scattering has the effect to turn the light back and eventually force it to re-emerge from the surface as diffuse reflectance. Absorption on the other hand, limits the penetration depth in a straightforward way by exponentially attenuating the incident light as a function of depth in tissue. There is no exact way of defining the penetration depth d_0 , but if exponential attenuation of the incident light is assumed, due to scattering and absorption (which is clearly an approximation) it is possible to define the penetration depth as the depth where the intensity drops to $1/e$ of the initial intensity:

$$d_0 = \frac{1}{\mu'_s + \mu_a} \quad (2.5.1)$$

Despite the approximations made, equation (2.5.1) usually provides a good estimate of how deeply the light penetrates.

In the case of diffuse reflectance we are not interested in the penetration depth per se, but rather in the *sampling depth* i.e. the depth from where the collected diffusely reflected light comes from. Penetration and sampling depth are closely related, and just as in the case of the former, there is no unique way of defining the sampling depth because light follows a number of different random paths from the incident point, to the point where it exits the tissue. Given the entry and exit points of light though, it is possible to identify an average path, and in that way, to define the sampling depth. The average path

also known as *classical path*, can be calculated, in principle, using path integral techniques [Perelman *et al* 1994, Perelman *et al* 1997].

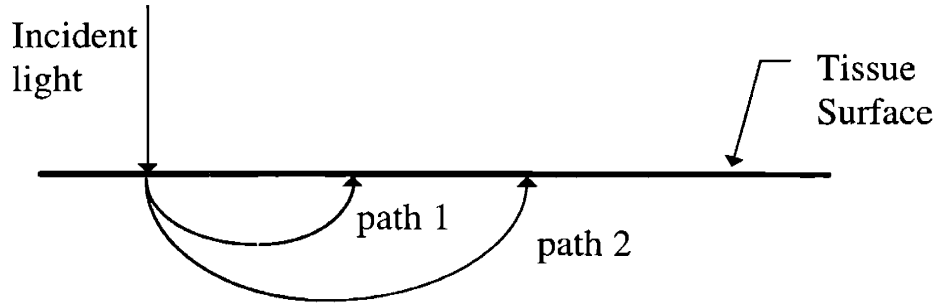


Figure 2.5: Average photon paths for two different entry/exit point configurations for diffuse reflectance. The sampling depth increases as the distance between the entry and exit points of light increases.

Figure 2.5 shows two such paths corresponding to two different separations between the entry and exit points of light. As this separation increases, the sampling depth of the light increases as well, but it never exceeds the actual penetration depth given by equation (2.5.1). For a realistic optical probe, such as the one used in this study, it is difficult and impractical to calculate the sampling depth using the path integral technique. Experimental measurements of the sampling depth of the probe will be presented in chapter 5. However, as we shall see in chapter 5 equation (2.5.1) provides a very good approximation of the sampling depth for the probe used here.

CHAPTER 3

EXPERIMENTAL METHODS

Diffuse reflectance spectra were collected *in vivo* on human subjects using an optical fiber probe. In this chapter, the experimental methods involved in collecting the *in vivo* data. Experimental methods related to tissue phantoms will be presented in chapter 5.

3.1 Diffuse reflectance spectroscopy system

The instrument used to collect the data in the clinical setting was capable of measuring both diffuse reflectance and multi-excitation wavelength fluorescence spectra [Zangaro *et al* 1996]. The part essential for the collection of the diffuse reflectance was employed in this study. Figure 3.1 shows a simplified block diagram of the system. The white light from a xenon-arc flashlamp (EG&G, FX-249) with approximately 10 μ sec pulse duration and an average energy of 4J/pulse, was coupled to a fiber optic probe (described in detail below) by means of a system of lenses, and delivered to tissue. The same probe collected the diffuse reflectance emerging from the tissue surface. The collected light was coupled to the entrance slit of an imaging spectrograph (Instruments SA CP-200 with 200 lines/mm grating blazed at 400 nm) which dispersed the light, and an electronically gated diode array detector (EG&G PAR OMA III, Model 1421) detected the light. Data were collected in the 360-685 nm spectral range, defined by the output intensity of the xenon lamp below 360 nm, and by the cutoff of the detector above

685 nm. The spectral resolution of the system was approximately 3.5 nm with an entrance slit of 0.25 mm. The detector offered the capability of electronic gating and a 12 μ sec gate time synchronized with the lamp pulse duration was used in order minimize spurious contributions from background light (endoscope illumination). The detector was controlled by a 486 PC notebook computer where the data were transferred and stored.

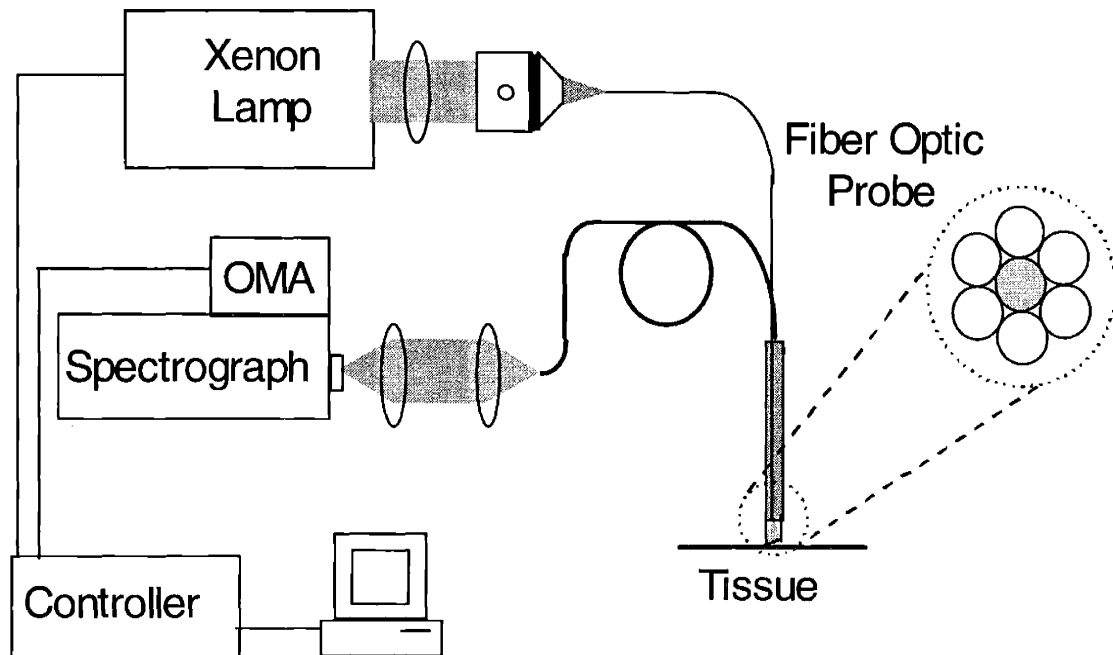


Figure 3.1: Schematic diagram of the instrument used to collect diffuse reflectance spectra. The system includes a xenon arc flash lamp as a white light source, a spectrograph/OMA system for spectral analysis, an optical fiber probe for light delivery and collection, and a PC computer for general control of the data acquisition process.

3.2 Optical probe

Light was delivered and collected by means of an optical probe [Cothren *et al* 1986, Brennan *et al* 1993] which was advanced through the accessory channel of the colonoscope until in contact with the tissue. The basic geometry of the probe is shown in figure 3.2. The probe consisted of a central optical fiber for light delivery and six fibers for collection, surrounding the delivery fiber in a circular manner. All optical fibers used were identical 200 μ m core multimode fibers with numerical aperture (NA) equal to 0.22

(acceptance angle approximately 15 degrees). The probe tip was fitted with a quartz shield approximately 1.5 mm in length and diameter. The function of the shield was to provide a fixed and reproducible geometry between the optical fibers and the tissue. In addition, the shield enabled larger delivery and collection areas as compared to the case where no shield is used. The delivery and collection spots had the form of overlapping cones with approximate radii of $r_d = 0.35$ mm and $r_c = 0.55$ mm respectively (figure 3.3). These radii depend on the NA of the optical fibers and the length of the shield which defines the distance from the tip of the fibers to the tissue surface. The tip of the optical probe was beveled at an angle of 17 degrees. This ensured that the unwanted specular reflections of the excitation light from the shield/air interface was not collected.

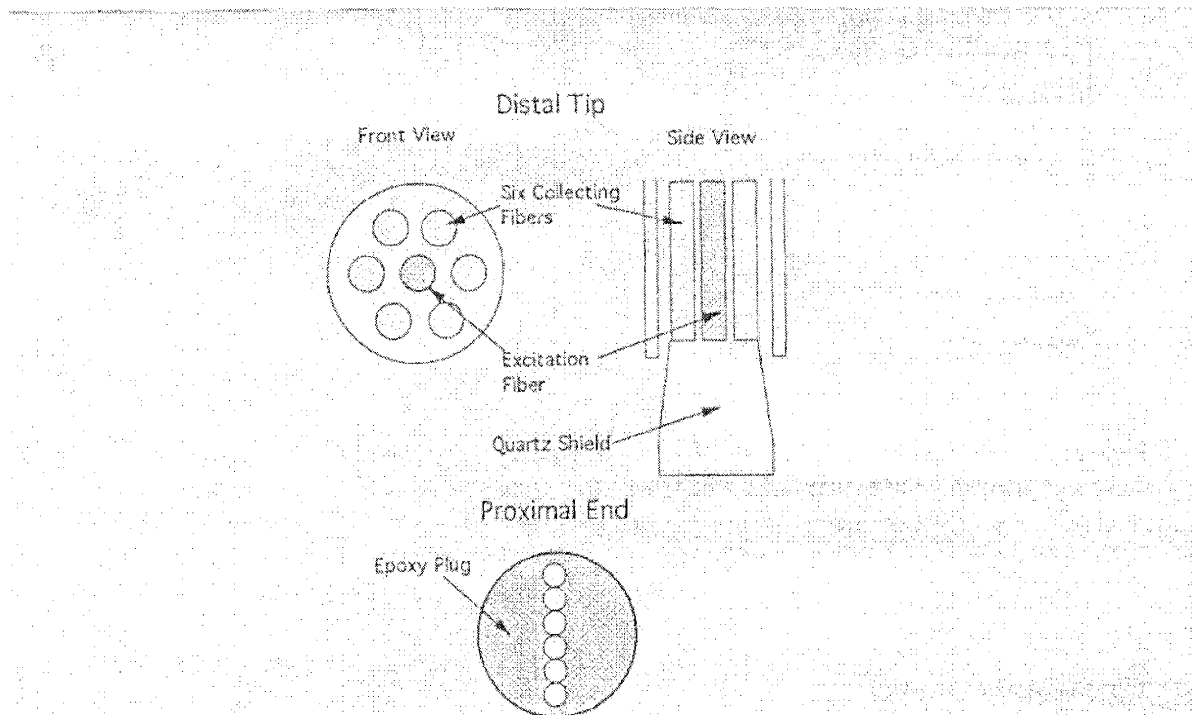


Figure 3.2: Schematic diagram of the proximal and distal ends of the fiber optic probe used to collect the data. Details of the fiber and the quartz shield configurations are shown. The distal tip consists of one central fiber for light delivery which is surrounded by six fibers for collection, and a quartz shield approximately 1.5 mm in length and diameter attached. All fibers are 200 μ m core, 0.22 NA.

The details of the probe delivery and collection geometry are shown in figure 3.3. Figure 3.3(a) shows a side view of the probe illustrating the delivery and collection areas

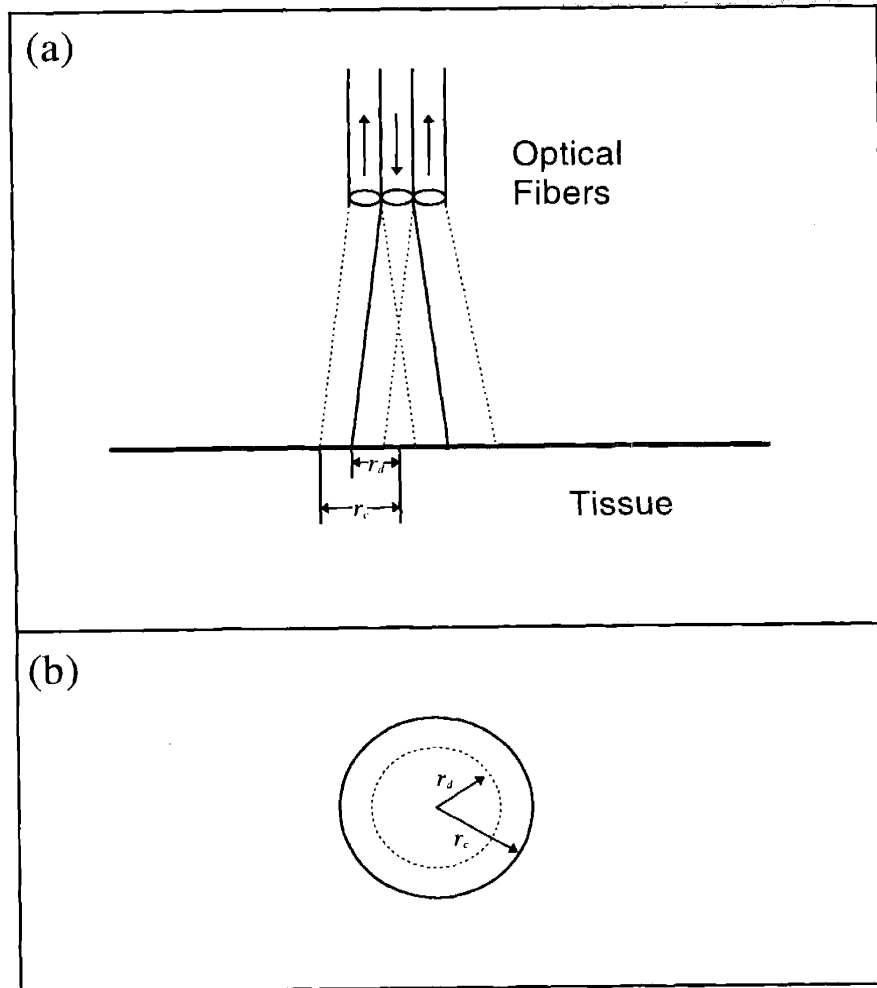


Figure 3.3: Delivery and collection geometry employed by the fiber optic probe. (a) Side view: The fiber tips are located approximately 1.5 mm above the tissue surface due to the presence of a quartz shield (not shown), resulting in concentric delivery and collection areas with radii r_d and r_c respectively, (b) Top view: The concentric delivery and collection areas are shown.

and figure 3.3(b) shows a top view of the same areas. It should be emphasized that the particular design of the optical probe which included the quartz shield, in addition to providing fixed and reproducible delivery/collection geometry, it also provided a controlled sampling depth. More details of the sampling depth characteristics of the optical probe will be discussed in section 5.9.

3.3 Data acquisition protocol

Diffuse reflectance spectra were collected *in vivo* from normal mucosa and adenomatous polyps in the colon of human subjects. The data were collected during routine endoscopy procedures carried out for cancer surveillance. Patients were selected in random with no preference in age, sex, previous medical history etc. After obtaining informed consent, a total of 45 patients were studied, with adenomatous polyps found in 13. Only data from patients with adenomatous polyps will be discussed in this thesis. Diffuse reflectance spectra were measured from a few different sites on every adenomatous polyp and from corresponding sites in the normal mucosa surrounding the polyp. Single-pulse excitation was used in order to avoid motion artifacts. All of the polyps studied were subsequently removed and examined histologically, while the normal mucosa sites were not histologically examined.

The diffuse reflectance spectrum of a 20% by volume BaSO₄ powder suspension was used as a reference, to take into account the spectral characteristics and overall intensity of the xenon lamp light, and the system response. The probe was immersed in the suspension so that reproducible geometry could be achieved every time, and a reference diffuse reflectance spectrum was recorded prior to collection of each data set. Tissue spectra were subsequently normalized by means of division by this reference spectrum. In this way, diffuse reflectance was always measured in units of the standard BaSO₄ diffuse reflectance which is an isotropic reflector following Lambert's law [Ditchburn 1976], and has a uniform flat response over the entire visible spectrum [Kortum 1969].

CHAPTER 4

DIFFUSE REFLECTANCE THEORY

The subject of this chapter is the various physical modeling approaches which may be employed to describe the diffuse reflectance of tissue. A model appropriate for application to the tissue data should be capable of implementing the particular delivery and collection geometry of the light, defined by the optical probe used. In order to develop such a detailed model the basic physical principles of the diffuse reflectance process will be first presented, and will be used then as a starting point for the model development. During investigation of the basic physics of the diffuse reflectance process, a number of different techniques in approaching the problem will be discussed. The advantages and disadvantages of these techniques will be reviewed, and finally, a model will be developed suitable for the tissue data analysis.

4.1 Diffuse reflectance

The basic geometry of the problem is shown in figure 4.1. Light is incident on the surface of tissue which is approximated as a homogeneous turbid medium with absorption and reduced scattering coefficients, μ_a and μ'_s , respectively. The tissue is also characterized by a refractive index n . Part of the incident light is absorbed in tissue, while the non-absorbed part is subject to multiple scattering events and eventually emerges from the surface as diffuse reflectance. The problem here is to develop a physical model which gives the diffuse reflectance as a function of the optical properties of tissue, taking

into account the specific geometry for the delivery and collection of light which are implemented by means of a fiber optic probe.

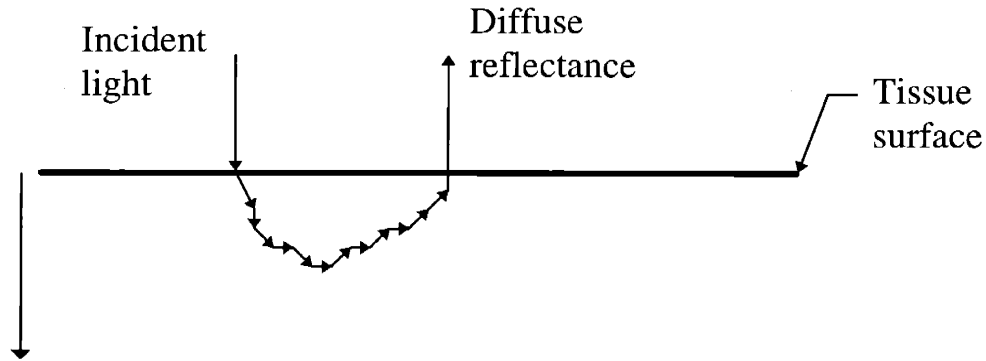


Figure 4.1: Typical physical picture of the diffuse reflectance process. Light is incident on tissue (modeled as semi-infinite homogeneous turbid medium) and after several successive scattering events the part of it which escapes absorption re-emerges from the tissue surface.

In modeling diffuse reflectance, the basic assumption is made that the tissue is made up of a semi-infinite homogeneous layer. This is clearly an approximation, because it is well known that biological tissues are in general inhomogeneous and are composed of distinct layers, with different morphological characteristics and different optical properties. However, the homogeneous single-layer approximation simplifies the analysis and since the typical penetration depth of light in tissue is approximately 0.5 mm in the visible range, this analysis yields an average measurement of the optical properties within the first one half millimeter below the tissue surface. This is where precancerous changes usually arise, so this is a good approximation for the purposes of this study.

In the case of the total diffuse reflectance, R_t , from a semi-infinite turbid i.e. the diffuse reflectance collected over the entire infinite extent of the surface, it can be easily shown that $R_t = R_t(\mu'_s / \mu_a)$ i.e. the total diffuse reflectance is a function of the ratio of the reduced scattering and absorption coefficients only. This is due to the *scale invariance* of the problem which can be checked in the following way. Assume that all dimensions of the problem are scaled by the same constant factor. The diffuse reflectance should remain in such a case invariant. When collection extends to infinity however, as in the case of R_t , infinity cannot be scaled and the only way for R_t to remain invariant is for it to be a function of the ratio μ'_s / μ_a only.

The use of an optical probe measuring diffuse reflectance, R_p , with a typical light collection radius, r_p , breaks the scale invariance of the problem, and introduces an explicit dependence on the reduced scattering coefficient, such that $R_p = R_p(\mu'_s / \mu_a, \mu'_s r_p)$. In this way, the use of an optical probe permits the separation of the diffuse reflectance dependencies on scattering and absorption. The goal is thus to develop a model for the probe diffuse reflectance, R_p . Application of this model to the data, should allow calculation of the optical parameters of the tissue under study. In order to develop a model which provides the diffuse reflectance from a semi-infinite medium, the basic physical process of light propagation in a scattering and absorbing medium must be modeled. The starting point in describing light propagation, is the radiative transport equation discussed in the following section.

4.2 Radiative transfer equation & diffusion approximation

The radiative transfer equation describes light propagation in turbid media. The time-independent form of the equation is given by

$$\hat{s} \cdot \nabla I(\vec{r}, \hat{s}) = -(\mu_s + \mu_a)I(\vec{r}, \hat{s}) + \mu_s \int_{4\pi} p(\hat{s}, \hat{s}')I(\vec{r}, \hat{s}')d\omega' + \epsilon(\vec{r}, \hat{s}) \quad (4.2.1)$$

where $I(\vec{r}, \hat{s})$ is the specific intensity i.e. the power per unit area, per unit solid angle, ($\text{W m}^{-2} \text{sr}^{-1}$), $p(\hat{s}, \hat{s}')$ is the scattering phase function (differential scattering cross section) which gives the probability of a photon incident in the direction, \hat{s}' , to be scattered in the new direction, \hat{s} , μ_s and μ_a , are the scattering and absorption coefficients, respectively, and $\epsilon(\vec{r}, \hat{s})$ is an external light source. The phase function obeys the following normalization condition

$$\int_{4\pi} p(\hat{s}, \hat{s}')d\omega' = 1. \quad (4.2.2)$$

The physical picture of the radiative transport equation is straightforward and is illustrated in figure 4.2. The specific intensity $I(\vec{r}, \hat{s})$ at point, \vec{r} , and direction, \hat{s} , within the cylindrical elementary volume shown, is decreased due to losses from scattering and absorption (first right hand side term), increased due to light scattered back into that region from outside (second right hand side term), and also increased by direct contributions from external light sources (third right hand side term). The photons are treated as billiard balls undergoing elastic scattering, with wave interference effects not explicitly taken into account (averaging out of these effects is assumed). Even though the physical picture of equation (4.2.1) is simple, the equation itself is difficult to solve; there is no known general solution, and it can be usually solved only numerically. Analytical solutions have been found for special conditions and approximations. One such analytical approximation is the diffusion approximation, discussed further below.

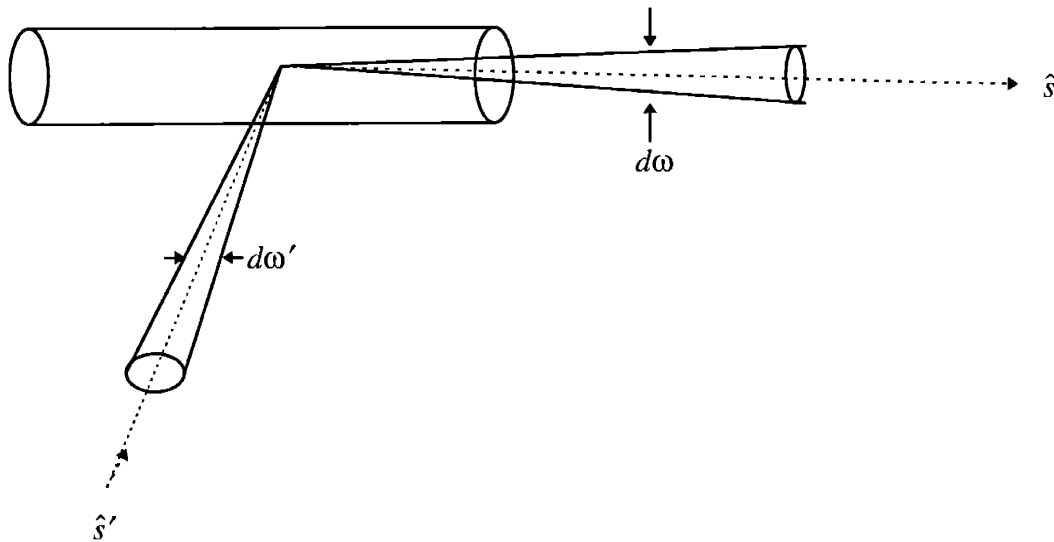


Figure 4.2: Physical picture of the radiative transport equation. Light intensity in an elementary cylindrical volume is decreased due to absorption and scattering in the direction \hat{s} , and increased due to external scattering in the direction \hat{s}' .

The diffusion approximation has been extensively studied and applied to various radiative transfer problems [Morse and Feshbach 1953, Ishimaru 1978]. Under this approximation, the specific intensity, $I(\vec{r}, \hat{s})$, is assumed to be composed of a large

diffusive part which is isotropic i.e. has no angular dependence and is proportional to the energy density, $\phi(\vec{r})$, plus a small flux term, $\vec{F}(\vec{r})$, such that

$$I(\vec{r}, \hat{s}) = \frac{1}{4\pi} \phi(\vec{r}) + \frac{3}{4\pi} \vec{F}(\vec{r}) \cdot \hat{s} \quad (4.2.3)$$

Substituting equation (4.2.3) into equation (4.2.1), assuming for simplicity $\epsilon(\vec{r}, \hat{s})=0$, multiplying both sides by \hat{s} , and integrating over the solid angle yields

$$\vec{F}(\vec{r}) = -D\nabla\phi(\vec{r}) \quad (4.2.4)$$

with $D = \frac{1}{3(\mu_a + \mu'_s)}$. Note that equation (4.2.4) is analogous to Fick's law [Benedek and Villars 1974] for diffusion processes. Taking the divergence of (4.2.4) and using the following definition for the flux $\vec{F}(\vec{r})$

$$\vec{F}(\vec{r}) = \int_{4\pi} I(\vec{r}, \hat{s}) \hat{s} d\omega \quad (4.2.5)$$

the diffusion equation is obtained (see the Appendix for a detailed derivation including the steps omitted here),

$$\nabla^2\phi(\vec{r}) - \mu^2\phi(\vec{r}) = 0 \quad (4.2.6)$$

with

$$\mu^2 = 3(\mu'_s + \mu_a)\mu_a = \mu_a/D. \quad (4.2.7)$$

The diffusion equation, along with the appropriate boundary condition dictated by the geometry of the problem, may be solved to provide information for the energy density, $\phi(\vec{r})$. The diffuse reflectance can then be calculated from (4.2.4), as the flux exiting the

surface. More detailed discussion of the diffusion approximation as applied to modeling the diffuse reflectance from a semi-infinite turbid medium will be given in section 4.7. A brief but instructive review of alternative methods for calculating the total diffuse reflectance will be given first.

4.3 Exponential model

The simplest way to approach the problem of calculating the total diffuse reflectance, R_t , from a homogeneous semi-infinite turbid medium is by assuming that the incident and backscattered light are exponentially attenuated according to the sum of the absorption and reduced scattering coefficients ($\mu_a + \mu'_s$). Even though this approximation essentially ignores the integral term in the radiative transfer equation (4.2.1), it is well known [Kubelka 1948, Ishimaru 1978] that solutions of this type (exponential) are a good approximation to the radiative transport equation, especially in 1-dimensional geometries. The price paid for the simplicity of this approximation is that the parameters (μ'_s, μ_a) must be replaced with a different set of scattering and absorption parameters which are related to the initial transport parameters in a complicated way. However, let us attempt to use the initial parameters (μ_a, μ'_s) here, and discuss later how these should be modified in order to account for the approximations made.

Figure 4.3 illustrates the geometry of the problem. A semi-infinite turbid medium is considered with $z=0$ defined on the surface and absorption and reduced scattering coefficients μ_a, μ'_s respectively. Light is incident on the surface of the medium and starts propagating inside it ($z>0$) subject to scattering and absorption. The intensity of the incident light is assumed to be exponentially attenuated i.e. $I = I_0 e^{-(\mu_a + \mu'_s)z}$. At a given depth z , light is scattered back from a thin layer with thickness dz . The backscattered light is assumed proportional to the reduced scattering coefficient μ'_s , and it is also exponentially attenuated by a factor $e^{-(\mu_a + \mu'_s)z}$ when it reaches the surface. In such a way, the total diffuse reflectance can be calculated by integrating over all depths, z , in the medium:

$$R_t = 2\mu'_s \int_0^{\infty} e^{-2(\mu'_s + \mu_a)z} dz = \frac{\mu'_s}{\mu'_s + \mu_a} \quad (4.3.1)$$

The factor of two is inserted so that $R_t=1$ when $\mu_a \rightarrow 0$. Equation (4.3.1) exhibits the correct dependence on the absorption/scattering ratio, which is dictated by the scale invariance of the problem. In addition it also has the correct behavior in the limit of very high absorption where the reflectance tends to zero, and in the limit of very low absorption where reflectance tends to unity (the normalization here is such that the diffuse reflectance is defined as the ratio of the light exiting the medium, to the incident light – in the absence of absorption all incident light eventually returns back as diffuse reflectance, which is hence equal to unity).

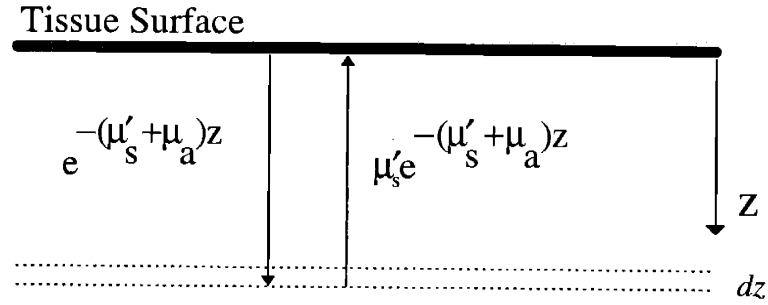


Figure 4.3: Geometry of the exponential diffuse reflectance model. Intensity of the light propagating in tissue is exponentially attenuated according to the sum of the reduced scattering and absorption coefficient.

However, despite the correct dependence on the ratio of the optical properties, and the correct behavior at the extreme limits, equation (4.3.1) produces abnormally high values for the total diffuse reflectance when compared with other accurate solutions such as the Monte-Carlo method (section 4.6). This discrepancy can be empirically corrected by introducing a scaling factor, k , for the reduced scattering coefficient. If the substitution $\mu'_s \rightarrow k\mu'_s$ is made with $k \cong 1/13$ [Wu *et al* 1993a], then equation (4.3.1) becomes

$$R_t = \frac{k\mu'_s}{k\mu'_s + \mu_a} = \frac{1}{1 + k \frac{\mu_a}{\mu'_s}} \quad (4.3.2)$$

Following this correction, equation (4.3.2) gives reasonable values for the diffuse reflectance in the range of optical parameters which is of interest in biological tissues (i.e. $\mu'_s / \mu_a = 1-1000$). The reason why μ'_s required rescaling, is related to the initial approximation employed in deriving equation (4.3.1). It is also interesting to note that even though such a non-trivial approximation to the radiative transfer equation was made, it was possible to obtain an expression for the diffuse reflectance which is characterized by the correct physical behavior, and which gives the correct values by employing only a simple fix.

Equation (4.3.2) is valid in the case of refractive index match conditions between the turbid medium and the surrounding medium. The surrounding medium is usually air, with refractive index approximately equal to unity. The refractive index of soft tissue is approximately 1.4, as discussed in section 2.2, and thus a refractive index mismatch boundary is defined by the tissue surface in realistic situations. It is possible to derive a general expression that relates the total diffuse reflectance under index-mismatched conditions, to that under index-matched conditions. Such a generalization can be implemented in equation (4.3.2) through the constant, k , which is in such a general case a function of the refractive index.

Let's assume that the tissue has refractive index, n , and that the diffuse reflectance is normalized to unity as discussed above (equation (4.3.1)). Due to the index mismatched conditions, part of the light which is internally incident on the boundary with angles larger than a critical angle, $\theta_c = \sin^{-1}(\frac{1}{n})$, with respect to the vertical on the surface, will be reflected back into the medium. This is equivalent to having an additional external source of light with intensity equal to that of the internally reflected light, which in turn generates additional diffuse reflectance, part of which is internally reflected to create a new source, and so on. Figure 4.4 illustrates this process. The total diffuse reflectance,

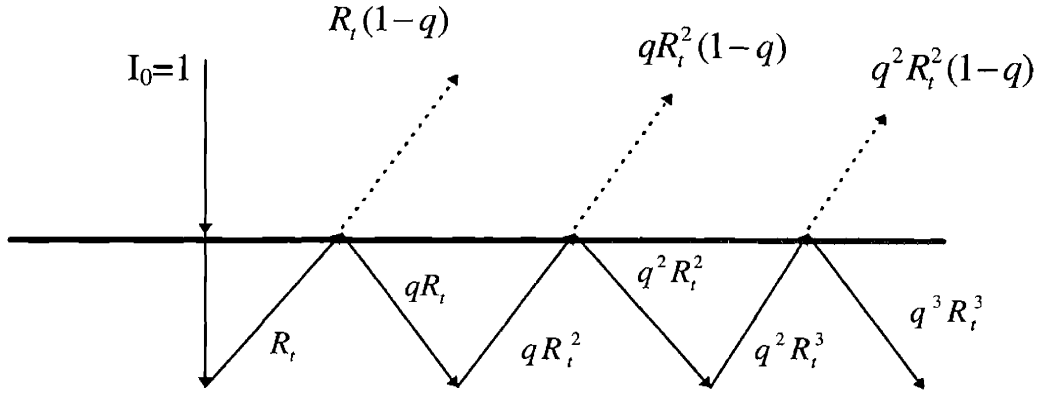


Figure 4.4: Calculation of the diffuse reflectance under refractive index mismatch conditions. The sum of the infinite steps of this process gives the total diffuse reflectance under refractive index mismatch conditions. R_t is the diffuse reflectance under index match conditions, and q is the part of the internally reflected light.

R_m , for the index-mismatched case may then be obtained in terms of the index-matched total diffuse reflectance, R_t , and the fraction, q , of the diffuse reflectance which is internally reflected [Lekner and Dorf 1988]

$$\begin{aligned}
 R_m &= R_t(1-q) + qR_t^2(1-q) + q^2R_t^3(1-q) + \dots \\
 &= R_t(1-q)(1 + qR_t + q^2R_t^2 + \dots) \\
 &= \frac{(1-q)R_t}{1 - qR_t}
 \end{aligned}
 \tag{4.3.3}$$

It is possible to calculate q by making the assumption that the light incident on the inner boundary has an isotropic specific intensity (hence the $\cos\theta$ term in the following equation, see discussion of Lambert's law in section 5.6); q is then given by

$$q = 2 \int_{\theta_c}^{\pi/2} \cos\theta \sin\theta d\theta = 1 - \frac{1}{n^2}
 \tag{4.3.4}$$

Since some light is reflected back even for angles smaller than the critical angle, θ_c , more accurate calculations must be performed. Exact values for the parameter q have been calculated and tabulated taking into account all relevant effects. Such a more

accurate expression is given by [Egan and Hilgeman 1979] in terms of the following empirical fit:

$$q = -1.4399n^{-2} + 0.7099n^{-1} + 0.6681 + 0.0636n$$

Equation (4.3.3) is however in a very good agreement with this empirical expression (within 5% accuracy, typically), which is sufficient for the purposes of this study (biological tissue), and in addition provides a simple and elegant physical picture.

Equation (4.3.2) can be now generalized for the index mismatched case. Using equation (4.3.3) it is possible to modify equation (4.3.2) so that it takes into account an index mismatched boundary. An expression may be derived for the dependence of the parameter, k , on the tissue refractive index. Let, k_m , be the generalized k parameter in the index mismatch case. From equation (4.3.3) it follows that

$$R_m = \frac{1}{1 + k_m \frac{\mu_a}{\mu'_s}} \quad (4.3.5)$$

From equations (4.3.2), (4.3.3), and (4.3.5) it can easily be seen that

$$k_m = \frac{k}{1 - q} = \frac{k}{1 - (1 - 1/n^2)} = kn^2 \quad (4.3.6)$$

Finally, equation (4.3.5) can be written as

$$R_m = \frac{1}{1 + kn^2 \frac{\mu_a}{\mu'_s}} \quad (4.3.7)$$

which takes into account effects introduced by the index mismatched boundary. Note that the index mismatch condition tends to decrease the diffuse reflectance, as expected, because of the internal reflection, and to correctly predict diffuse reflectance equal to zero

when $n \rightarrow \infty$ (all light internally reflected). Note also the fact that equations (4.3.2) and (4.3.7) have the same functional form and index mismatch conditions are implemented in a straightforward way.

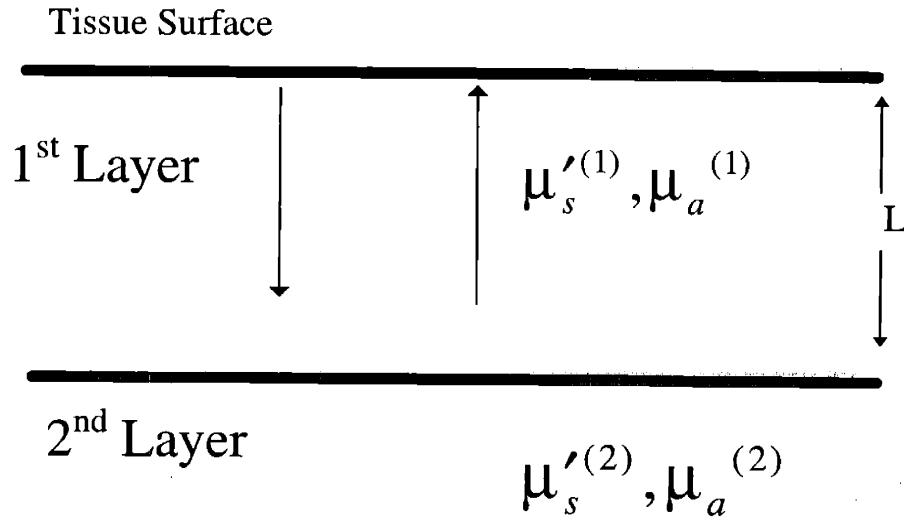


Figure 4.5: Geometry for a two-layer exponential model of diffuse reflectance.

The model developed in this section can be easily generalized to take into account the layered structure of tissue, with each layer characterized by different optical properties. For example, let's consider the case where there are two tissue layers with the top layer thickness being, L , and the second layer extending to infinity (figure 4.5). The top layer is characterized by absorption coefficient, $\mu_a^{(1)}$, and reduced scattering coefficient $\mu'_s{}^{(1)}$, and the second layer by absorption and reduced scattering coefficients, $\mu_a^{(2)}$, and $\mu'_s{}^{(2)}$, respectively. The diffuse reflectance, R_2 , is then given by

$$\begin{aligned}
 R_2 &= 2\mu'_s{}^{(1)} \int_0^L e^{-(\mu_a^{(1)} + \mu'_s{}^{(1)})z} dz + 2\mu'_s{}^{(2)} \int_L^\infty e^{-(\mu_a^{(2)} + \mu'_s{}^{(2)})z} dz \\
 &= \frac{1}{1 + \frac{\mu_a^{(1)}}{\mu'_s{}^{(1)}}} (1 - e^{-(\mu_a^{(1)} + \mu'_s{}^{(1)})L}) + \frac{1}{1 + \frac{\mu_a^{(2)}}{\mu'_s{}^{(2)}}} e^{-(\mu_a^{(2)} + \mu'_s{}^{(2)})L}
 \end{aligned} \tag{4.3.8}$$

Equation (4.3.8), differs significantly from the simpler equation (4.3.7) which corresponds to the semi-infinite case because the parameter L breaks the scale invariance by which equation (4.3.7) is characterized. This interesting observation will be further discussed in terms of the initial data analysis presented in section 6.1.

Equation (4.3.8) is derived here for the refractive index match case, but can be easily generalized to the index mismatch case in way similar to that of the semi-infinite model (equation (4.3.7)). In addition, the correction factor k has been omitted for simplicity, but the same general arguments apply, just as in the case of the semi-infinite model.

4.4 Photon migration model

This method employs probabilistic concepts to describe the scattering of light, and to set up a framework that enables the calculation of the diffuse reflectance from semi-infinite media. Following such an approach, photons are assumed to move in “bunches” or “packets”, with a characteristic initial weight (usually equal to unity), which is subsequently reduced by absorption events. Furthermore, a set of functions, f_n , are defined which describe the probability of a photon packet to escape as diffuse reflectance after a number of n scattering events in a turbid medium with zero absorption. The total diffuse reflectance in the presence of scattering and absorption is then given by equation (4.4.1) [Wu *et al* 1993a]

$$R_t = \sum_{n=1}^{\infty} \left(\frac{\mu_s}{\mu_s + \mu_a} \right)^n f_n \quad (4.4.1)$$

with the normalization condition $\sum_{n=1}^{\infty} f_n = 1$ i.e. all the light escapes as diffuse reflectance in the absence of absorption. Note that f_n depends only on the scattering properties of the medium and is independent of absorption. By making the assumption that f_n has an exponential dependence on n , such that $f_n = ke^{-kn}$ where k is a constant, and by plugging

this in equation (4.4.1), the following expression is derived for the total diffuse reflectance

$$R_t = \frac{1}{1 + k \ln(1 + \mu_a / \mu'_s)} \quad (4.4.2)$$

When $\mu'_s \gg \mu_a$, as it is usually the case for tissue, the logarithm in equation (4.4.2) can be expanded to yield

$$R = \frac{1}{1 + k \ln(1 + \mu_a / \mu'_s)} \cong \frac{1}{1 + k \frac{\mu_a}{\mu'_s}} \quad (4.4.3)$$

This expression is identical to equation (4.3.2) which was derived in a much different way. However, just as in the case of equation (4.3.2), the constant k is not explicitly calculated here either; it is still a free parameter which must be externally calibrated by some other means.

4.5 Path integral formulation

Just like the photon migration technique, the path-integral formulation also treats light scattering as a probabilistic process, but employs a different formalism. The concepts of photon weight, and no-absorption photon path are used again, but the no-absorption path probability f_n , is here explicitly calculated using the Feynman path integral technique. According to this formalism [Perelman *et al* 1994], the concept of the *classical path* is introduced, which is defined as the most probable path that a photon is likely to follow when entering a turbid medium at a point, x_i , and exiting at a point x_f (figure 4.6). The probability for this path may be written as a path integral as follows

$$P(x_i, x_f) = (const) \int e^{-\frac{1}{2\mu_s \sigma^2} \int_0^T (\dot{x}^2 + \dot{z}^2) dt} Dx(t) Dz(t) \quad (4.5.1)$$

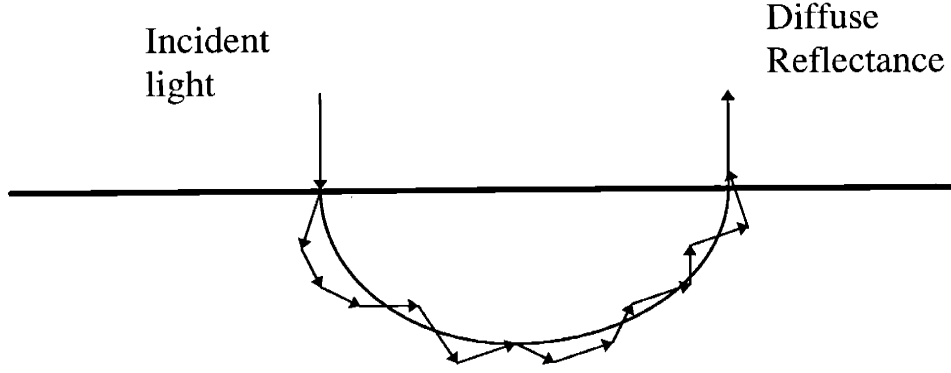


Figure 4.6: Geometry of the path integral picture of diffuse reflectance. Actual path is shown together with the theoretical classical path (smooth line) which is the most probable path for a photon entering and exiting the turbid medium at the points shown.

where the phase function of the scattering process is assumed to be Gaussian,

$$p(\theta) = \frac{1}{2\pi\sigma^2} e^{-\frac{\theta^2}{2\sigma^2}}, \quad (4.5.2)$$

and T is the total travel time of the photon (the assumption for the speed of light $c=1$ has been made here). By evaluating the path integral (4.5.1) using standard techniques [Perelman *et al* 1994, Feynman and Hibbs 1965], the escape probabilities, f_n , may be explicitly calculated:

$$f_n = \left(\frac{3}{2\pi(1-g)} \right)^{1/2} n^{-3/2} e^{-\frac{11}{6n(1-g)}} \quad (4.5.3)$$

with, g , being the anisotropy of scattering. Using equations (4.5.3) and (4.4.1) the total diffuse reflectance can be found:

$$R = e^{-2 \left(\beta \frac{\ln(1+\mu_a/\mu_t)}{1-g} \right)^{1/2}} \quad (4.5.4)$$

Note that this expression is different than the expressions obtained by the methods presented in sections 4.3 and 4.4. The scattering anisotropy, g , and the scattering coefficient, μ_s , appear explicitly in this expression, instead of being combined in μ'_s . This solution is nevertheless in good agreement with the other solutions, as will become evident in section 4.8.

4.6 Monte Carlo method

The Monte Carlo (MC) technique is one of the most powerful methods for solving the radiative transport equation. However, this method provides numerical solutions only, and often requires long computational times. These basic attributes of the method preclude its use in situations where computational speed is an important issue, and the result is required in real time, as in the case of tissue spectroscopy. Despite these drawbacks, the MC method can serve as a standard which may be used for evaluating the validity and accuracy of approximate techniques such as the methods mentioned previously. For example, we have already seen in section 4.3 that in the case of the simple exponential 1-dimensional model, comparison with the results obtained using the MC method enables the evaluation of the correction factor k , which is used to rescale μ'_s in equation (4.3.2).

The use of the MC method to study light transport in tissue is spread widely [Wilson and Adam 1983, Wu *et al* 1993a, Wang *et al* 1995]. The heart of the method consists of a computer simulation of the light propagation process. Photons are launched and traced as they propagate in the turbid medium subject to scattering, absorption, reflectance, and transmission events. The MC method is capable of accurately implementing the correct boundary conditions of the problem by directly simulating its realistic geometry. This enables the calculation of effects due to complicated geometrical configurations, multiple layers, refractive index mismatched boundaries etc. The price paid for this return is of course speed; some complicated configurations require thousands of years to calculate with the present day computers. Fortunately, the problem of diffuse reflectance from biological tissues is simple enough, so as to allow the MC method to

produce acceptable solutions with typical computational times which range from a few minutes to a few hours, with today's computers (1997).

Input parameters are the scattering and absorption coefficients, μ_s and μ_a , the scattering phase function, $p(\theta)$, the tissue refractive index, n , and the details of the geometric configuration of the problem (location of boundaries, layers etc.). Instead of tracing the paths of single photons, packets of photons are considered which propagate together as a group. This scheme has been proven to reduce the variance in the final result, as compared to tracing single photons [Wang *et al* 1995]. Each photon packet is assigned a weight equal to one, and the photons are subsequently propagated according to the following procedure:

(i) A path length, l , is chosen obeying the following probability distribution:

$$p(l) = \mu_t e^{-\mu_t l} \quad (4.6.1)$$

with

$$\mu_t = \mu_a + \mu_s. \quad (4.6.2)$$

(ii) The photon packet is propagated a path length, l , into the medium and the photon weight, w , and the photon absorption weight w_a , are simultaneously updated as follows:

$$w \rightarrow \frac{\mu_s}{\mu_t} w. \quad (4.6.3)$$

$$w_a \rightarrow w_a + \frac{\mu_a}{\mu_t} w. \quad (4.6.4)$$

(iii) The photon packet is scattered by an random angle θ with respect to the previous direction. The scattering angle obeys the probability distribution defined by the scattering phase function, $p(\theta)$. The Henyey-Greenstein phase function (equation (2.1.1)) is usually employed to describe the angular characteristics of scattering.

(iv) If the photon packet reaches a boundary and the medium encountered is air, then the current photon weight is recorded as diffuse reflectance and a new photon packet is

initialized and launched. If the boundary is characterized by a refractive index mismatch condition, the reflection and transmission coefficients are then calculated according to the Fresnel equations.

(v) The process is repeated until the photon is either recorded as diffuse reflectance, or its weight becomes smaller than a preset minimum value, in which case it is terminated in a stochastic way such that premature photon termination does not violate the total photon number conservation [Wang *et al* 1995], and after a new photon packet is launched, the whole process is repeated for the new packet.

4.7 Diffusion theory - method of images

The diffusion approximation to the radiative transfer equation (presented in section 4.2) is a well studied method for calculating the diffuse reflectance from a semi-infinite turbid medium. It is possible to solve the 3-dimensional diffusion equation in the case of an infinitely thin incident light beam, using the Green's function method [Groenhuis *et al* 1983, Schmitt 1991]. However, this method is mathematically complicated and requires rather extensive numerical calculations. Since one of the goals of this study was to evaluate the ability to collect and analyze data *in vivo*, in real time, the simpler and more elegant method of images, was chosen to solve the diffusion equation. An additional advantage of this method, as it will become evident from the discussion below, is that through its simplicity it provides further insight into the physics of the problem, as compared to more mathematically complicated methods.

We begin by assuming that the turbid medium is actually infinite in extent. In that case, the solution of the diffusion equation (4.2.6) due to a point source is given by [Ishimaru 1978]

$$\phi(r) = \frac{1}{4\pi D} \frac{e^{-\mu r}}{r} \quad (4.7.1)$$

where $\phi(r)$ is the energy density, and r is the distance from the source. The boundary condition in this case requires that $\phi(r)$ goes to zero at infinity, which (4.7.1) satisfies. When the turbid medium is semi-infinite (according to the assumption made for tissue), a different boundary condition must be satisfied on the interface (tissue surface). The correct boundary condition states that there is no diffusive light entering the medium i.e. light is allowed to escape, but once it escapes it can not reenter the tissue. This is mathematically expressed by the relation $I(\vec{r}, \hat{s}) = 0$, with \hat{s} pointing inward (in any direction below the surface of the turbid medium). This clearly violates the diffusion approximation (4.2.3) which assumes that light has a non-zero angular dependence on the boundary in all directions. However, an approximate boundary condition may be obtained by requiring that the *average* incoming diffuse flux is equal to zero such that the following relation is satisfied

$$\int_{2\pi, \hat{n} \cdot \hat{s} > 0} I(\vec{r}, \hat{s})(\hat{n} \cdot \hat{s}) d\omega = 0 \quad (4.7.2)$$

The unit vector, \hat{n} , in equation (4.7.2) points inward in the turbid medium, and the integral is taken over solid angle 2π corresponding to the hemisphere located above the surface. Equation (4.7.2) refers to the index matched case. When the turbid medium is characterized by a refractive index larger than unity (as is the case for tissue), the part of the internally reflected light, q , can be thought of as an incoming flux entering the medium from outside (see also section 4.3). In this case, the boundary condition (4.7.2) is written

$$\int_{2\pi, \hat{n} \cdot \hat{s} > 0} I(\vec{r}, \hat{s})(\hat{n} \cdot \hat{s}) d\omega = q \int_{2\pi, \hat{n} \cdot \hat{s} < 0} I(\vec{r}, \hat{s})(\hat{n} \cdot \hat{s}) d\omega \quad (4.7.3)$$

Using now equation (4.2.3), equation (4.7.3) leads to the following boundary condition

$$\phi(r, z) - \frac{2A}{3\mu'_s} \frac{\partial \phi(r, z)}{\partial z} = 0 \quad \text{at } z=0 \quad (4.7.4)$$

where, z , is the depth into the semi-infinite turbid medium measured from the surface, and, r , is the distance from the point of incidence of the light measured on the surface of the medium. The parameter $A = \frac{1+q}{1-q} = 2n^2 - 1$ takes into account the refractive index mismatch condition at the medium/air boundary by means of the total internal reflectance, q , which is a function of the refractive index of the medium and is given by equation (4.3.4).

For a semi-infinite medium, it is possible to implement this boundary condition using a method analogous to the method of images which is used in electrostatics [Farrel *et al* 1992]. A light source with magnitude $S_0 = \frac{\mu'_s}{\mu'_s + \mu_a}$, is positioned at depth $z_0 = \frac{1}{\mu'_s + \mu_a}$, in the tissue. The energy density $\phi(r, z)$ is set to zero at an extrapolated boundary located at a distance $z_b = \frac{2A}{3(\mu'_s + \mu_a)} = \frac{2A}{3} z_0$ above the surface. This is where $\phi(r, z)$ is equal to zero according to the diffusion approximation [Duderstadt and Hamilton 1976]. To implement this condition for $\phi(r, z)$, a light sink with magnitude opposite to that of the light source is positioned symmetrically at a distance $z = z_0 + z_b = \frac{5A}{3} z_0$ above the tissue surface, as shown in figure 4.7. The total energy density due to the source/sink pair is then given by

$$\phi(r, z) = \frac{1}{4\pi D} \left(\frac{e^{-\mu r_1}}{r_1} - \frac{e^{-\mu r_2}}{r_2} \right) \quad (4.7.5)$$

with $r_1 = ((z - z_0)^2 + r^2)^{1/2}$, $r_2 = \left((z - z_0)^2 \left(1 + \frac{2}{3} A\right)^2 + r^2 \right)^{1/2}$.

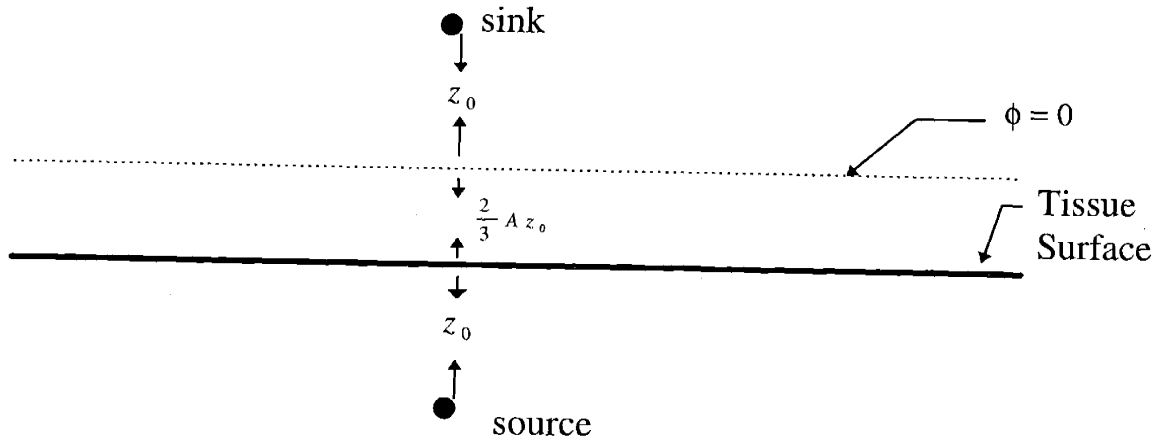


Figure 4.7: Configuration of the light source/sink pair employed to implement the appropriate boundary condition for diffusion of light from a semi-infinite turbid medium.

The diffuse reflectance radial density, $R(r)$, exiting the tissue surface at $z=0$ is given by the flux crossing the boundary, which is calculated by taking the derivative of $\phi(r, z)$ with respect to z evaluated on the surface ($z=0$),

$$\begin{aligned}
 R(r) &= -D \left. \frac{\partial \phi}{\partial z} \right|_{z=0} \\
 &= \frac{z_0}{4\pi} \frac{\mu'_s}{\mu'_s + \mu_a} \left\{ \left(\mu + \frac{1}{r_1} \right) \frac{e^{-\mu r_1}}{r_1^2} + \left(1 + \frac{4}{3} A \right) \left(\mu + \frac{1}{r_2} \right) \frac{e^{-\mu r_2}}{r_2^2} \right\}. \quad (4.7.6)
 \end{aligned}$$

Equation (4.7.6) is an expression for the flux in the direction perpendicular to the surface. It is possible to calculate the flux at any direction other than the perpendicular – see section 5.6 for a more detailed discussion.

Note that equation (4.7.6), unlike the exponential method and the path integral method, provides an expression for the radial distribution of the diffuse reflectance on the surface of the turbid medium. This is very useful for modeling light delivery and collection by fiber optic probes with finite diameter, as in the present study. However, it still does not provide angular resolution of the diffusely reflected light. This issue, which is not a critical one in terms affecting the collected spectra, will be further investigated in chapter 5 (section 5.6).

The total reflectance, R_t , can now be calculated from equation (4.7.6) by integrating over the entire surface area of the tissue

$$R_t = \int_0^{2\pi} d\phi \int_0^{\infty} R(r) r dr = (1 + e^{-\frac{4}{3} A \mu z_0}) \frac{e^{-\mu z_0}}{2} \quad (4.7.7)$$

Equation (4.7.7) is an expression for the total diffuse reflectance analogous to expressions (4.3.7), (4.4.3), and (4.5.4) given by the exponential, the photon migration, and the path integral methods, respectively. It is interesting to note that the physical picture of diffuse reflectance from a semi-infinite medium, may be approached in a number of different ways. Comparison of these different methods should provide further insight into the physics of the problem and facilitate the selection of the appropriate model for modeling diffuse reflectance spectra from biological tissue with the use of a fiber optic probe. The following section discusses the advantages and the disadvantages of the various models presented so far.

4.8 Model comparison

Several analytical approaches have been presented in calculating the diffuse reflectance from a semi-infinite medium, including (a) a simple exponential attenuation model (section 4.3), (b) a photon migration model (section 4.4), (c) a path integral model (section 4.5), and (d) a diffusion theory model (section 4.7). As already mentioned, the purpose of examining these models is the better understanding of the physics of the problem and the proper identification of an appropriate model for application to the colon tissue diffuse reflectance data.

The four models presented provide the total diffuse reflectance, R_t , from a semi-infinite turbid medium. It is generally easier to calculate the total diffuse reflectance, as compared to the diffuse reflectance at a given location or angle. Knowledge of the total diffuse reflectance is not adequate in practical cases, however. When diffuse reflectance is measured with a fiber optic probe which is characterized by a certain diameter and

acceptance solid angle, a model is needed which provides spatial and angular resolution on the tissue surface. Furthermore, for biological tissue applications, the model employed must be characterized by acceptable accuracy within the whole range of optical properties expected to be found in tissue. This range is typically given by $1 \text{ mm}^{-1} < \mu'_s < 5 \text{ mm}^{-1}$, and $0.001 \text{ mm}^{-1} < \mu_a < 1 \text{ mm}^{-1}$, as discussed in chapter 2. Note that the range of the absorption coefficient, μ_a , is much wider than that of the reduced scattering coefficient μ'_s . Since all four models presented yield expressions for the total diffuse reflectance, R_t , it is possible to compare the performance of the models in the range $0.1 < \mu'_s/\mu_a < 1000$ which is realistic for biological tissues.

Figure 4.8 shows R_t for the models presented as a function of the reduced scattering to absorption coefficient ratio μ'_s/μ_a . Note that the characteristic shape of the curves asymptotically approach $R_t=1$ as $\mu'_s/\mu_a \rightarrow \infty$ because in that case all the incident light eventually returns back as diffuse reflectance. For $\mu'_s/\mu_a = 0$ all models correctly give $R_t=0$, because in that case there no diffuse reflectance either due to the fact that $\mu'_s=0$ or because $\mu_a \rightarrow \infty$. The most accurate solution is the Monte-Carlo solution which unlike the other models, makes no approximations in calculating the final result. The differences between the analytical models are expected to be due to the different nature of the various approximations involved in the development of each individual model. Due to the lack of approximations involved, the MC method can be used as the standard to evaluate the performance of each model. Figure 4.9 shows such a comparison with the MC technique. The relative performance of the models is presented, in terms of division by the MC curve. This yields a flat line equal to unity for the MC model, and the deviation of the other models from that line can be seen over the entire range of optical parameters in figure 4.8 by means of the deviation from the ideal value of unity.

Despite the simple and approximate way it was derived, the exponential model performs very well, with a maximum deviation of about 20% at the two ends of the range. The diffusion model agrees very well with the MC solution for small absorption, where it is known that the diffusion approximation provides the highest accuracy [Ishimaru 1978]. The largest deviation for the diffusion model is observed for high absorption ($\mu_a > \mu'_s$),

which is rarely found in biological tissues in the visible range. Finally, the path integral model exhibits a superior agreement with MC (down to 0.1 % accuracy) for high absorption, but it deviates significantly for large absorption.

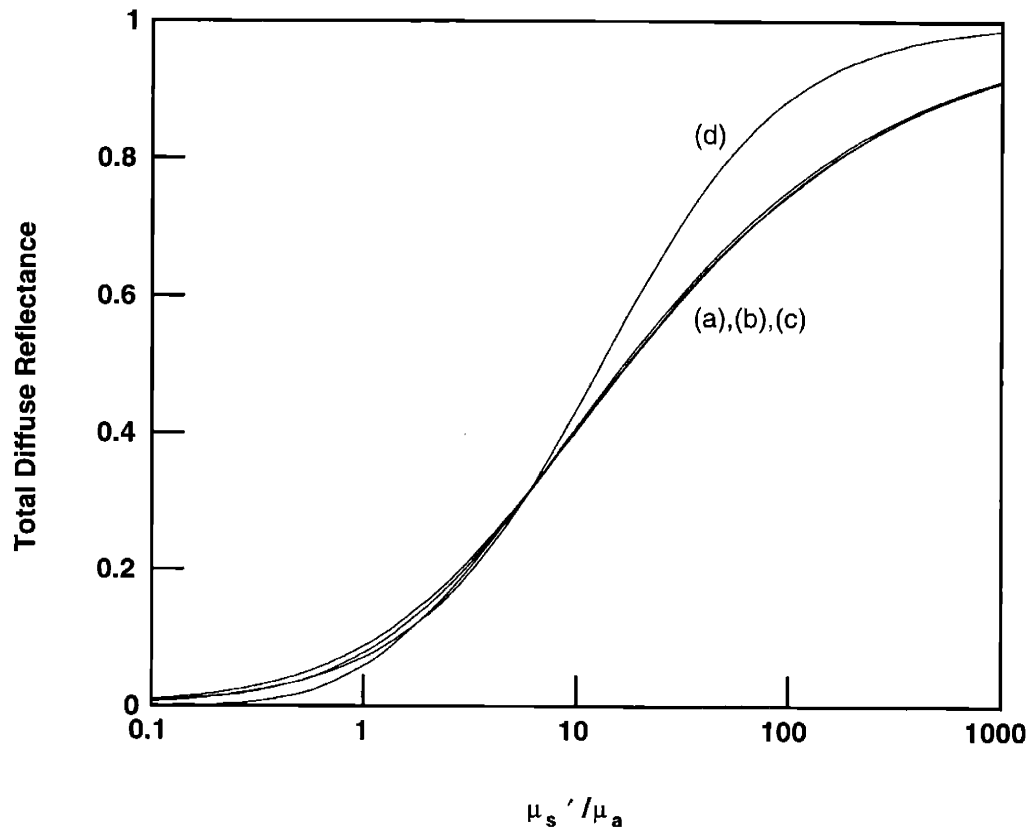


Figure 4.8: Total diffuse reflectance as a function of the μ_s'/μ_a ratio, as calculated by the following models (a) Monte-Carlo model, (b) path integral model, (c) diffusion model, and (d) exponential model. All models appear to be in good agreement except the exponential model which slightly deviates.

Based on these observations, it appears that the exponential model is the simplest and easiest model to use for tissue applications. As will be discussed in chapter 6, it is possible to use a variant of this model to describe the tissue data. However, the formulation of the model in such a case is semi-empirical, in the sense that the model parameters are uncalibrated, are unknown functions of the tissue optical parameters, and hence are not amenable to a simple physical interpretation. The photon migration model is essentially equivalent (in terms of the final expression obtained) to the exponential model, and hence it is not shown in figures 4.8 and 4.9. The path integral model is very

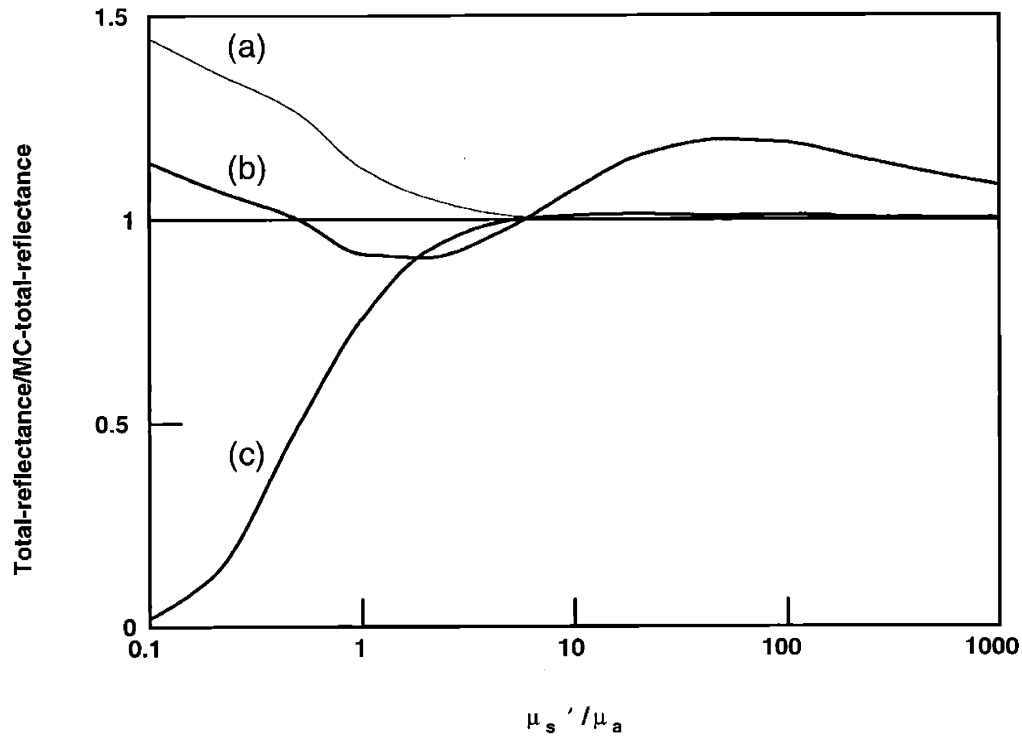


Figure 4.9: Total diffuse reflectance spectra as a function of the μ_s'/μ_a ratio, as calculated by the models presented in figure 4.8. The curves are shown here divided by the Monte-Carlo curve, in order to inspect fine differences between the models. (a) diffusion, (b) exponential, and (c) path integral. All models (except the exponential model) agree very well as long as absorption is smaller than scattering.

accurate in the limit of low absorption, but presents significant deviations from the MC standard for relatively high absorptions. In addition, it does not provide spatial resolution of the diffuse reflectance (the formalism actually permits the calculation of spatially resolved diffuse reflectance, but the process is rather complicated mathematically, requiring numerical evaluation in the final stages). The diffusion model on the other hand provides spatially resolved diffuse reflectance with acceptable accuracy over the entire range of optical parameters. It has been therefore selected as the basis of the model to be used for analysis of the actual tissue data.

4.9 Optical fiber probe model

Using the method of images (section 4.7) to implement the diffusion approximation to the radiative transfer equation, the diffuse reflectance radial density, $R(r)$, collected at a distance, r , from the point of incidence of the light on the surface of a semi infinite turbid medium, is given by equation (4.7.6)

$$R(r) = \frac{z_0}{4\pi} \frac{\mu'_s}{\mu'_s + \mu_a} \left\{ \left(\mu + \frac{1}{r_1} \right) \frac{e^{-\mu r_1}}{r_1^2} + \left(1 + \frac{4}{3} A \right) \left(\mu + \frac{1}{r_2} \right) \frac{e^{-\mu r_2}}{r_2^2} \right\} \quad (4.7.6)$$

$$\text{with } \mu = \left(3\mu_a (\mu_a + \mu'_s) \right)^{1/2}, \quad r_1 = \left(z_0^2 + r^2 \right)^{1/2}, \quad r_2 = \left(z_0^2 \left(1 + \frac{2}{3} A \right)^2 + r^2 \right)^{1/2}, \quad z_0 = \frac{1}{\mu'_s + \mu_a}.$$

The parameter A , which depends on the refractive index of the medium (as explained in section 4.7) has a value of approximately 3.2 for a tissue refractive index of $n \cong 1.4$ [Farrel *et al* 1992].

To find the total light collected by the probe, the expression given by equation (4.7.6) must be integrated over the delivery and collection areas of the probe, which are characterized by radii, r_d , and, r_c , respectively, as illustrated in figure 3.3. Assuming that the incident light intensity is uniform over the entire delivery area, the diffuse reflectance, $R_p(\lambda)$, collected by the probe is then given by

$$R_p(\lambda) = \frac{1}{r_d^2} \int_0^{r_c} r dr \int_0^{2\pi} d\phi \int_0^{r_d} R(\lambda, |\vec{r} - \vec{r}'|) r' dr' \quad (4.9.1)$$

where $|\vec{r} - \vec{r}'| = (r^2 + r'^2 - 2rr' \cos \phi)^{1/2}$. The integrals in equation (4.9.1) can be evaluated numerically. However, due to the cylindrical symmetry of the problem, it is possible to make a simplifying approximation by assuming point delivery of light ($r_d = 0$) and by finding a value for r_c which compensates for this approximation. The diffuse reflectance collected by the probe, $R_p(\lambda)$, is then given by

$$\begin{aligned}
R_p(\lambda) &= 2\pi \int_0^{r_c} R(r) r dr \\
&= \frac{1}{2} \frac{\mu'_s}{\mu'_s + \mu_a} \left\{ e^{-\mu z_0} + e^{-(1+\frac{4}{3}A)\mu z_0} - z_0 \frac{e^{-\mu r'_1}}{r'_1} - (1+\frac{4}{3}A)z_0 \frac{e^{-\mu r'_2}}{r'_2} \right\} \quad (4.9.2)
\end{aligned}$$

where $r'_1 = (z_0^2 + r_c^2)^{1/2}$ and $r'_2 = \left(z_0^2 (1 + \frac{2}{3}A)^2 + r_c^2 \right)^{1/2}$.

To compensate for the point-source approximation, the radius of the collection area, r_c , is empirically calibrated in a way such that equation (4.9.2) closely models the probe diffuse reflectance. Calibration is performed on tissue phantoms with known optical properties, as will be explained in section 5.2. The advantage of this approximation involved in simplifying equation (4.9.1) and deriving equation (4.9.2), lies in the fact that equation (4.9.2) is much easier to invert as compared to equation (4.9.1), which requires numerical integration.

Equation (4.9.2) is now formulated in terms of the absorption coefficient, $\mu_a(\lambda)$, and the reduced scattering coefficient spectrum, $\mu'_s(\lambda)$, and can be used to analyze the diffuse reflectance spectra collected from tissue. At this point, some further key simplifying approximations can be made regarding the formulation of the model in terms of the tissue optical parameters. The first approximation is with regards to absorption. As discussed in section 2.3, hemoglobin is assumed to be the only significant light absorber in colon tissue in the visible range of the spectrum. Based on this assumption, the total tissue absorption, $\mu_a(\lambda)$, is expressed by equation (2.3.1)

$$\mu_a(\lambda) = 2.3 c_{Hb}^* \left(\alpha \epsilon_{HbO_2}(\lambda) + (1 - \alpha) \epsilon_{Hb}(\lambda) \right) \quad (2.3.1)$$

Since the spectral dependence of the quantities $\epsilon_{HbO_2}(\lambda)$ and $\epsilon_{Hb}(\lambda)$ is known from figure 2.2, the spectral dependence of $\mu_a(\lambda)$ is also known, and the only absorption

parameters to be determined are the total hemoglobin concentration, c_{Hb}^* , and the hemoglobin oxygen saturation, α .

When the model (4.9.2) is applied to analyze the data, determination of c_{Hb}^* and α is performed in the following way. For a given tissue spectrum, $R_p(\lambda)$, initial values are assigned to c_{Hb}^* and α (typically $c_{Hb}^*=0.0$ and $\alpha=0.5$). Equation (4.9.2) is then numerically inverted and solved for $\mu'_s(\lambda)$, which exhibits residual characteristic spectral features of hemoglobin absorption. Because the spectral features of hemoglobin cannot be present in $\mu'_s(\lambda)$, the parameters c_{Hb}^* and α are then modified, and the process is repeated in a recursive way, such that $\mu'_s(\lambda)$ presents finally a smooth spectral shape with the hemoglobin spectral features absent.

The analysis procedure described above determines the absorption parameters, c_{Hb}^* and α , and the reduced scattering coefficient spectrum, $\mu'_s(\lambda)$. It is based on the assumption that $\mu'_s(\lambda)$ is a relatively smooth function of the wavelength λ , which is suggested by the *in vitro* results presented in section 2.4, and which data analysis confirms, as it will become evident from the discussion below.

Furthermore, $\mu'_s(\lambda)$ can be written as a product of the scatterer density, ρ_i , and the reduced scattering cross section $\sigma'_i(\lambda)$ of the various tissue scatterers

$$\mu'_s(\lambda) = \sum_i \rho_i \sigma'_i(\lambda) \quad (4.9.3)$$

with the sum taken over all individual scatterers. Unfortunately, detailed knowledge about the tissue scattering properties is not available, and due to this lack of information explicit evaluation of the sum in equation (4.9.3) is not possible. Instead, the *effective* scatterer density, ρ_s , and the *effective* reduced scattering cross section, $\sigma'(\lambda)$, are considered, such that $\mu'_s(\lambda) = \rho_s \sigma'(\lambda)$, i.e. the tissue scattering properties are modeled in an average way, as if tissue contained a single well-defined type of scatterer, with scatterer density, ρ_s , and reduced scattering cross section, $\sigma'(\lambda)$. In general, $\sigma'(\lambda)$ depends on the refractive index, shape, and size of the scatterer, as well as on the refractive index of the

medium surrounding the scatterer. For a spherical scatterer size, $\sigma'(\lambda)$ can be calculated numerically using Mie scattering theory [Wiscombe 1979] (see also section 2.1).

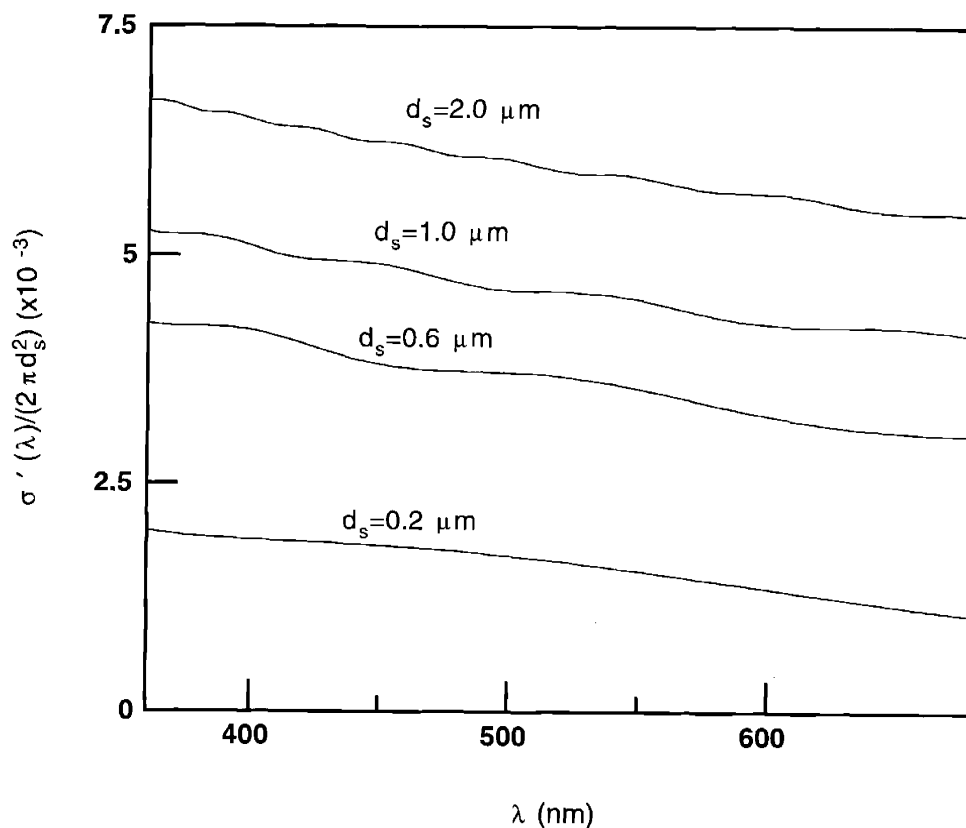


Figure 4.10: Reduced scattering cross section spectra for tissue, $\sigma'(\lambda)$, calculated using Mie theory. Results are shown for four different diameters, $d_s = 0.2, 0.6, 1.0,$ and $2.0 \mu\text{m}$. The slope of the spectra is inversely related to the diameter. A refractive index of 1.4 was assumed for the scattering particles, and a refractive index of 1.36 for the surrounding medium.

Figure 4.10 shows such a calculation of $\sigma'(\lambda)$ for spherical scatterers with various diameters. Note that the slope of $\sigma'(\lambda)$ depends on the scatterer diameter, d_s , in a simple way i.e. the slope is inversely related to scatterer size. In this way, it is possible to assign a scatterer size to every reduced scattering cross section $\sigma'(\lambda)$, and hence to every tissue reduced scattering spectrum $\mu'_s(\lambda)$ in the range $d_s = 0.2 - 2.0 \mu\text{m}$. For example, by inspecting the reduced scattering spectra of normal colon mucosa, previously reported based on *in vitro* measurements [Marchesini *et al* 1994, Zonios *et al* 1996], it can be easily determined that they best match a scatterer size between 0.3 and 0.4 μm . Figure

4.11 shows the slope of $\sigma'(\lambda)$, defined as $\frac{\sigma'(\lambda = 360)}{\sigma'(\lambda = 685)}$, vs. the scatterer size d_s . High spectral slopes correspond to small scatterer size, while lower spectra slopes are indicative of a larger scatterer size. For scatterer size smaller than approximately $1.0 \mu\text{m}$ the slope exhibits stronger dependence on the scattering size. This suggests that determination of sizes smaller than $1.0 \mu\text{m}$ is in general easier and more accurate.

In calculating the results shown in figures 4.10 and 4.11, the refractive indices of the scatterers and the surrounding medium were assumed similar to those likely to be found

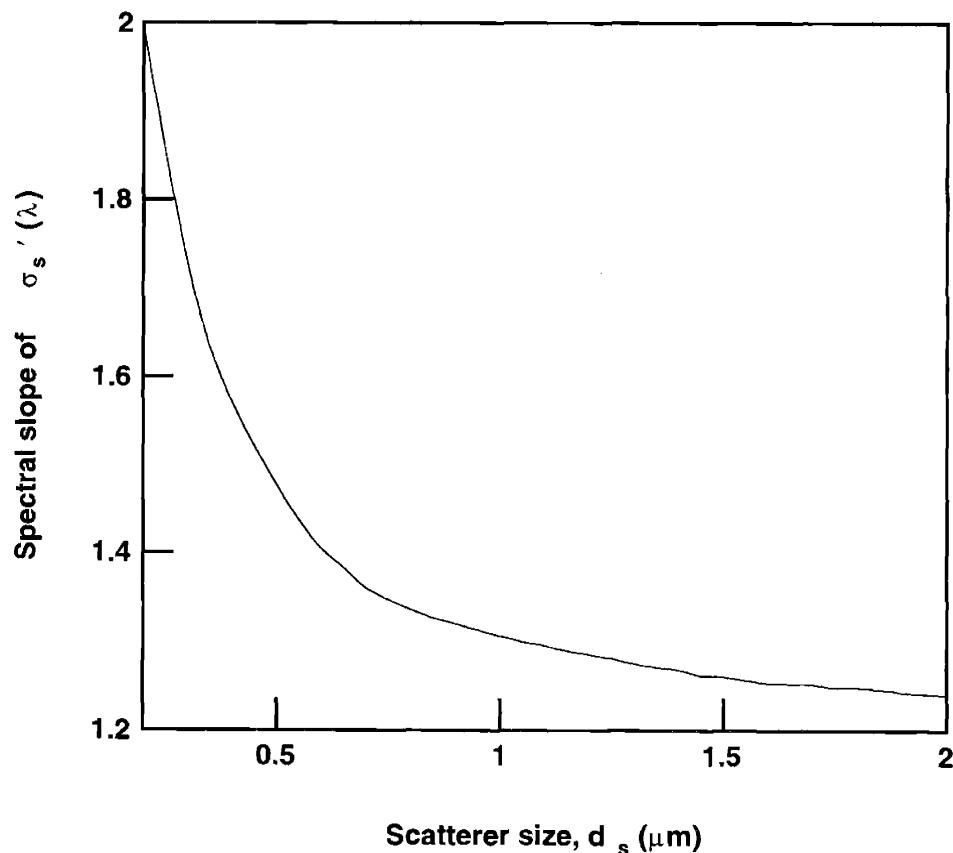


Figure 4.11: Dependence of the slope of the reduced scattering spectrum, $\mu'_s(\lambda)$, on the diameter of the effective scatterer size, d_s , according to Mie theory. Scatterer diameters smaller than $1.0 \mu\text{m}$ have a greater effect on the reduced scattering spectral slope.

in tissue. Reasonable assumptions are a refractive index of approximately 1.36 for the surrounding medium, and approximately 1.4 for the scatterers. These values can be justified by keeping in mind that the lower bound for the tissue refractive index is set by

the refractive index of water, which is approximately equal to 1.33 in the visible range, and the upper bound is set by the maximum refractive index reported for soft tissue, which is around 1.45 [Duck 1990]. In addition, such a range of values is consistent with the magnitude and cross section of light scattering generally observed for soft biological tissues. Wavelength dependence of the refractive index can be assumed negligible; for example, the refractive index of water changes by less than 1% across the entire visible range, as mentioned in section 2.2 [Hale and Querry 1973].

Based on the above discussion, equation (4.9.2) describing the diffuse reflectance, $R_p(\lambda)$, collected by an optical probe, is finally formulated in terms of four scalar parameters: (a) hemoglobin concentration, c_{Hb}^* , (b) hemoglobin oxygen saturation, α , (c) effective scatterer density, ρ_s , and (d) effective scatterer size, d_s . Data analysis produced a set of the four parameters, $(c_{Hb}^*, \alpha, \rho_s, d_s)$, for every tissue diffuse reflectance spectrum. The absorption parameters were first obtained, and then the scattering parameters were obtained by fitting the calculated tissue reduced scattering coefficient spectra to Mie theory, as explained above. The analysis of the data will be presented in chapter 6.

CHAPTER 5

INVESTIGATIONS ON TISSUE PHANTOMS

In this chapter, investigations of the performance of the diffuse reflectance model which was developed in section 4.9 will be presented. Tissue phantom materials will be employed for this purpose. The term “tissue phantom” refers to materials which simulate the specific optical properties and the geometry of tissue. The advantage here is that in contrast to the case of real tissue, the optical properties of the phantom are known. Application of the diffuse reflectance model to the spectra collected on the phantom should yield the correct optical properties. Comparison of the output of the model with the known optical properties of the phantom, provides a way of evaluating the accuracy, validity, and performance of the model in terms of describing the diffuse reflectance spectra from tissue.

In addition to investigating the accuracy of the model in terms of predicting the optical parameters of the phantoms, the basic approximations employed in deriving the model were tested. This was done by using hemoglobin and spherical beads to generate the absorption and scattering properties of the phantoms, respectively. Another important use of the tissue phantoms was the calibration of the probe radius parameter, r_c , (see discussion in section 4.9). Moreover, a few additional issues related to the diffuse reflectance problem were investigated, such as the significance of the angular and spatial resolution of the diffuse reflectance in terms of optical probe design. Finally, issues that have to do with light penetration depth, and hence the sampling depth in tissue, were

studied. After testing on tissue phantoms is presented in this chapter, application of the model to the real tissue data will follow in chapter 6.

5.1 Phantom construction

To simulate light scattering, suspensions of spherical polystyrene particles (beads) in de-ionized water (Polysciences, Inc) were used. The beads were modeled as dielectric spheres with their scattering properties given by Mie theory. Tissue absorption was simulated by introducing hemoglobin into the phantom, prepared from lyophilized (freeze-dried) human hemoglobin (Sigma, H0267). The hemoglobin solutions were in equilibrium with air in atmospheric pressure, so that hemoglobin was essentially in the oxygenated form (oxyhemoglobin). Generation of deoxyhemoglobin requires special experimental techniques to control the partial pressure of oxygen (see section 2.3). These will be discussed in section 5.8, where the hemoglobin oxygen saturation effects in tissue absorption will be discussed in terms of phantom simulations.

The scattering properties of the polystyrene beads were calculated numerically using a Mie theory computer code [Wiscombe 1979]. Figure 5.1 shows the reduced scattering coefficient spectrum, $\mu'_s(\lambda)$, of beads with various sizes which were used in the construction of the various phantoms. The values shown are for total polystyrene concentration of 0.625% by volume. This yielded $\mu'_s(\lambda)$ in a realistic range for tissue (according to the measurements presented in section 2.4 and other reports in the literature for soft tissues [Cheong *et al* 1990, Duck 1990]). Since polystyrene light absorption is negligible in the visible range, absorption in the phantoms was solely due to oxyhemoglobin.

Note that the spectral dependence of $\mu'_s(\lambda)$ shown in figure 5.1 is qualitatively similar to that presented in figure 4.10 for tissue i.e. the spectra exhibit a relatively smooth shape with slope inversely related to bead size. The main difference here is that for polystyrene beads the slope is higher due to the higher refractive index, n_p , of polystyrene, which exhibits a weak dependence on the wavelength across the visible

range and is given by the expression $n_p = 1.5607 + 10002/\lambda^2$, (λ in nm) [Marx and Mulholland 1983] so that $1.62 > n_p > 1.58$ in the range $400 < \lambda < 700$ nm. The background scattering material (de-ionized water), was assumed to have refractive index equal to 1.335, independent of wavelength, which is a very good approximation, as discussed in section 2.2. The size of the phantoms was approximately 30x30x5 mm, simulating the flat geometry of the normal colon mucosa. Additional phantoms were constructed with cylindrical geometry (10 cm depth and 5 mm diameter) to simulate the geometry of the polyps, but no significant spectral differences were found due to the different geometries. This was as expected, since these dimensions are much larger than the mean free path of light. The measurements on the phantoms were performed in a manner similar to that of the measurements performed on tissue, by utilizing the same data collection system (presented in chapter 3) and by placing the optical probe in contact with the surface of the phantom.

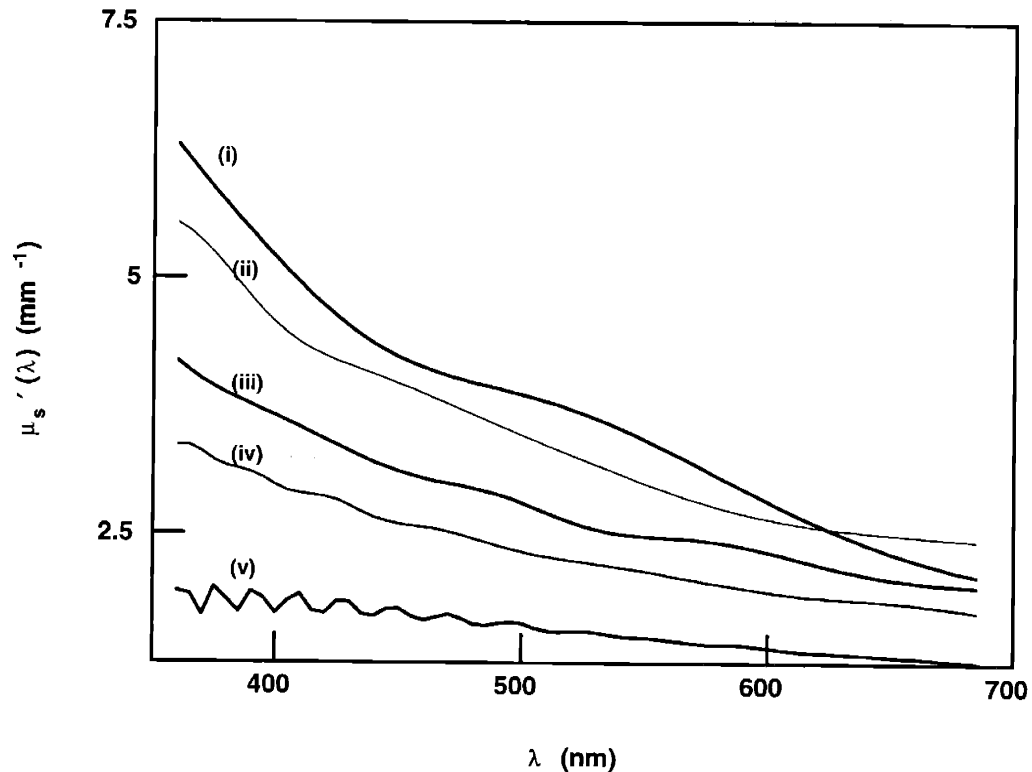


Figure 5.1: Reduced scattering spectra of polystyrene beads corresponding to five different bead diameters: (i) 0.35 μm , (ii) 0.48 μm , (iii) 0.78 μm , (iv) 1.07 μm , and (v) 1.9 μm . Note the changes in the spectral slope and intensity as a function of the diameter.

In the following investigations of diffuse reflectance on tissue phantoms and comparisons with the analytical model developed in section 4.9, the same spectral calibration technique using BaSO₄ (described in section 3.3) has been employed. In this way, the spectra were measured in arbitrary units of BaSO₄ reflectance. For the purpose of comparing the phantom spectra with the model, equation (4.9.2) was scaled appropriately by the introduction of an overall scaling factor which was determined by direct comparison of the model output with the phantom data. The same scaling technique was employed for the analysis of the actual tissue data which will be discussed in the next chapter.

5.2 Absorption range

Based on the *in vitro* measurements of the optical properties of colon tissue which were presented in section 2.4, absorption is expected to vary across a wide range spanning approximately three orders of magnitude, depending on the wavelength of light. To test the performance of the model in terms of the absorption coefficient, a range from $\mu_a = 0.001 \text{ mm}^{-1}$ to $\mu_a = 5 \text{ mm}^{-1}$ was chosen. Scattering was due to polystyrene beads with 1.07 μm diameter, yielding reduced scattering coefficient $\mu'_s(\lambda)$, in the range 1.7-3.2 mm^{-1} (corresponding to the wavelength range 700-400 nm, see figure 5.1(iv)). The oxyhemoglobin extinction spectrum, $\epsilon_{\text{HbO}_2}(\lambda)$ (figure 2.2) was used in the calculation of the phantom absorption coefficient, $\mu_a(\lambda)$, by means of the relation $\mu_a(\lambda) = 2.3 c_{\text{HbO}_2} \epsilon_{\text{HbO}_2}(\lambda)$ (equation 2.3.1, with $\alpha=1.0$). Different absorption coefficient values were obtained by appropriately varying the oxyhemoglobin concentration. Beer's law (exponential attenuation in absorbing material) holds over a wide range of concentrations for hemoglobin solutions [van Assendelft 1970], so that absorption depended linearly on concentration.

Figure 5.2 shows diffuse reflectance spectra measured on phantoms with different oxyhemoglobin concentrations vs. the model predictions of equation (4.9.2). The four phantom spectra (thick lines) correspond to four different hemoglobin concentrations:

(a) 0.0 mg/dL, (b) 50 mg/dL, (c) 125 mg/dL, and (d) 250 mg/dL. These values cover the typical range of absorption coefficient values expected in tissue. The model predictions using the same optical parameters employed in the preparation of the phantoms are indicated by thin lines. It is important to emphasize that the model spectra are not fits to the phantom spectra, but independent predictions using as input the optical parameters employed in the preparation of the phantom. The purpose of figure 5.2 is to illustrate the accuracy with which the model can describe the phantom data, rather than how well the model can fit the data.

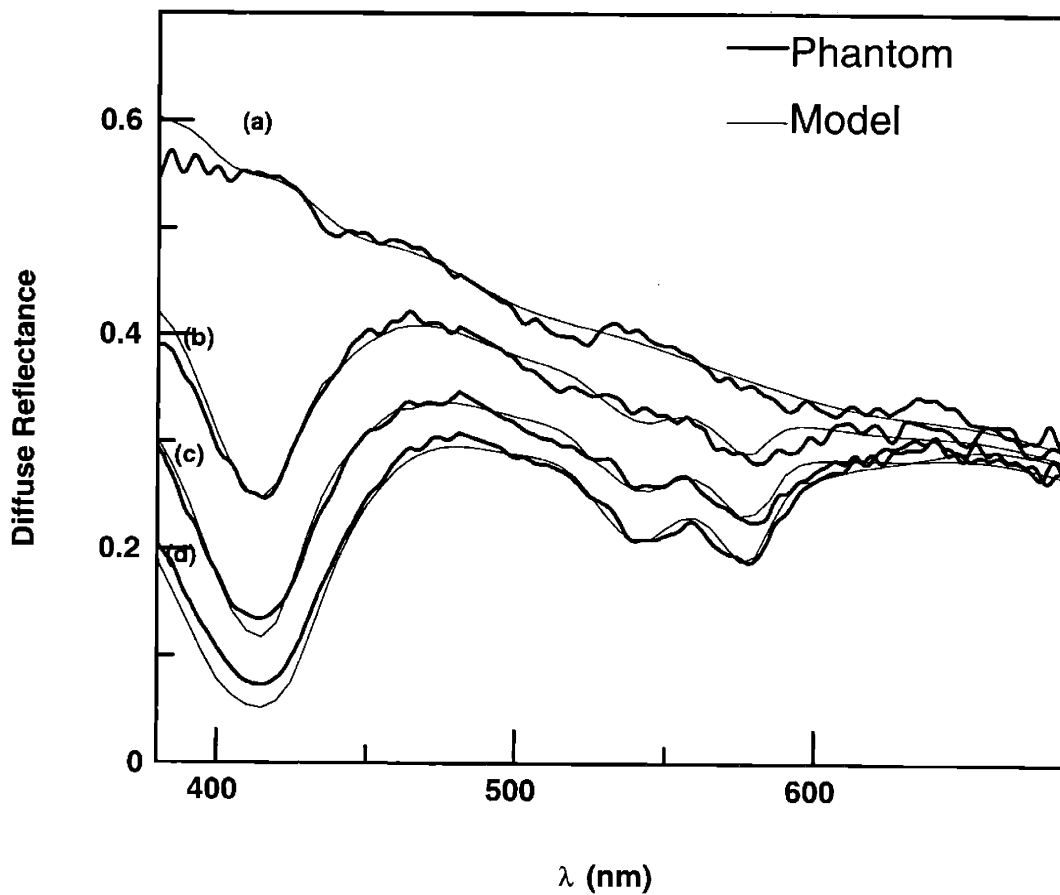


Figure 5.2: Diffuse reflectance spectra measured on tissue phantoms (thick line) corresponding to four different hemoglobin concentrations: (a) 0.0 mg/dL, (b) 50 mg/dL, (c) 125 mg/dL, (d) 250 mg/dL. The model predictions using the same optical parameters employed in the preparation of the phantoms are also shown (thin line). Agreement is very good between the phantom data and the model.

The probe diameter parameter r_c , (equation (4.9.2)) was calibrated based on the results shown in figure 5.2. The optimal value was found to be $r_c=0.45$ mm which is

close to the optical probe specification value of $r_c = 0.55$ mm (see chapter 3). Calibration was performed by comparing the model output to the phantom diffuse reflectance spectrum measured with the phantom oxyhemoglobin concentration set equal to zero (figure 5.2(a)). In this case, the effect of varying r_c represents a change in the slope of the modeled diffuse reflectance spectrum. Increasing r_c tends to make the slope smaller, while decreasing r_c tends to increase the slope. This behavior is expected since in the limit $r_c \rightarrow \infty$ the diffuse reflectance spectrum tends to have a flat shape (slope equal to zero) because in that limit the scale invariance is not broken, and the measured signal is not sensitive to variations in $\mu'_s(\lambda)$ alone. The value $r_c = 0.45$ mm was determined in a way such that the model produced the best fit to the slope of spectrum (a) of figure 5.2 (no hemoglobin). Once determined, r_c was kept fixed for the rest of the tissue phantom experiments, as well as throughout the entire analysis of the tissue data.

According to figure 5.2, the model was found to describe the phantom data with satisfactory accuracy. For hemoglobin concentrations lower than 100 mg/dL, the deviation between the model and the phantom spectra was always smaller than 10% over the entire wavelength range. The largest deviation occurred when absorption was comparable to scattering. This is shown in figure 5.2(d) near the peak of oxyhemoglobin absorption, around 415 nm. The hemoglobin concentration was in this case 250 mg/dL which corresponds to an absorption coefficient of approximately 5 mm^{-1} at 415 nm, while the reduced scattering coefficient was approximately 2.8 mm^{-1} at the same wavelength. In the range of high absorption, it was found that the model parameter $z_0 = 1/(0.6\mu_a + \mu'_s)$ improved the agreement between the model and the phantom data, while in the low absorption range, $z_0 = 1/\mu'_s$ was found to give best results. This parameter was also calibrated on the phantom in a manner similar to parameter r_c , i.e. following determination ($z_0 = 1/(0.6\mu_a + \mu'_s)$) it was kept fixed at that value throughout the data analysis. More detailed discussion regarding the parameter z_0 will be presented in section 5.4.

In summary, it was established that the model performs satisfactory across the range of absorption coefficient values found in colon tissue, as long as μ_a does not significantly exceed μ'_s . Since absorption is not expected to exceed scattering in colon tissue in the visible spectral range, the model is expected to perform adequately in terms of describing the tissue data. In addition, even in the limit of very high hemoglobin absorption, where a deviation is noted between the model and the phantom data around 415 nm, the model still describes quite well the majority of the spectral range. This indicates that it can still be used to analyze the data and calculate the four relevant parameters with acceptable accuracy.

5.3 Scattering range

In this section, the performance of the model in terms of the parameters describing the tissue scattering properties i.e. the effective scatterer size, d_s , and the effective scatterer density, ρ_s , will be investigated. These parameters are related to the reduced scattering coefficient, $\mu'_s(\lambda)$, as explained in section 4.9. As can be seen from figure 5.2(a) which shows the diffuse reflectance spectrum of 1.07 μm diameter beads with no hemoglobin added ($\mu_a(\lambda)=0.0$), the model is capable of successfully describing variations in $\mu'_s(\lambda)$ across the whole wavelength range with satisfactory accuracy. In the case of figure 5.2(a), $\mu'_s(\lambda)$ changes from 1.7 mm^{-1} at 700 nm, to approximately 3.2 mm^{-1} at 400 nm, as already stated in the beginning of section 5.2. This covers a realistic range for $\mu'_s(\lambda)$, which is expected for tissue. Note that in contrast to absorption which presents a variation of approximately three orders of magnitude across the wavelength range, variations in $\mu'_s(\lambda)$ are restricted in the much narrower range, usually between 1.0 and 4.0 mm^{-1} .

To assess the ability of the model to correctly describe the scatterer size, d_s , and scatterer density, ρ_s , phantoms were prepared using 5 different bead diameters: 0.35, 0.48, 0.78, 1.07, and 1.9 μm . The $\mu'_s(\lambda)$ spectra corresponding to polystyrene beads of the different sizes have been already presented in figure 5.1. Diffuse reflectance spectra were

measured from each phantom with no oxyhemoglobin added, and the spectra were compared to the output of the model. Figure 5.3 shows the results of the comparison with the phantom data represented by a thick line, and the model output by a thin line. The model describes the data in a satisfactory manner, in terms of both the spectral slope (parameter d_s) and the overall value of the diffuse reflectance (parameter ρ_s).

Careful inspection of figures 5.1 and 5.3 reveals that the diffuse reflectance spectra

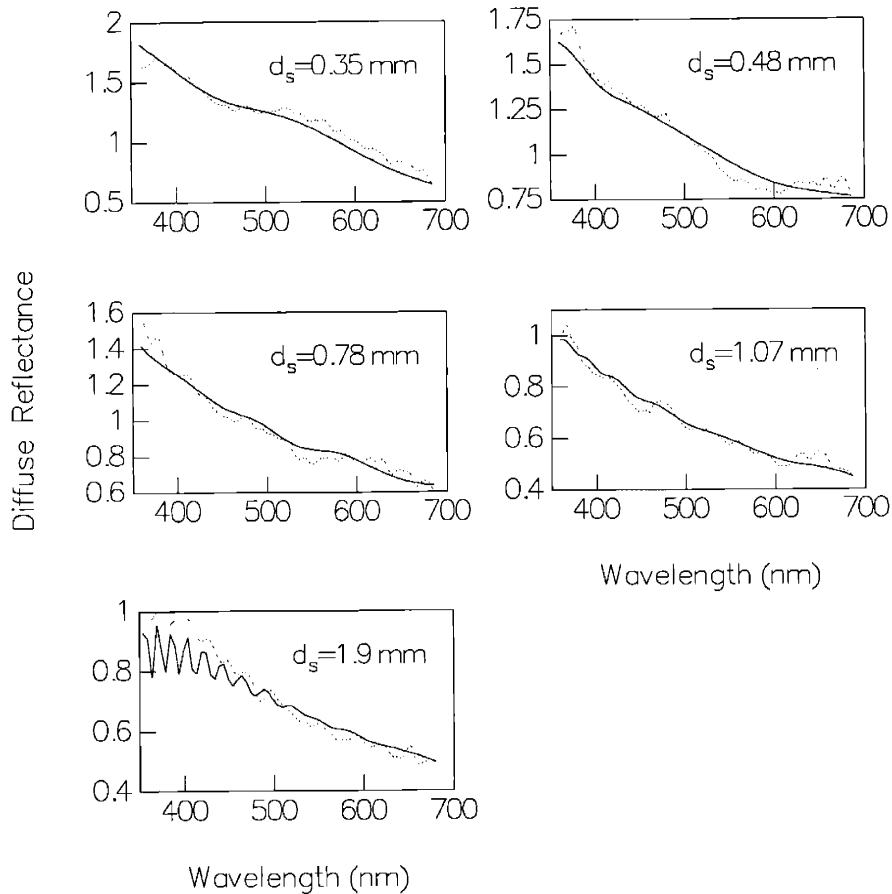


Figure 5.3: Comparison between phantom data (dotted lines) and the model output (solid lines) for phantoms made out of different size polystyrene beads with no hemoglobin added. Results are shown for 0.35 μm , 0.48 μm , 0.78 μm , 1.07 μm , and 1.9 μm bead diameters, d_s . The model predicts in an accurate way both the spectral shape of the diffuse reflectance spectra (related to the size d_s), and the overall intensity (related to the scatterer density ρ_s).

exhibit the characteristic features of $\mu'_s(\lambda)$. This is expected because $\mu'_s(\lambda)$ is the only free parameter in the model in the absence of absorption. In general, the spectra exhibit smooth shapes and change slowly as a function of wavelength, with the exception of the

spectra corresponding to $d_s = 1.9 \mu\text{m}$ where an oscillation is observed for $\lambda < 450 \text{ nm}$. Note that the model even predicts this small oscillation (figure 5.3(e)) (with a deviation in the overall intensity).

Based on these results, we conclude that the model satisfactorily describes variations in $\mu'_s(\lambda)$, and that it accurately describes diffuse reflectance spectra measured from homogeneous suspensions of spherical scatterers with sizes in the range $d_s = 0.35\text{-}1.9 \mu\text{m}$. In addition it accurately predicts the concentration of the bead suspensions, which affects the overall intensity of the spectra.

5.4 Optical probe response

In chapter 4, various models providing the total diffuse reflectance from a semi-infinite turbid medium were investigated, and it was pointed out that the total diffuse reflectance is a function of the μ'_s/μ_a ratio only. This does not hold true for the diffuse reflectance collected by an optical probe because the probe breaks the scale invariance of the problem and introduces explicit separate dependencies on μ'_s and μ_a . Thus, an optical probe with certain geometric characteristics (diameter, acceptance angle, etc.), can be completely characterized by studying these separate dependencies of the diffuse reflectance spectra, on μ'_s and μ_a . One way to do this is by generating the 3-dimensional plot of the probe diffuse reflectance as a function of μ'_s and μ_a , either theoretically or experimentally. However, the complexity of realistic optical probe geometries limits the applicability of theoretical models, and the best practical way to determine the behavior of a probe in terms of the optical properties of the medium under study, is by means of empirical calibration.

The phantom data presented in sections 5.2 and 5.3 provide valuable information for investigating the behavior of the probe. Detailed knowledge regarding the probe delivery and collection characteristics is very useful because different probe geometries correspond to different probe sensitivities in terms of the extent at which the absorption and scattering of the medium under study affect the diffuse reflectance spectra measured.

For example, a given optical probe may enhance absorption affects in the collected diffuse reflectance spectra, while a different probe may enhance scattering effects. Also, the overall intensity of the light collected, as well as the sampling depth of the light may be affected. Since a 3-dimensional plot is difficult to analyze, the dependencies of the probe diffuse reflectance on μ'_s and μ_a will be studied separately.

Using the phantom data shown in figure 5.2, the curves presented in figure 5.4 were generated, which show the diffuse reflectance collected by the probe as a function of the absorption path length ($1/\mu_a$) for a constant value of μ'_s ($\mu'_s(\lambda = 415 \text{ nm})=2.9 \text{ mm}^{-1}$). Experimental data on phantoms represented by triangles, correspond to various absorption coefficient values measured at 415 nm. The continuous lines correspond to the model predictions (equation (4.9.2)). Figure 5.4(b), which best matches the phantom data, was generated with $z_0 = 1/(0.6\mu_a + \mu'_s)$, while figure 5.4(a) was generated with $z_0 = 1/\mu'_s$ and agrees very well with the phantom data only in the small absorption range. Note that when the value $z_0 = 1/(\mu_a + \mu'_s)$ is used, given by [Farrel *et al* 1992], the model results deviate from the phantom data, in the small absorption range, and it is not shown in figure 5.4. In this way, the parameter z_0 was empirically calibrated in a manner similar to that with which the parameter r_c was calibrated in section 5.2. The empirical expression $z_0 = 1/(0.6\mu_a + \mu'_s)$ was adopted for the phantom and tissue data analysis because of its better performance in the high absorption range (usually reflected in the spectral range 400-450 nm).

Note that the curves (a) and (b) shown in figure 5.4 exhibit first a rather steep increase for $\mu_a \geq 0.1 \text{ mm}^{-1}$, and then level off a maximum value. This indicates that starting from the case of zero absorption where the diffuse reflectance signal is maximized, a steady increase in absorption (even by several orders of magnitude) does not significantly affect the probe diffuse reflectance. Only when $\mu_a \geq \mu_{a0}$, with μ_{a0} an absorption coefficient value characteristic of the probe ($\mu_{a0} \cong 0.1 \text{ mm}^{-1}$ in the present case), absorption starts to introduce significant changes in the signal detected. In this way, a characteristic absorption coefficient value, μ_{a0} , can be identified for every probe, below which the diffuse reflectance exhibits a very small dependence on absorption. This

characteristic value strongly depends on the effective separation between light delivery and collection of the probe. The larger the delivery/collection separation, the more sensitive the probe becomes to absorption, as has been also pointed out by other researchers [Kumar and Schmitt 1997, Perelman *et al* 1997]. This information is important due to the fact that an optical probe can thus be designed in terms of the specific absorption range one is interested to probe.

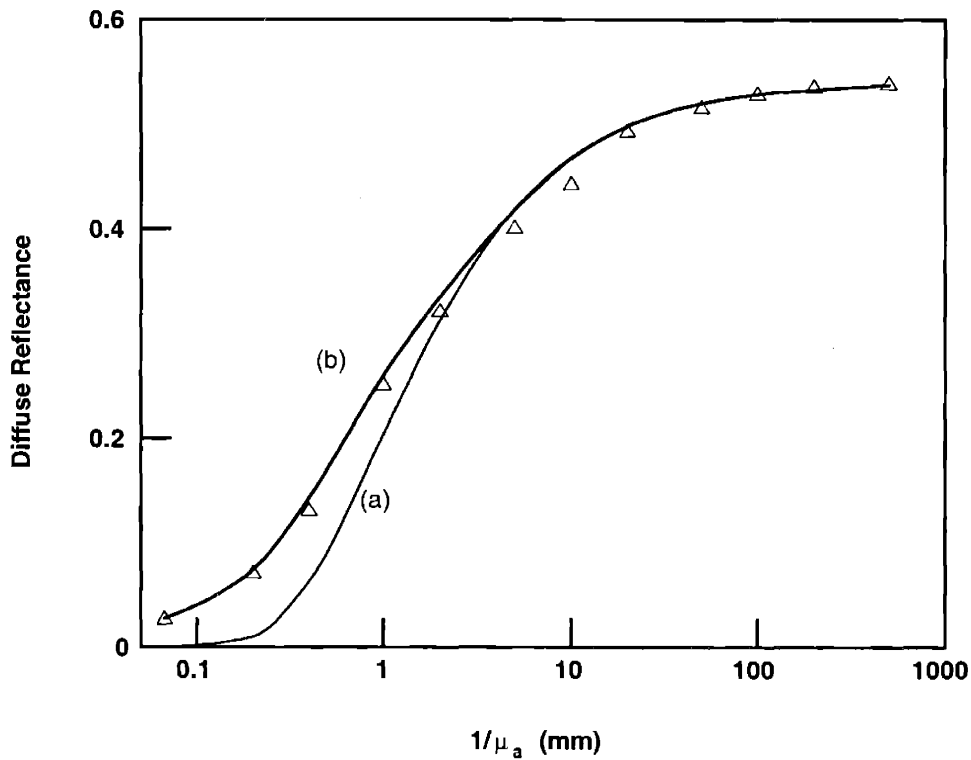


Figure 5.4: Diffuse reflectance collected by the probe as a function of the absorption path length ($1/\mu_a$) for a constant reduced scattering coefficient value ($\mu'_s=2.9 \text{ mm}^{-1}$). Two model output curves are shown for two different values of the parameter z_0 : (a) $z_0=1/\mu'_s$, and (b) $z_0=1/(0.6\mu_a + \mu'_s)$. Note that the second curve agrees better with the phantom data (indicated by triangular points) in the range of high absorption.

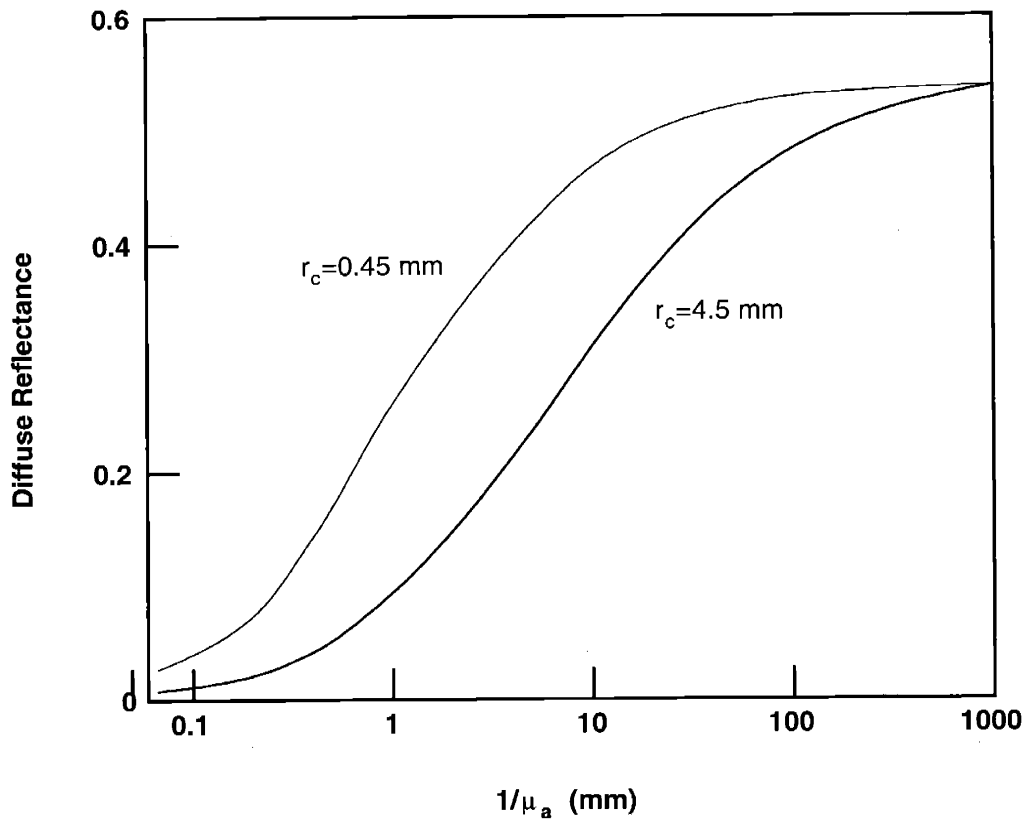


Figure 5.5: Diffuse reflectance collected by the probe as a function of the absorption path length ($1/\mu_a$) for two different values of the parameter r_c (related to probe diameter): $r_c = 0.45$ mm (used in this study), and $r_c = 4.5$ mm. Note that the larger diameter probe is more sensitive to absorption and tends to exhibit a curve closer to that of total diffuse reflectance (figure 4.8). The reduced scattering coefficient was constant for both curves ($\mu'_s = 2.9$ mm⁻¹).

The effect of the probe diameter in terms of the sensitivity to absorption is illustrated in figure 5.5, where the diffuse reflectance is plotted (using the model) for two probe geometries: (a) $r_c = 0.45$ mm (same as figure 5.4), and (b) $r_c = 4.5$ mm. Note that the probe with the larger diameter is more sensitive to absorption, because changes around small absorption values which produce very small difference in the diffuse reflectance collected by probe (a) (small diameter), produce significantly larger changes in the diffuse reflectance collected by probe (b) (large diameter). In other words, the negative of the derivative with respect to μ_a of curve (b) is larger than that of curve (a). The probe sensitivity to absorption, S_a , can then be defined as follows [Kumar and Schmitt 1997]:

$$S_a = -\frac{dR_p}{d\mu_a} \quad (5.4.1)$$

and in similar way, the sensitivity to scattering, S_s , can be also defined as

$$S_s = -\frac{dR_p}{d\mu'_s} \quad (5.4.2)$$

Both of these parameters can be considered for the optimal design of an optical probe.

Figure 5.6 shows diffuse reflectance curves in a manner similar to those shown in

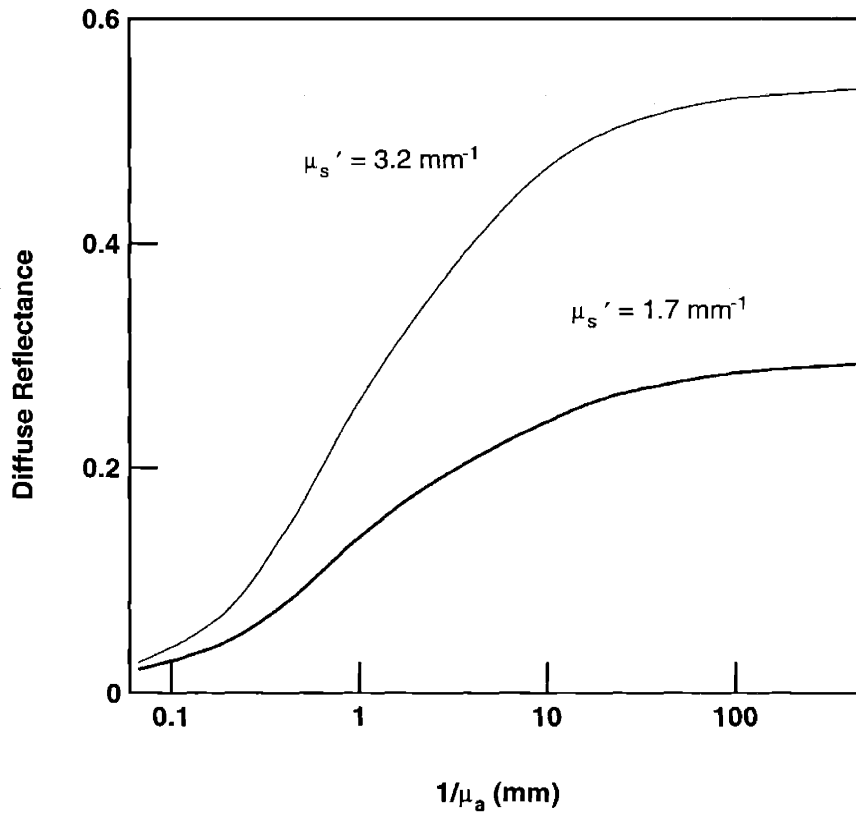


Figure 5.6: Diffuse reflectance collected by the probe as a function of the absorption path length ($1/\mu_a$) for two different values of μ'_s : (a) $\mu'_s=3.2 \text{ mm}^{-1}$, and (b) $\mu'_s=1.7 \text{ mm}^{-1}$. Diffuse reflectance increases as μ'_s increases, but the shape of the curves remains approximately the same since it is defined by the absorption sensitivity S_a .

figure 5.4 but for two different values of the reduced scattering coefficient: (a) $\mu'_s=3.2 \text{ mm}^{-1}$, and (b) $\mu'_s=1.7 \text{ mm}^{-1}$. This illustrates the dependence of R_p on μ'_s , which, in general, increases with increasing μ'_s . This is intuitively obvious because increased

scattering is expected to increase the diffuse reflectance. The shape of the two curves is similar though, and is mainly determined by the absorption sensitivity of the probe, S_a which indicates a rather small dependence of the shape on μ'_s .

Figure 5.7 shows R_p as a function of μ'_s , for three different absorption values, covering the realistic range of absorption values for colon tissue: (a) $\mu_a=0.0 \text{ mm}^{-1}$, (b) $\mu_a=0.4 \text{ mm}^{-1}$, and (c) $\mu_a=3.2 \text{ mm}^{-1}$. The scattering sensitivity, S_s , is defined as the negative slope of these curves. The major observations here are that the diffuse reflectance signal is approximately linearly related to the reduced scattering coefficient, and that the scattering sensitivity is approximately constant in the range $\mu'_s=1.0\text{-}4.0 \text{ mm}^{-1}$ which is the realistic range for the tissues in this study.

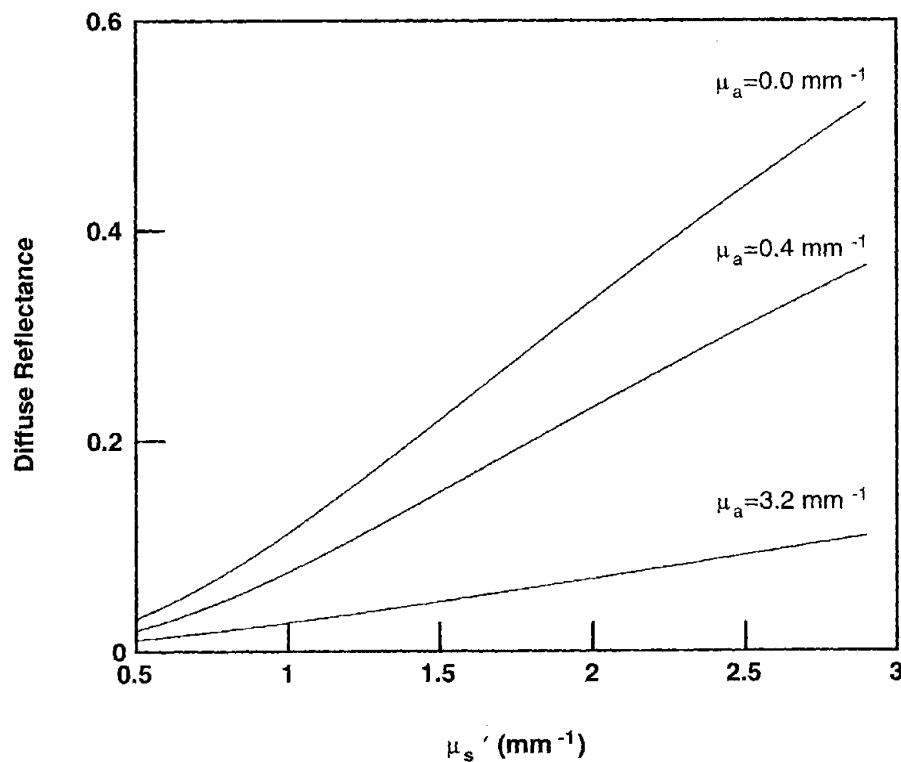


Figure 5.7: Diffuse reflectance collected by the probe as a function of the reduced scattering coefficient μ'_s , for three different absorption values: $\mu_a=0.0, 0.4,$ and 3.2 mm^{-1} . The dependence of the collected diffuse reflectance is approximately linear with μ'_s , and inversely related to the absorption coefficient.

5.5 Delivery/collection geometry

The major approximation made in deriving equation (4.9.2) from equation (4.9.1), was that light is actually delivered at a point instead of an extended circular delivery area with radius r_d which is closer to the realistic case (figure 3.3). To account for this approximation, which was made to avoid numerical integration of equation 4.9.1, the value of the collection radius, r_c , had to be determined empirically on tissue phantoms as explained in detail in the previous sections. It was found that the optimal value was $r_c=0.45$ mm, as compared to the value $r_c=0.55$ mm calculated from figure 3.3. Note that these two values differ only slightly (approximately 20%), a fact which suggests that the approximation involved in deriving (4.9.2) is acceptable.

It is nevertheless interesting to investigate the performance of equation (4.9.1) by explicitly evaluating the integrals numerically, and by comparing the result to the analytical expression given by equation (4.9.2). Figure 5.8(a) shows the results of this comparison as a function of the absorption coefficient μ_a in the range $\mu_a=0-3.0$ mm⁻¹. The top curve corresponds to the quantity

$$k_1 = \frac{R'_p(r_d = 0.35 \text{ mm}, r_c = 0.55 \text{ mm})}{R_p(r_d = 0 \text{ mm}, r_c = 0.45 \text{ mm})} \quad (5.5.1)$$

while the bottom curve corresponds to the quantity

$$k_2 = \frac{R'_p(r_d = 0.30 \text{ mm}, r_c = 0.30 \text{ mm})}{R_p(r_d = 0 \text{ mm}, r_c = 0.45 \text{ mm})} \quad (5.5.2)$$

where R'_p and R_p are the diffuse reflectances given by equations (4.9.1) and (4.9.2) respectively, and μ'_s is kept constant at the typical value $\mu'_s=2.9$ mm⁻¹. Note that equation (4.9.1) with the nominal values $r_d=0.35$ mm and $r_c=0.55$ mm, does not agree with the calibrated expression (4.9.2). A similar behavior is observed in figure 5.8(b) which shows the quantities k_1 and k_2 plotted as a function of μ'_s , in a manner similar to

that of figure 5.8(a), with the absorption coefficient kept now constant ($\mu_a=0$). The fact that k_2 is constant for all values of μ'_s and μ_a indicates that equation (4.9.2) with $r_d=0.0$ mm and $r_c=0.45$ mm agrees well with equation (4.9.1) with $r_d=r_c=0.30$ mm over the entire range of the absorption and reduced scattering coefficient values shown in figures 5.8(a) and 5.8(b).

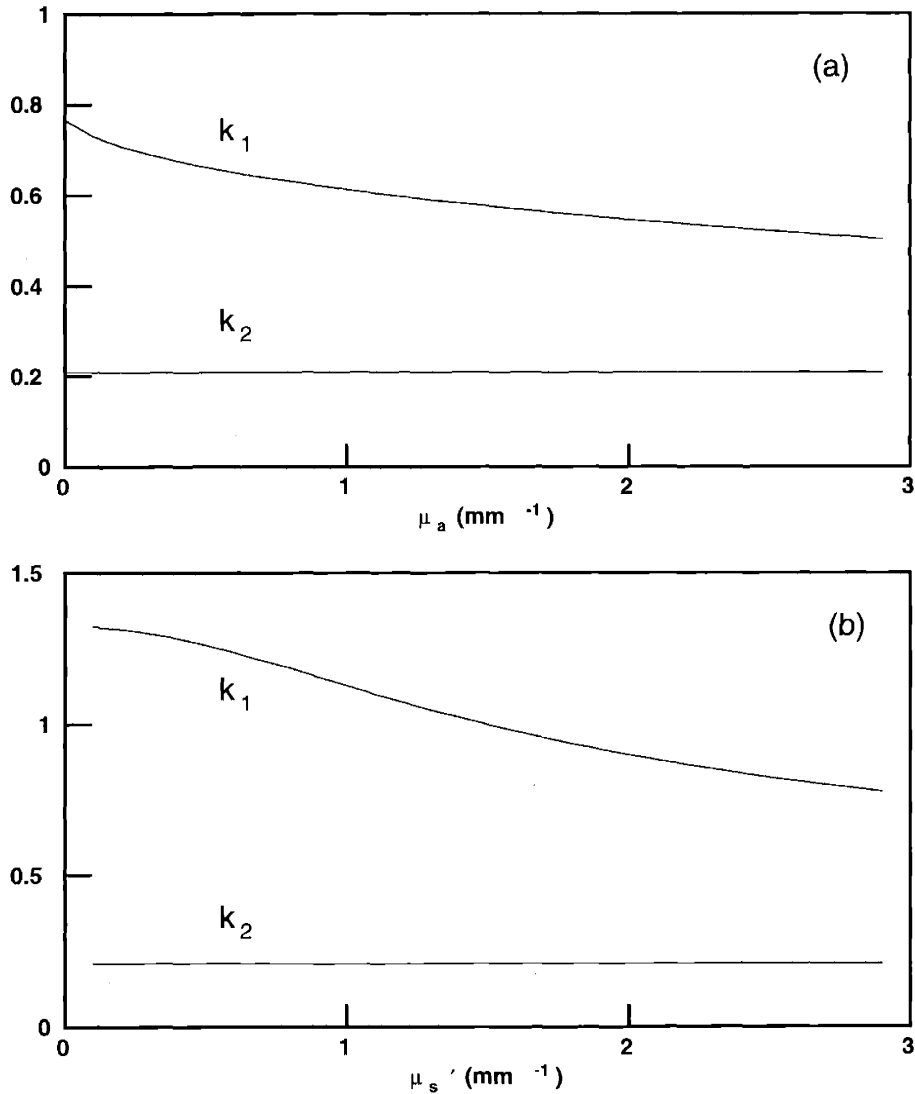


Figure 5.8: Ratio of the diffuse reflectance given by equations (4.9.1) and (4.9.2) (R'_p, R_p respectively): (a) as a function of μ_a for two different sets of the probe parameters r_d and r_c , (b) as a function of μ'_s for the same values of r_d and r_c . The flat line indicates agreement between the two equations for this particular set of r_d and r_c .

The overall picture presented in figure 5.8, indicates that the simple way of calculating the delivery and collection areas of the probe (see figure 3.3) is not accurate enough, and there are probably other probe geometric characteristics which need to be taken into account such as non-uniform illumination, imperfections in the probe shield, the fact that the probe tip is beveled at an angle of 17 degrees etc. However, even in that case, equation (4.9.1) can be made equivalent to equation (4.9.2) by means of empirical calibration of the r_c, r_d parameters (in this case, $r_d = r_c = 0.30$ mm). The main observation appears to be here that both expressions cannot describe the probe without empirical calibration of the parameters, and so they are in that sense equivalent. The additional fact that equation (4.9.2) offers an analytical form makes it superior and thus obviates use of (4.9.1).

5.6 Angular dependence

The diffuse reflectance modeling analysis presented until now, has not dealt explicitly with the details of the angular dependence of the light exiting the tissue surface. Information regarding the angular dependence is important because the light is delivered and collected by means of fiber optics with limited acceptance solid angle (numerical aperture – NA). As mentioned in chapter 3, the NA of the fibers used in this study was 0.22 which corresponds to an acceptance angle of approximately 10 degrees. Light exiting the tissue at an angle θ greater than 10 degrees with respect to the vertical on the tissue surface (figure 5.9), escapes detection. Equation (4.9.2) gives the diffuse reflectance in the direction perpendicular to the surface and provides no information on the angular distribution of the diffusely reflected light. The main issue to be addressed here is whether the fact that only part of the light is detected, introduces any significant spectral changes, thus rendering the model expressed by equation (4.9.2) inappropriate for describing the data collected by means of a fiber optic probe.

In addition to any spectral distortions, the limited acceptance solid angle, S_p , of a fiber optic probe, introduces an overall decrease in the total amount of light detected. If the angular distribution of the diffuse light intensity is isotropic, this decrease can be

easily found to be given by the ratio of the probe solid angle to the total solid angle, i.e. $S_p/4\pi$. This is true when the power per unit solid angle (irradiance) is characterized by a $\cos\theta$ dependence (θ is defined as the angle of the light exiting direction with respect to

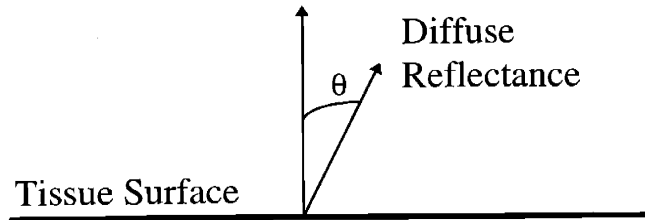


Figure 5.9: Diffusely reflected light exiting at angle θ from the tissue surface.

the vertical on the surface – see figure 5.9). When the irradiance has a $\cos\theta$ dependence, the radiance or specific intensity (power per unit solid angle per unit area) is then constant and independent of the angle θ . This condition is known as *Lambert's Law* [Ditchburn 1976], and one well known situation where it applies, is the description of the angular intensity distribution of diffusive particles escaping from a small hole or aperture [Reif 1965]. It is often incorrectly stated that diffusive light escaping from the surface of a semi-infinite turbid medium follows Lambert's Law. This is not entirely true, since the specific boundary condition of the problem (discussed in detail in section 4.7) forces a different angular dependence than that given by Lambert's Law. However, we shall see in the following that Lambert's Law can be used as an acceptable approximation in the case of diffuse reflectance from tissue.

The correct angular dependence can be found directly from the basic equation expressing the diffusion approximation (equation (4.2.3))

$$I(\vec{r}, \hat{s}) = \frac{1}{4\pi} \phi(\vec{r}) + (3/4\pi) \bar{F}(\vec{r}) \cdot \hat{s} \quad (4.2.3)$$

from which it can be clearly seen [Morse and Feshbach 1953] that the angular dependence in question has the form $f(\theta) = a + b \cos\theta$, where θ is the angle between the

flux, \bar{F} , and the unit vector, \hat{s} , which normal on the surface. The crucial observation here is that the parameters, $a = \frac{4}{7}$ and $b = \frac{6}{7}$, do not depend on the optical properties of the medium, and hence the limited angular collection characteristics of a fiber optic probe are not expected to introduce any significant distortions to the measured spectra. This is in contrast to the radial collection characteristics (such as probe diameter and delivery/collection distance), which introduce strong distortions to the shape of the spectra collected, depending on the underlying optical properties of the medium as will be discussed in section 5.7.

Numerical solution of the transport equation using the Monte-Carlo method (section 4.6) shows that there exists, in fact, a weak dependence of the angular distribution of the diffusive light on the optical parameters of the medium as well as on the refractive index match/mismatch conditions. The introduction of refractive index mismatched conditions at the boundary, together with an increase in the absorption coefficient tend to bring the angular dependence of the light closer to that described by Lambert's Law.

This is illustrated in figure 5.10 which shows the angular dependence of light specific intensity escaping from a semi-infinite turbid medium, obtained through Monte-Carlo simulations. Figure 5.10(a) shows angular distributions corresponding to various absorption values for the refractive index matched case ($n=1.0$). The absorption values corresponding to the first three curves (i), (ii) and (iii) are $\mu_a = 3.0, 0.3,$ and 0.003 mm^{-1} respectively. The reduced scattering coefficient was kept constant at $\mu'_s = 3.0 \text{ mm}^{-1}$. Curve (iv) is the prediction of the diffusion approximation. Note that as absorption is reduced, the exact solution of the problem comes in good agreement with the diffusion approximation. Figure 5.10(b) shows similar distributions for the more realistic (for biological tissue) index mismatched case ($n=1.4$). Three curves are shown for the same values of μ_a shown in figure 5.10(a), and for the same constant value of μ'_s . The angular distribution is now closer to a Lambertian (essentially constant in the range 0-70 degrees, and approximately independent of absorption. There is no comparison here with the diffusion approximation because of the index mismatched boundary.

The general observation from figure 5.10 is that the angular distribution of the diffusive light depends weakly on the optical properties of the medium, as well as on the

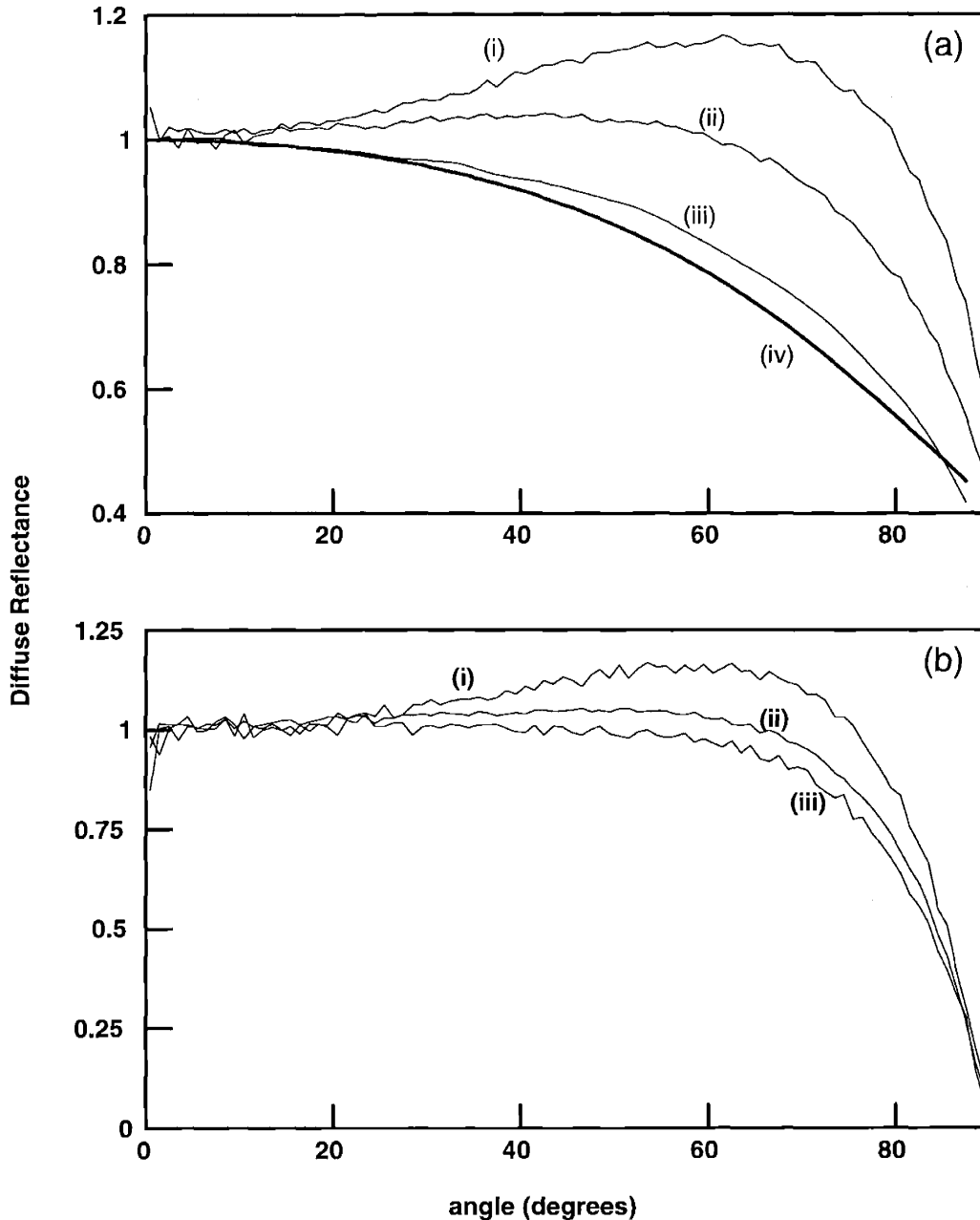


Figure 5.10: Angular distribution of the specific intensity (power per solid angle per unit area) of the total diffuse reflectance from a semi-infinite turbid medium for two different values of the refractive index n : (a) $n=1.0$ (index matched), and (b) $n=1.4$ (index mismatched). The various curves correspond to different values of the absorption coefficient: (i) $\mu_a=3 \text{ mm}^{-1}$, (ii) $\mu_a=0.3 \text{ mm}^{-1}$, and (iii) $\mu_a=0.003 \text{ mm}^{-1}$. The reduced scattering coefficient value was $\mu'_s=2.9 \text{ mm}^{-1}$. Thick line (iv) in figure (a) is the theoretical prediction of the diffusion approximation.

refractive index, and that as absorption increases and a refractive index mismatch boundary condition is introduced, the angular distribution tends to a constant (Lambertian). This indicates that there are no spectral distortions due to the finite acceptance angle of the probe, and that the only correction required is an overall factor, $k = S_p / 4\pi$, by which equation (4.9.2) should be scaled.

One last check is in due because the above discussion did not take into account the finite radial collection characteristics of the probe. To confirm the validity of the above analysis for realistic optical probe geometries, MC simulations were performed for two different sets of optical parameters spanning a range of two orders of magnitude in absorption, (a) $\mu_1 = \mu'_s / \mu_a = 10$, and (b) $\mu_2 = \mu'_s / \mu_a = 1000$, and representing two extreme cases in the variation of the optical properties. The collection and delivery geometry was assumed similar to that of the probe presented in chapter 3. The diffuse reflectance was calculated for two acceptance angle ranges, (a) 0-90 degrees (total reflectance), and 0-10 degrees (optical probe reflectance). Differences between the two angular acceptance ranges can be measured by means of the quantity q_a .

$$q_a = \frac{\frac{R_p^{(90)}(\mu_1)}{R_p^{(90)}(\mu_2)}}{\frac{R_p^{(15)}(\mu_1)}{R_p^{(15)}(\mu_2)}} \quad (5.6.1)$$

If $q_a = 1$ the different angular range has no effect on the spectral shape, while values different than unity signify spectral distortions. $R_p^{(90)}, R_p^{(15)}$ are the diffuse reflectance signals measured in the 0-90 and 0-15 degree ranges, respectively. Figure 5.11 shows q_a , as a function of the delivery/collection separation, r , on the surface. Note that the ratio is close to one as expected for all values of, r , which confirms the original hypothesis that there are no spectral alterations. The maximum deviation (about 15%) occurs for $r > 1$ mm which corresponds to a larger probe than the one used in this study, which had a radius of approximately 0.5 mm. Errors due to the finite angular acceptance of such a

probe are expected to be less than 10%. This is well within the tolerance range of the standard errors involved in measurements on biological tissue.

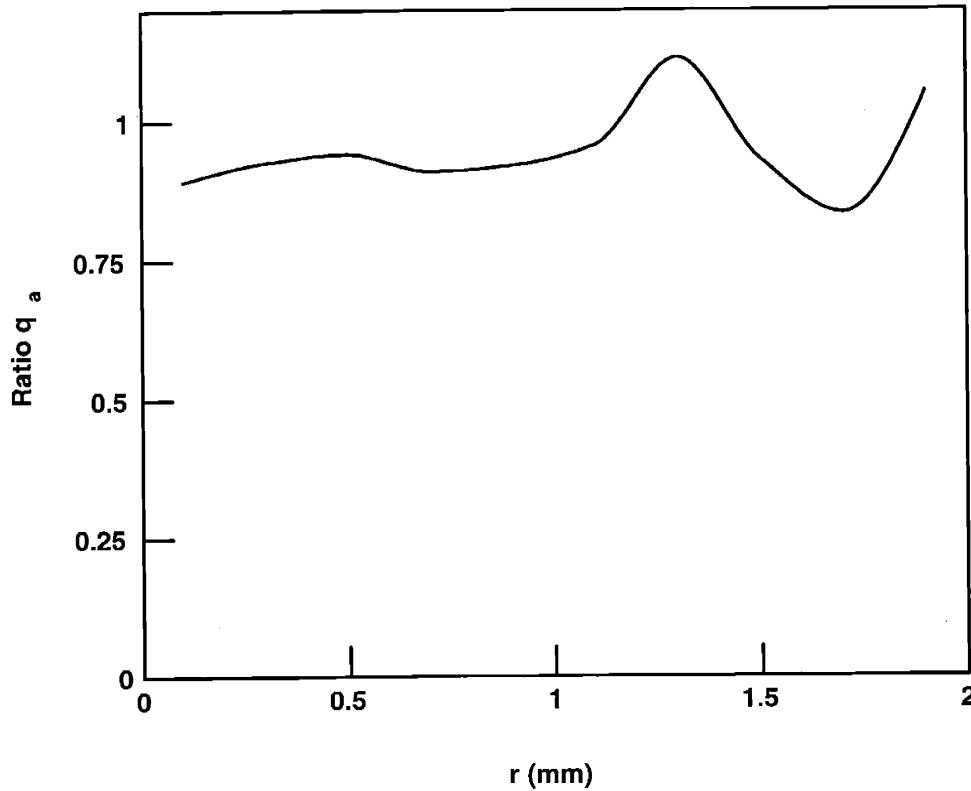


Figure 5.11: Error introduced by an optical probe with 15 degrees acceptance angle as opposed to total collection over all angles (acceptance angle 90 degrees) as a function of the delivery/collection separation r . For $r \cong 0.5$ mm which is close to the realistic value for the optical probe, the error is smaller than 10%. These results are based on Monte-Carlo simulations.

5.7 Radial dependence

The diffuse reflectance depends, in general, very strongly on the distance between delivery and collection points. The intensity of the diffuse reflectance drops dramatically as the delivery/collection separation increases. The radial dependence of the intensity is given by equation (4.9.1), which is the starting point for the derivation of equation (4.9.2) that describes the diffuse reflectance collected by the probe. Based on equation (4.9.2), a variety of expressions may be derived to describe the diffuse reflectance signals collected by a variety of probes with different diameters and/or delivery/collection characteristics.

Such an investigation provides important insight into the fundamental issues of optical probe design for diffuse reflectance collection.

To further investigate these issues, experiments were performed on tissue phantoms to study the radial dependence of the diffuse reflectance i.e. the dependence on the delivery/collection separation. Instead of using the standard optical probe described in chapter 3, a simpler configuration consisting of one delivery and one collection optical fiber was employed, shown in figure 5.12.

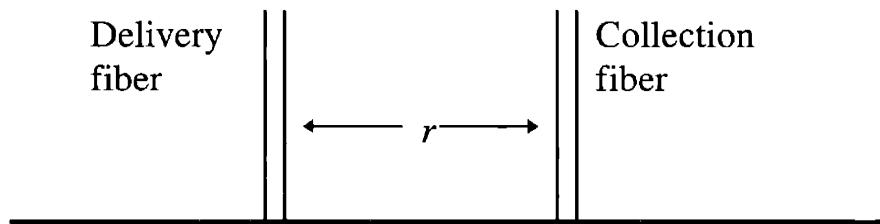


Figure 5.12: Geometry for the phantom experiments with variable delivery/collection separation, r .

The fibers were identical to those used in the construction of the optical probe, characterized by 200 μm core diameter and $\text{NA}=0.22$. The phantom was constructed with 1.07 μm diameter beads with concentration 0.625% by volume polystyrene, and 100 mg/dL oxyhemoglobin. The delivery-collection distance (measured from the center of the delivery fiber to the center of collection fiber), was varied from a minimum of 0.2 mm (fibers side by side, in contact) to a maximum of 10.0 mm in steps of 0.2 mm, and a diffuse reflectance spectrum was collected at each step. Figure 5.13 shows typical diffuse reflectance spectra taken at various fiber separations, namely 0.2, 0.5, 1.0, 1.5, 2.0, 2.5, 3.0, and 3.5 mm. Note that as the fiber separation increases, the overall intensity drops, and the shape of the diffuse reflectance spectra changes dramatically, exhibiting a stronger modulation by the characteristic features of hemoglobin absorption. For large separations (3.0 and 3.5 mm) there is practically no diffuse reflectance measured below 450 nm, where absorption is strongest. These observations are consistent with the analysis presented in section 5.4, where the sensitivity to absorption, S_a , was defined,

and it was also pointed out that probes with large diameter are more sensitive to absorption effects. Thus, to maximize the sensitivity of the probe in terms of investigating fine details of the tissue absorption, a large delivery/collection separation is required. The tradeoff in such a case would be an overall drop in intensity. Both of these effects should be taken into account when designing an optical probe.

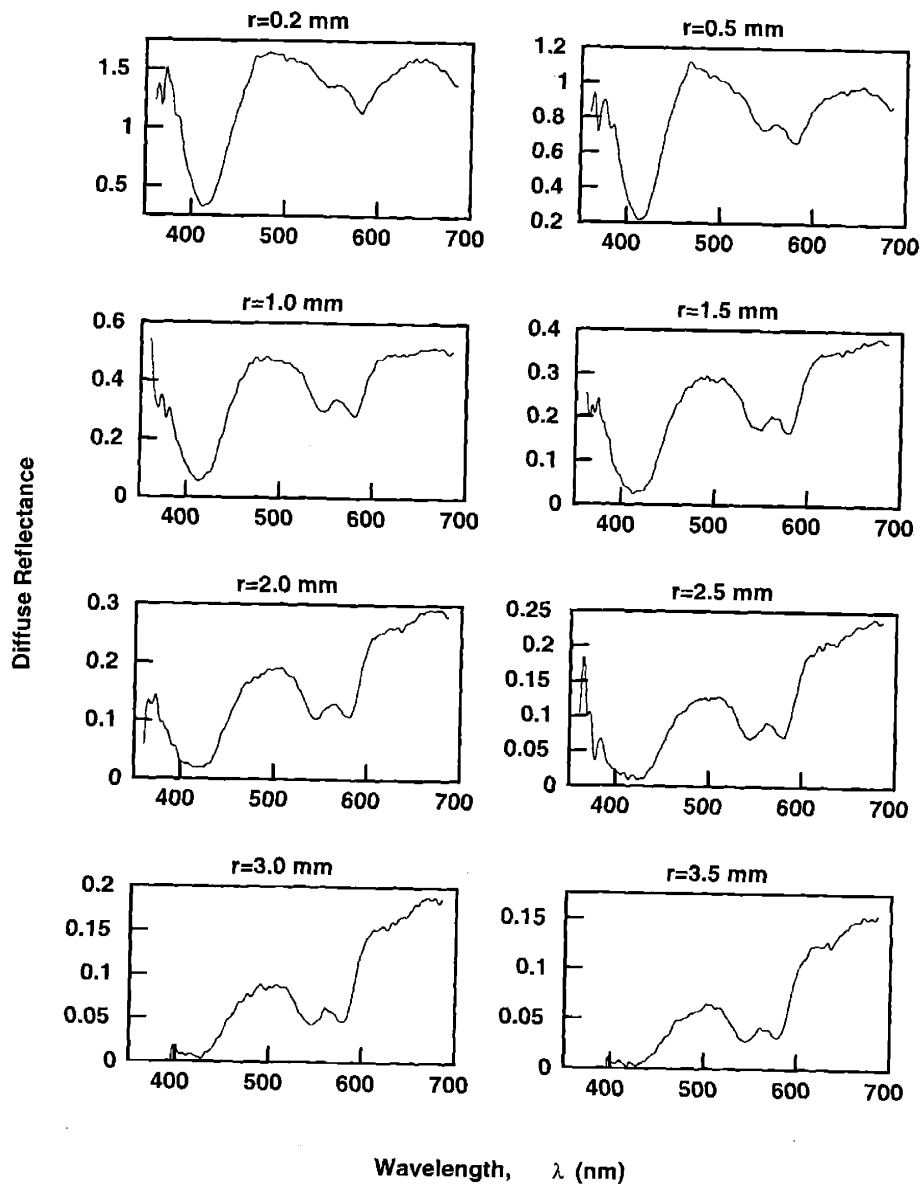


Figure 5.13: Diffuse reflectance collected with various delivery/collection separations ranging from $r=0.2$ mm (upper left) to $r=3.5$ mm (bottom right), by employing the geometry shown in figure 5.1. Note the dramatic changes in the spectral shape and overall intensity as a function of r .

Since measurements of the diffuse reflectance, $R_i(\lambda)$, were performed over an extended range of delivery/collection separations, r_i , the total diffuse reflectance, $R_t(\lambda)$, can be found by evaluating the weighted sum of all the individual measurements as follows,

$$R_t(\lambda) = 2\pi \int_0^{\infty} R(r, \lambda) r dr \cong 2\pi \delta r \sum_i r_i R_i(r, \lambda) \quad (5.7.1)$$

with $\delta r = r_{i+1} - r_i$. Figure 5.14 shows the result of the calculation according to equation (5.7.1) (thick line), along with the theoretical prediction given by the simple exponential model (thin line). Note the very good agreement between theory and experiment illustrated in figure 5.14.

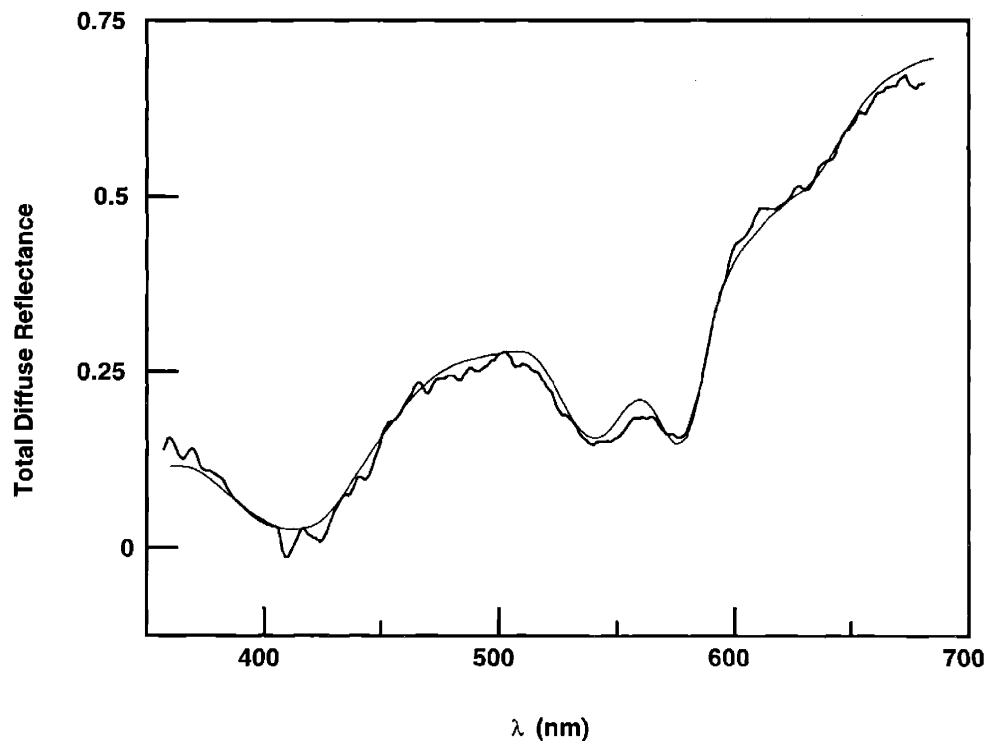


Figure 5.14: Total diffuse reflectance measured on phantom (thick line) vs. exponential model output (thin line). The agreement between experiment and model is excellent.

Even though only part of the diffuse reflectance light was collected due to the limited acceptance angle of the fiber optics used, there were no spectral distortions introduced, so that equation (4.3.7) successfully describes the experimental data. This observation serves

as independent confirmation for the basic result of the analysis presented in section 5.6, i.e. that measurement with an optical fiber at limited NA does not introduce any significant changes in the spectral shape of the diffuse reflectance.

5.8 Hemoglobin oxygen saturation

In this section, the ability of the model to measure the hemoglobin oxygen saturation parameter, α , is investigated. As mentioned in sections 2.3 and 4.9, the hemoglobin oxygen saturation is expressed as $100\alpha\%$, with $0 \leq \alpha \leq 1$. The amounts of oxy and deoxy hemoglobin present in tissue are determined by the partial pressure of oxygen present in the same environment, as explained in more detail in section 2.3. In order to observe the gradual transition from full oxygenated hemoglobin to fully deoxygenated and vice versa, a means to control the partial oxygen pressure is required. Under atmospheric pressure, and after equilibrium has been established, a solution of hemoglobin is fully oxygenated because the partial pressure of oxygen in the solution is equal to the partial pressure of the air above. This can be changed by bubbling the solution with an inert gas, a process which gradually reduces the partial pressure of oxygen in the solution. Another method is the introduction of a small amount of baking yeast [Hull and Foster 1997, Liu *et al* 1995] in the hemoglobin solution, which also gradually reduces the partial pressure of oxygen because yeast consumes the dissolved oxygen. This method has been chosen for the phantom experiments discussed in this section, because it provides a slow and steady conversion rate and it is easy to implement.

The phantoms were prepared with $1.07 \mu\text{m}$ polystyrene bead suspensions, 0.625 % total polystyrene by volume, and various amounts of hemoglobin. The partial pressure of oxygen was externally monitored with an oxygen-sensitive electrode (Microelectrodes, Inc, NH). Figure 5.15 shows spectra taken on a phantom with hemoglobin concentration 250 mg/dL, corresponding to the two extreme cases, (a) hemoglobin fully oxygenated (thin line), (b) hemoglobin fully deoxygenated (thick line). Note that the spectra exhibit the characteristic features of the oxy and deoxy hemoglobin (figure 2.2). The large absorption dip in the diffuse reflectance spectra is located at 415 nm for oxyhemoglobin

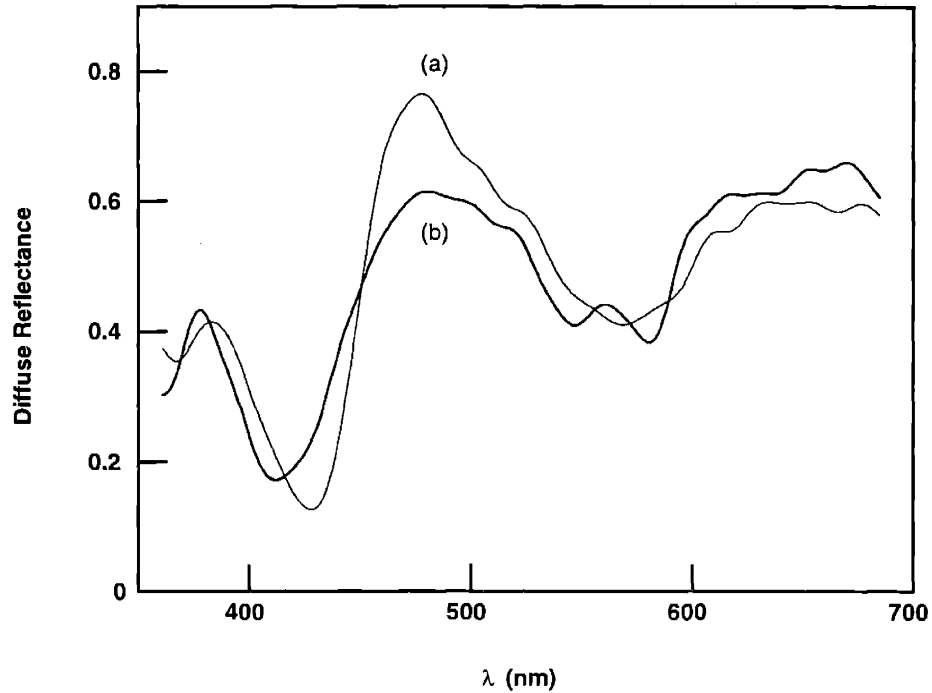


Figure 5.15: Spectra of phantoms containing (a) deoxyhemoglobin, and (b) oxyhemoglobin. Note the characteristic spectral features of the two hemoglobin types which are also shown in figure 2.2.

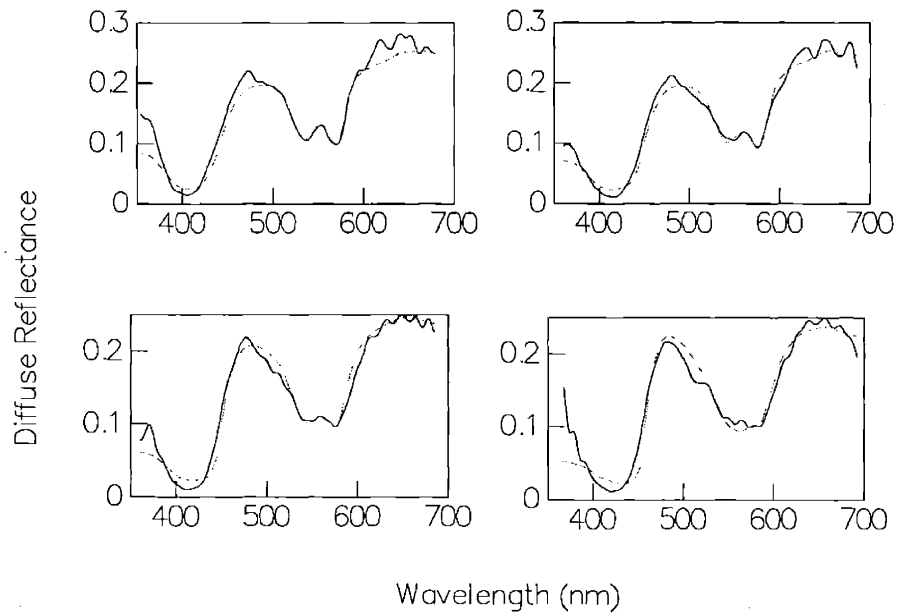


Figure 5.16: Diffuse reflectance spectra measured on phantoms for various values of hemoglobin oxygen saturation $\alpha=1.0$ (upper left), $\alpha=0.75$ (upper right), $\alpha=0.55$ (bottom left), and $\alpha=0.2$ (bottom right). Spectra indicated with dotted lines represent the predictions of the model.

and at 430 nm for deoxyhemoglobin. Also oxyhemoglobin exhibits the double absorption dip feature (542, 577 nm), which is absent in the deoxyhemoglobin case. Finally the total signal of deoxyhemoglobin at 430 nm is slightly less than that of oxyhemoglobin at 415 nm.

To observe intermediate states characterized by the presence of both oxy and deoxy hemoglobin, a higher hemoglobin concentration was used in the phantom (800 mg/dL). Figure 5.16 shows the spectra corresponding to various values of the parameter α : $\alpha=1.0, 0.7, 0.5,$ and 0.2 . The model predictions are also shown (dotted line). Note that the model describes the data well, and the value of the parameter α , can thus be determined. The spectroscopically determined parameter values were compared with the values corresponding to the partial pressure of oxygen measured (see section 2.3), and it was determined that α can in general be determined with an accuracy of approximately ± 0.05 .

5.9 Sampling depth

The definition and basic considerations concerning the sampling depth in tissue were presented in section 2.5. Results on the measurement of the sampling depth on tissue phantoms using the standard optical probe (section 3.2) will be presented here. To perform the measurements, the phantom was confined between two glass slides (microscope cover slips – see figure 5.17) which were approximately 140 μm thick and attached on a caliper so that their separation could be controlled with 10 μm precision. The glass slides were mounted horizontally, and the liquid phantom was inserted between the plates with a syringe and filled the gap completely due to surface tension.

The probe was placed in contact with one slide and spectra were collected by varying the thickness of the phantom in the 0-1000 μm range in steps of 50 μm . The phantom consisted of 1.07 μm polystyrene beads 0.625% by volume and 250 mg/dL hemoglobin. Figure 5.18 shows the intensity measured as a function of the phantom thickness for two representative wavelengths: (a) $\lambda=415$ nm ($\mu'_s=2.9$ mm^{-1} , $\mu_a=5.0$ mm^{-1}) and (b)

$\lambda = 685 \text{ nm}$ ($\mu'_s = 1.7 \text{ mm}^{-1}$, $\mu_a = 0.01 \text{ mm}^{-1}$). Note that the absorption coefficient value differs by two orders of magnitudes between these two cases. The diffuse reflectance intensity is constant as a function of phantom thickness and starts to drop at a thickness of approximately $400 \mu\text{m}$ for the 685 nm light, and at around $100 \mu\text{m}$ for the 415 nm light.

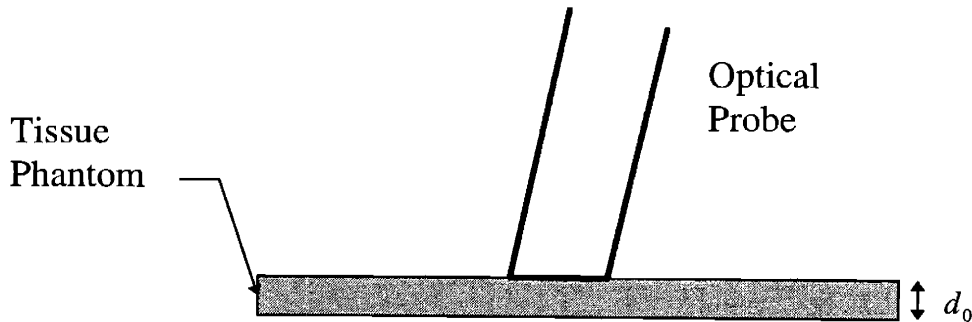


Figure 5.17: Tissue phantom geometry for sampling depth measurements.

The sampling depth is approximately equal to these thickness values, i.e. diffuse reflectance at 685 nm arises from a maximum depth of $400\text{-}500 \mu\text{m}$, while diffuse reflectance at 415 nm travels only a maximum of $100\text{-}150 \mu\text{m}$ deep in tissue. The large difference between the sampling depths of these two different wavelengths is due to the difference in the absorption coefficient. Using the expression for the average path length in tissue ($d_0 = 1/(\mu'_s + \mu_a)$) very good agreement is obtained with the above values of the sampling depth i.e. $d_0 = 125 \text{ mm}$ at $\lambda = 415 \text{ nm}$, and $d_0 = 588 \text{ nm}$ at $\lambda = 685 \text{ nm}$. This implies that the average path length of light is a very good estimate for the sampling depth, for this particular optical probe configuration.

These results confirm the initial hypothesis that diffusely reflected light measured in this study, mainly carries information about the mucosal layer which is the top layer of the colon tissue. This is in agreement with our initial objective i.e. we are interesting in probing the top one half millimeter of tissue (mucosal layer) which contains cells and is the location where precancerous changes first occur. As mentioned in section 2.5, the probe diameter and delivery/collection separation in general, affect the actual values of

the sampling depth. Even though the particular probe design employed in this study was not initially targeted toward investigations of colon mucosa, it turned out that the probe performed well in terms of enhancing the difference between the normal mucosa and the adenomatous polyp tissues, as we shall see in the next chapter.

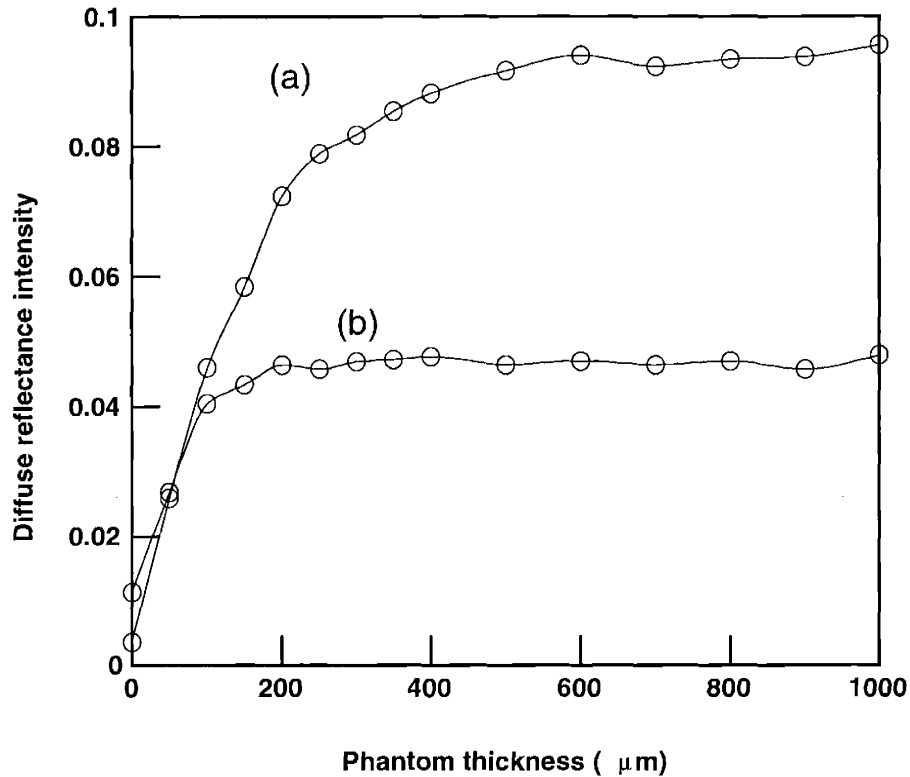


Figure 5.18: Diffuse reflectance intensity measured as a function of the phantom thickness for two different sets of optical parameters corresponding to two different wavelengths: (a) $\lambda = 415 \text{ nm}$ ($\mu'_s = 2.9 \text{ mm}^{-1}$, $\mu_a = 5.0 \text{ mm}^{-1}$) and (b) $\lambda = 685 \text{ nm}$ ($\mu'_s = 1.7 \text{ mm}^{-1}$, $\mu_a = 0.01 \text{ mm}^{-1}$). The sampling depth is defined as the depth at which the intensity starts to drop (approximately $500 \mu\text{m}$ at 685 nm , and $100 \mu\text{m}$ at 415 nm).

CHAPTER 6

DATA ANALYSIS

In the previous chapters, the fundamental issues regarding tissue optics were presented, together with various approaches in modeling diffuse reflectance from biological tissue which was modeled as a homogeneous semi-infinite turbid medium. Further examination of the specific details of the problem (delivery and collection of light through a fiber optic probe etc.) led to the development of a model suitable for describing the diffuse reflectance spectra from tissue, which were collected *in vivo* on human subjects. Detailed results of the data analysis using this model will be presented in this chapter. Prior to the application of the model developed in section 4.9 and tested on phantoms in chapter 5, the applicability of the simpler exponential model describing the total diffuse reflectance (presented in section 4.3) will be discussed.

6.1 Typical data and exponential model

Figure 6.1 shows typical diffuse reflectance spectra from three adenomatous polyp sites (located on the same polyp), and three normal mucosa sites located near the polyp. There are significant spectral differences readily observable between the two tissue types, especially in the blue region of the spectrum where the hemoglobin absorption valley around 420 nm is noted as the prominent spectral feature. This valley is much more prominent in the polyp spectrum which also shows a continuous decrease in intensity starting from the red end (~700 nm) and moving toward the green region (~500 nm) of

the spectrum, while in the same range the normal mucosa spectrum shows a steady increase in intensity. The secondary absorption dips of hemoglobin (542 and 577 nm) are much more prominent in the adenomatous polyp spectrum, indicating increased hemoglobin concentration, reduced scattering, or a combination of both of these effects.

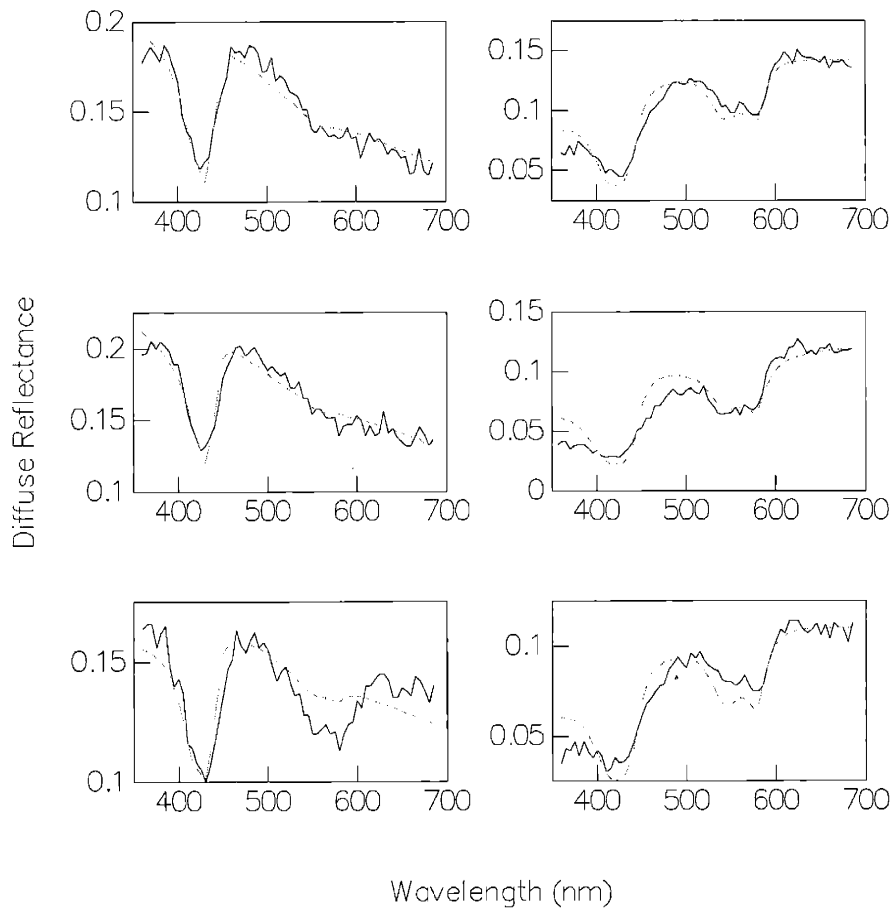


Figure 6.1: Typical diffuse reflectance data from 3 sites measured on an adenomatous polyp (right column), and 3 normal mucosa sites located near the polyp (left column). Data are indicated with continuous lines, and model fits using the exponential model (equation (6.1.2)) are shown with dotted lines. Note the very good agreement between the data and the model, despite the dramatic differences between the spectra of the two tissue types.

Closer inspection of the spectra shown in figure 6.1 reveals that both oxy and deoxy hemoglobins are present in the two tissue types, because the large absorption is located around 420 nm, which is between 415 nm (maximum oxyhemoglobin absorption) and 430 nm (maximum deoxyhemoglobin absorption). This also indicates that the concentration of oxyhemoglobin is likely to be larger than that of deoxyhemoglobin.

More detailed analysis presented in the next section, based on application of the model developed in section 4.9, will quantitatively confirm these observations.

The fact that normal and adenomatous polyp tissue diffuse reflectance spectra exhibit such distinct differences, indicates that there must be significant corresponding differences in the optical parameters characterizing these tissues. These differences can be found through the application of a physical model to analyze the data. A detailed physical model acts in that sense as the connection between the empirical level analysis of a qualitative examination of the spectral shapes, and the fully quantitative determination of the tissue optical properties. On an qualitative level, comparison between the spectral shapes of the typical tissue data shown in figure 6.1, and the tissue phantom data (figure 5.2), indicates that the great similarity between the features of the spectra shown in the two figures, serves as an indirect proof for the initial approximations made regarding the tissue optical parameters i.e. that absorption is mainly due to hemoglobin and that scattering can be modeled using spherical Mie scatterers.

Prior to application of the detailed model developed in section 4.9 to the data, it is interesting to examine how the simple exponential model presented in section 4.3 performs. This particular order of applying the two different models to analyze the data, apart from having a historical value (the exponential model was the first successful model to describe the data), it also points out important advantages and disadvantages of the two models, and provides a better perspective and intuition into the physical aspects of the problem and the underlying information.

The exponential model (equation 4.3.7) can be used to analyze the data in the following form

$$R(\lambda) = R_0 \frac{1}{1 + c_1 \frac{\mu_a(\lambda)}{\mu'_s(\lambda)}} \quad (6.1.1)$$

where $R(\lambda)$ is the experimentally determined tissue diffuse reflectance spectrum to be modeled, and c_1, R_0 , are parameters of the model. Refractive index mismatch conditions are absorbed in the parameter c_1 . In addition, the absorption coefficient $\mu_a(\lambda)$, is

considered to be a linear combination of the known oxy and deoxy hemoglobin absorption spectra (equation (2.3.1)). The reduced scattering spectrum, $\mu'_s(\lambda)$, is assumed equal to that measured on *in vitro* samples of normal colon mucosa (section 2.4). In this way, equation (6.1.1) can be applied to the data, and attempts to fit the data can be made by varying the three parameters c_1 , R_0 , and α . This simple model can successfully describe the adenomatous polyp data as shown in figure 6.1 where the thin lines correspond to fits using equation (6.1.1). However, only the hemoglobin oxygen saturation parameter, α , is a calibrated parameter here. The parameter c_1 measures the absorption/scattering ratio in arbitrary units, and R_0 is just an overall intensity parameter. In addition, because of the particular range of optical parameters found in adenomatous polyps, the scale invariance of the problem (discussed in section 4.1) is not completely broken, and thus equation (6.1.1) which is formulated in terms of the absorption/scattering ratio only, can be successfully applied to the data. The fact that scale invariance is not completely broken probably indicates that absorption in adenomatous polyps is high enough making collection of light by the probe very similar to the case where a probe with infinite radius is used.

In the case of the normal mucosa spectra however equation (6.1.1) fails completely. This failure may be attributed to increased scattering, decreased absorption, or a combination of both of these factors, as compared to polyp spectra. This can be qualitatively confirmed by inspection of the typical data shown in figure 6.1. A model suitable for description of the normal data should include a parameter with units of length which introduces the required scale invariance breaking.

The simplest model to try in such a case, is the generalization of the exponential model for two-layer systems (described in section 4.3). Assuming that $\mu'_s{}^{(2)} \gg \mu'_s{}^{(1)}$ (which essentially means that the second layer is assumed absent i.e. light reaching that layer has a very small chance to return back) the second term in equation (4.3.8) becomes negligible and the model has the following form:

$$R(\lambda) = R_0 \frac{1}{1 + c_1 \frac{\mu_a(\lambda)}{\mu'_s(\lambda)}} (1 - e^{-c_1(\mu_a(\lambda) + \mu'_s(\lambda))L}) \quad (6.1.2)$$

Equation (6.1.2) successfully describes the normal data as the fits to the normal data in figure 6.1 show (thin lines). The layer thickness parameter, L , introduces here the scale invariance breaking and it is actually connected more to the effects of the finite collection radius of the probe, rather than to the thickness of the top tissue layers (as it was initially introduced). It is in fact a complicated function of the tissue optical properties and the geometric characteristics of the optical probe. In that sense, it is a semi-empirical uncalibrated parameter, just like c_1 . Equation (6.1.2) can be equally well applied to fit the polyp data. In that case the parameter, L , turns out to be large enough so that the exponential term in (6.1.2) turns out to be very small.

Application of the model (6.1.2) to the data yields a set of four parameters (c_1, L, R_0, α). Parameter α which is already calibrated, provides meaningful information and will be discussed in detailed in the next section where the data analysis based on the diffusion model will be presented. Parameters, c_1 and L , are functions of the optical properties of tissue. It is interesting to examine their distributions which are shown in figure 6.2 in the form of a two-dimensional plot. Note that the normal data tend to form a well defined cluster, while the polyp data present a larger and variable spread and form a separate cluster. The parameter c_1 is larger for polyps, confirming the initial observation of increased hemoglobin concentration and/or decreased scattering.

This analysis, which was performed using the exponential model, is more advanced than a qualitative (empirical) inspection of the data because it employs a model and provides quantitative information, but it is still on a semi-empirical level, since the model parameters are unknown functions of the tissue optical properties (i.e. uncalibrated). The diffusion model presented in the next section eliminates these undesirable features and provides fully calibrated quantitative information. However, the simple exponential model performs very well in terms of describing the spectral lineshape of the tissue data.

When fitting the data is the only consideration, the simplicity of the exponential model makes it attractive.

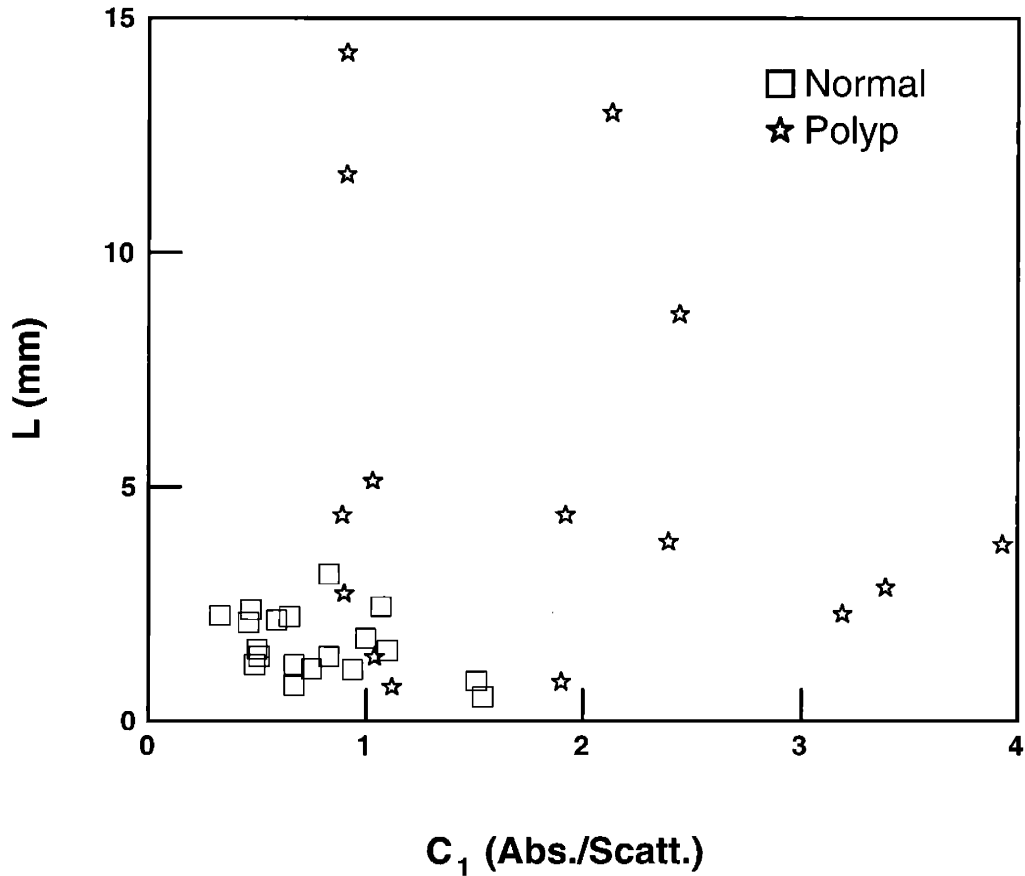


Figure 6.2: 2-dimensional plot of the two most important parameters of the exponential model: (a) c_1 parameter (x-axis), and (b) L parameter (y-axis). Note that even though these parameters do not have a simple physical interpretation, the data points corresponding to normal tissue (squares) tend to form a well defined cluster, while the adenomatous polyp data points (asterisks) present a wider and variable spread.

6.2 Optical probe model

The diffusion model is formulated in terms of the four calibrated parameters: (a) total hemoglobin concentration, (b) hemoglobin oxygen saturation, (c) scatterer density, and (d) scatterer diameter, (c_{Hb}^* , α , ρ_s , d_s , respectively). The model is applied to the data in a stepwise manner as explained in section 4.9, to obtain the absorption parameters c_{Hb}^* and α first, and then the scattering parameters ρ_s , d_s . Prior to presenting the results of the

data analysis, the procedure followed will be illustrated, by applying the model to one typical adenomatous polyp spectrum and one typical normal tissue spectrum, selected from the spectra shown in figure 6.1.

Figure 6.3 shows the scattering spectra $\mu'_s(\lambda)$ calculated from the typical diffuse reflectance spectra by numerically inverting equation 4.9.2. The best Mie theory fits are also shown (thin lines). The main difference between the spectra of the two tissue types is observed in the spectral slope, which corresponds to a different effective scattering size, $d_s = 1.5 \mu\text{m}$ for the polyp and $d_s = 0.35 \mu\text{m}$ for normal mucosa. The values for the scatterer densities were $\rho_s = 15 \times 10^8 \text{ mm}^{-3}$ for the normal mucosa and $\rho_s = 1.3 \times 10^8 \text{ mm}^{-3}$ for the adenomatous polyp. The normal mucosa spectrum was characterized by hemoglobin concentration $c_{Hb}^* = 22.5 \text{ mg/dL}$, while the corresponding value for the adenomatous polyp was about 6 times higher ($c_{Hb}^* = 165 \text{ mg/dL}$). The hemoglobin saturation was found to be $\alpha = 0.65 \pm 0.05$, and $\alpha = 0.55 \pm 0.05$ for the normal mucosa and the adenomatous polyp spectra respectively. These results are in agreement with the empirical qualitative observations made by initial visual inspection of the spectra, and with the semi-quantitative results of the exponential model; the diffusion theory model allows a direct quantification of the empirical observations, in terms of the model parameters.

Figure 6.4 shows the best model fits to the data, using the model in a forward way to calculate the diffuse reflectance spectrum, and having c_{Hb}^* , α , and $\mu'_s(\lambda)$ as inputs. The $\mu'_s(\lambda)$ spectra used are the Mie theory fits from figure 6.3. The model describes the data in an accurate way, despite the dramatic differences noted in the spectral shape between the two tissue types and the fact that $\mu'_s(\lambda)$ is approximated assuming a homogeneous distribution of spherical scatterers. The deviation between the data and the model is typically smaller than 10% for most of the wavelength range. This result, together with the result of figure 6.3 shows that Mie theory successfully describes the reduced scattering spectra of colon tissue.

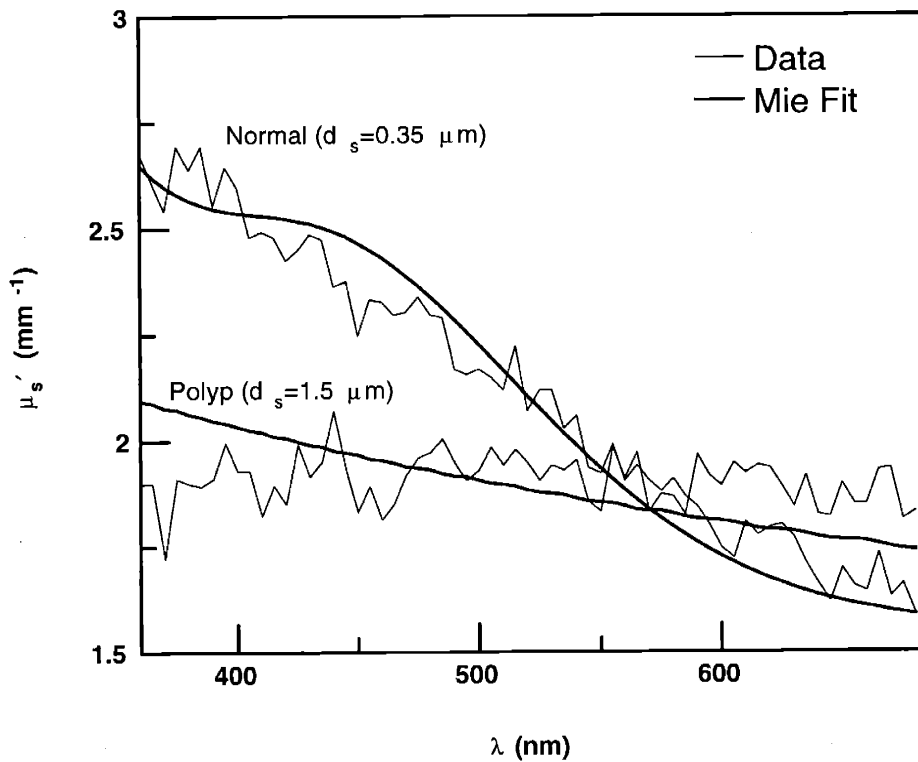


Figure 6.3: Scattering spectra obtained from the data shown in figure 6.4 (thin lines), and best fits using Mie theory (thick lines). The Mie theory fits assign an effective scatterer size d_s to the scattering spectra. The polyp is characterized by a larger effective scatterer size ($d_s = 1.5 \mu\text{m}$) as compared to normal mucosa ($d_s = 0.35 \mu\text{m}$).

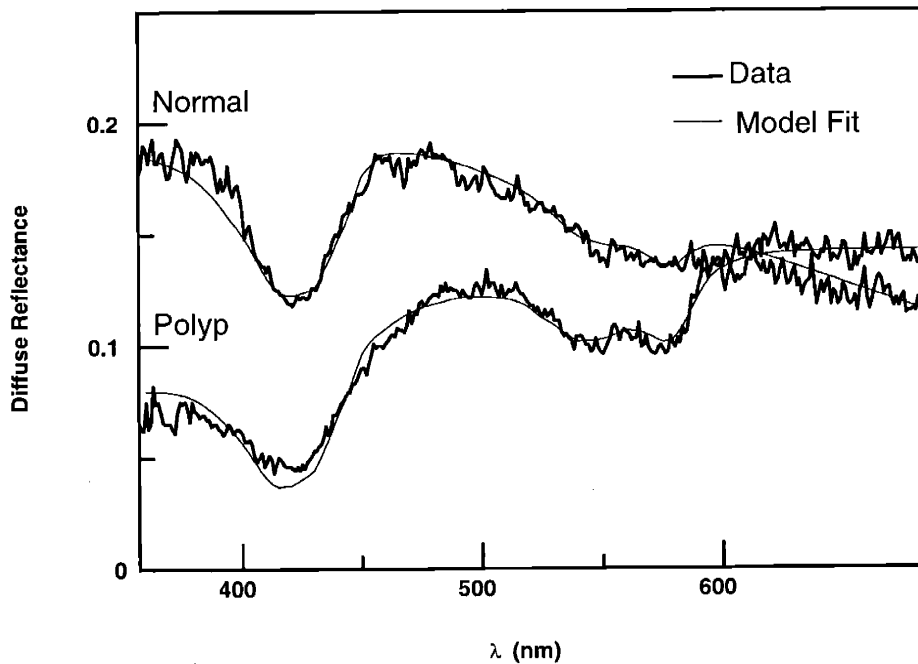


Figure 6.4: Typical normal and adenomatous polyp spectra (thick lines), and best fits to the data using the model (thin lines) and Mie theory to approximate the reduced scattering coefficient.

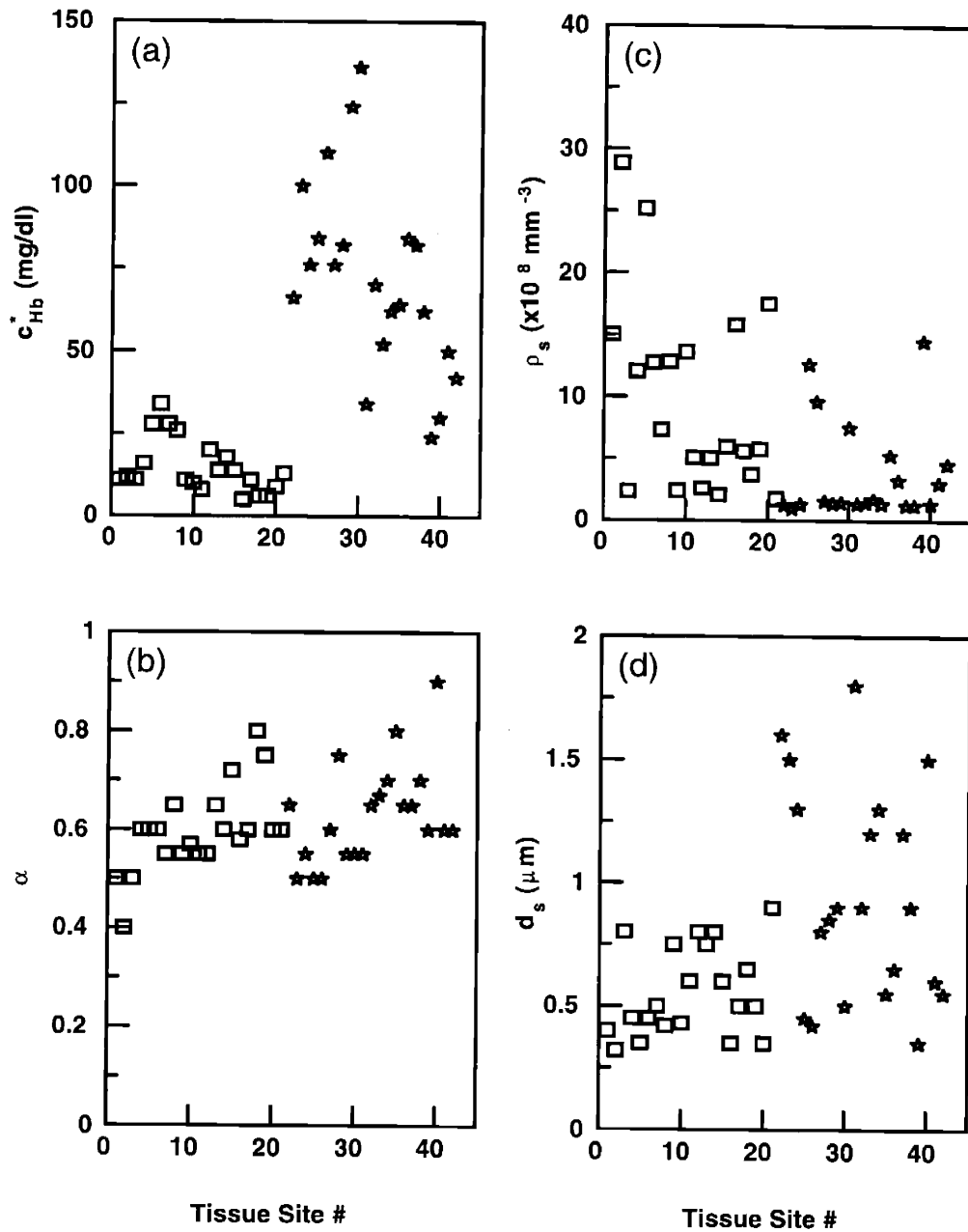


Figure 6.5: Model parameters obtained from data analysis: (a) total hemoglobin concentration, c_{Hb}^* , (b) hemoglobin oxygen saturation, α , (c) effective scatterer density, ρ_s , and (d) effective scatterer size, d_s . The largest difference between normal mucosa (squares) and adenomatous polyps (stars) is observed in the total hemoglobin concentration.

Figure 6.5 shows the calculated values of the four parameters for all tissue sites studied: (a) total hemoglobin concentration c_{Hb}^* , (b) hemoglobin oxygen saturation α , (c) effective scatterer density ρ_s , and (d) effective scatterer size d_s . Adenomatous polyps

were clearly characterized by increased hemoglobin concentration, while there were no observable differences in terms of the hemoglobin oxygen saturation. The effective scatterer density was in general lower in adenomatous polyps, and the effective scatterer size larger, even though there was significant overlap of these parameter distributions between the two tissue types.

Figure 6.6 shows a plot of the hemoglobin concentration c_{Hb}^* , vs. the effective scatterer size d_s . These two parameters are shown together in order to summarize and illustrate the differences found in the scattering and absorption properties of normal mucosa and adenomatous polyps in the colon. Note that the normal mucosa data tend to form a cluster, while the adenomatous polyp data are characterized by a wider spread and irregular distribution, in both the effective scatterer size and the hemoglobin concentration.

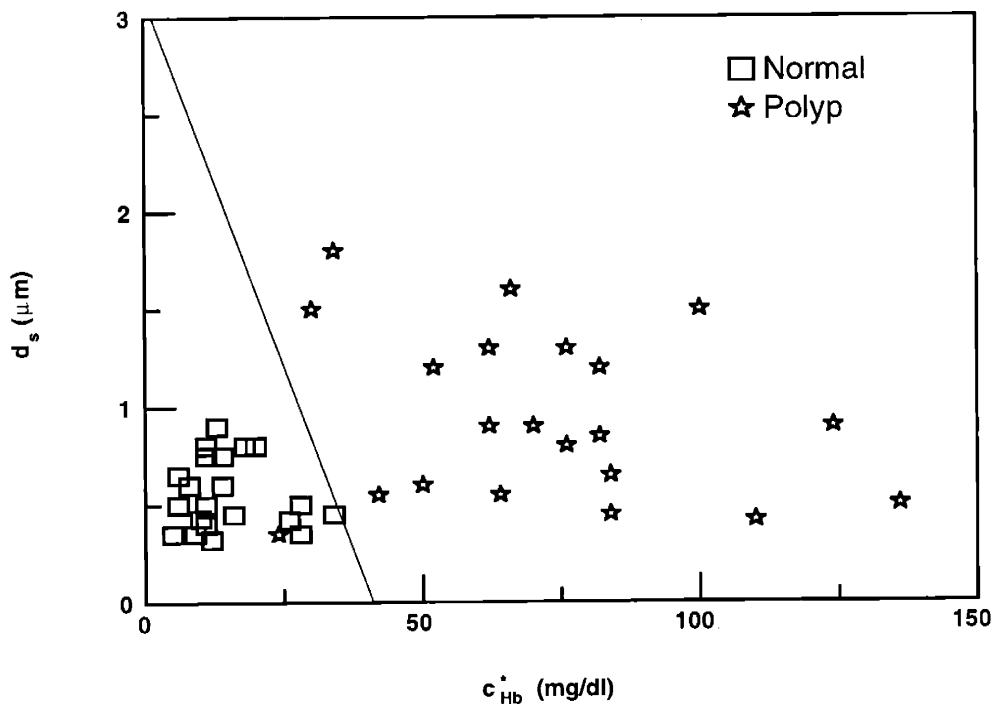


Figure 6.6: Binary plot of the total hemoglobin concentration c_{Hb}^* vs. the effective scatterer size d_s . The normal data tend to form a well defined cluster, while the adenomatous polyp data are marked by wider variation. The straight line is a decision line separating the two types of tissue, drawn using logistic regression analysis (see section 6.3).

6.3 Statistical analysis of model parameters

Table 6.1 summarizes the results by giving the average values and the standard deviations for each parameter, for the two tissue types examined. Based on the information presented in Table 6.1, it can be easily seen that the total hemoglobin concentration is clearly different for the two tissue types. This is not true for the hemoglobin oxygen saturation where the mean values are almost identical. Finally, the separation for the two scattering parameters, density and size, is clear for the mean values, but if the standard deviations are examined, there is significant overlap between the values for the two tissue types.

Table 6.1: Average values and standard deviations for the model parameters.

Model Parameter	Normal	Adenomatous Polyp
Total Hb Concentration c_{Hb}^* (mg/dL)	13.6±8.8	72.0±29.2
Hb Oxygen Saturation α	0.59±0.08	0.63±0.10
Effective Scatterer Density ρ_s ($\times 10^8$ mm ⁻³)	9.2±7.5	3.5±4.0
Effective Scatterer Size d_s (mm)	0.56±0.18	0.94±0.44

The ability of each parameter to indicate a particular tissue type can be further investigated using logistic regression [Hosmer and Lemeshow 1989]. A commercially available statistical software package [Statacorp. 1997] was used to implement this analysis technique, and a probability was assigned to every parameter value. This probability indicated the tissue type which the tissue site under study was most likely to belong to. For example, using the total hemoglobin concentration parameter, logistic regression assigned a probability to every hemoglobin concentration value which

indicated whether the tissue site was normal ($p_{c_{Hb}}^* = 0$) or adenomatous ($p_{c_{Hb}}^* = 1$). Figure 6.7 is a plot of this probability distribution. Note that the normal data points (circles) are clustered in the low hemoglobin concentration region, while the adenomatous polyp data points (asterisks) are located in the high concentration region. Between the two ranges, there is a transition range where a few data points fall. If $p_{c_{Hb}}^* = 0.5$ is set as the threshold between the two tissue types, then there is one normal point that is misclassified as adenomatous polyp, and two adenomatous polyp point misclassified as normal, while the rest of the data are correctly classified. In that sense, it is possible to identify hemoglobin concentration as a statistically reliable indicator of whether a tissue site is normal or adenomatous.

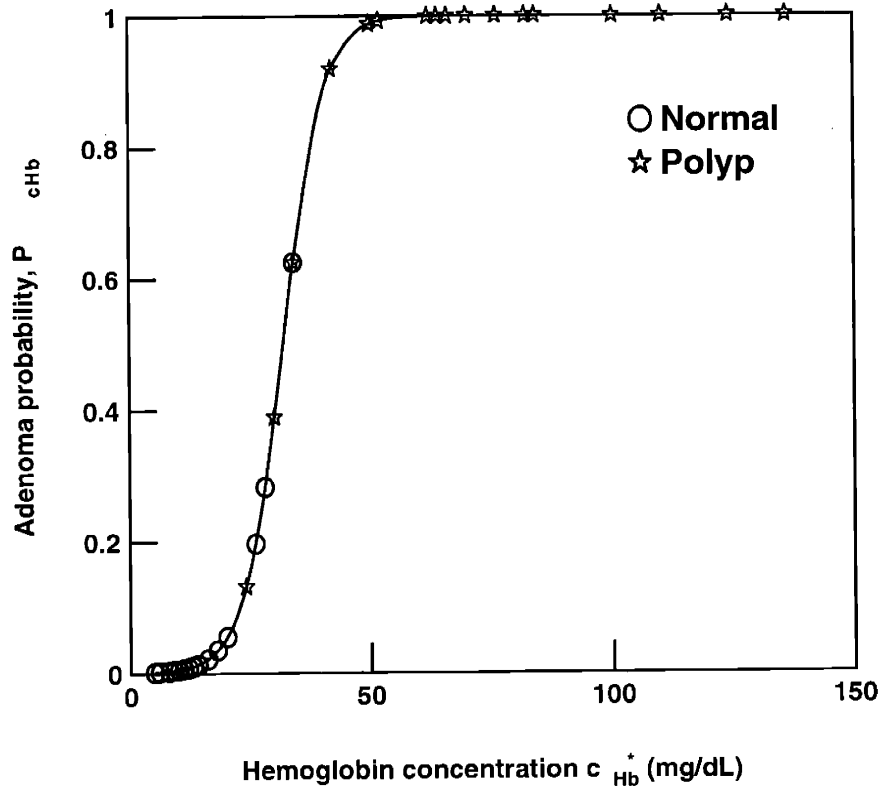


Figure 6.7: Probability distribution of the hemoglobin concentration indicating adenomatous polyp ($p_{c_{Hb}} = 1$) or normal mucosa ($p_{c_{Hb}} = 0$).

Similar analysis for the other three parameters reveals that the hemoglobin oxygen saturation has practically no predicting ability for distinguishing the two tissue types, which is expected based on the values of the mean and the standard deviation shown in

Table 6.1. In the same way, the two scattering parameters offer some predicting ability but not as good as the hemoglobin concentration. Logistic regression provides the parameter R^2 which is a measure of how well a parameter can distinguish between the two tissue types. This parameter varies in the range $0 \leq R^2 \leq 1$ with $R^2 = 0$ indicating practically no ability to distinguish and $R^2 = 1$ indicating perfect predicting ability. Table 6.2 summarizes these results for the R^2 values of all the parameters. Note that it is possible to combine two or more parameters in the decision making process. The maximum distinguishing capability is obtained when all four parameters are used, but essentially all the predicting power is due to the a combination of the total hemoglobin concentration and the scatterer size. This is in agreement with figure 6.6 which nicely illustrates this point. The straight line in figure 6.6 is the optimum separation line that can be drawn to separate the two tissue types, based on logistic regression analysis. Note that such a line could be easily drawn by hand based on just a qualitative inspection of the data. Logistic regression provides a formal mathematical methodology for separating the data in different types (i.e. providing a diagnosis) which can be especially in cases where there several data types characterized by many parameters.

Table 6.2: Discriminating ability of model parameters in terms of the R^2 quantity obtained through logistic regression.

Model Parameter	R^2
Total Hb Concentration, c_{Hb}^*	0.808
Hb Oxygen Saturation, α	0.023
Effective Scatterer Density , ρ_s	0.174
Effective Scatterer Size, d_s	0.228
c_{Hb}^*, d_s	0.846
$c_{Hb}^*, \alpha, \rho_s, d_s$	0.851

6.4 Discussion

A diffusion theory model has been successfully employed to describe the tissue diffuse reflectance as measured by an optical fiber probe *in vivo*. The model is relatively simple from a mathematical point of view, yet it has the ability to spatially resolve the diffuse reflectance on the surface of a turbid medium, as required for modeling light delivery and collection through an optical fiber probe. By utilizing appropriate approximations, the model is expressed in an analytical form which is amenable to numerical inversion. Finally, the validity of the model was found to extend over a wide range of absorption values, covering the entire range of values found in colon mucosa, and it was determined that the model holds as far as absorption does not significantly exceed scattering.

A major feature of the model is the implementation of light collection by a fiber optic probe. The radius r_c of the probe collection area (discussed in section 4.9) is a parameter of the model, and can be used to describe different probe configurations. The importance of this parameter lies in the fact that it defines the probe's sensitivity to absorption. Spectra collected by a probe with large r_c will be more sensitive to tissue absorption as compared to spectra collected by a probe with a smaller r_c . This is evident from the analysis on tissue phantoms presented in section 5.4, and from the tissue data shown in figure 6.1, where the secondary absorption peaks of hemoglobin are barely noticeable in the normal mucosa spectrum; a probe with larger r_c would make these features more prominent.

The above attributes of the model make it attractive and appropriate for describing the diffuse reflectance from biological tissues. Other researchers have already used variants of this model in the study of diffuse reflectance from tissues and tissue phantoms in the IR range [Liu *et al* 1995, Hull and Foster 1997]. The present study is, to our knowledge, the first one to apply it to *in vivo* human mucosal tissue diffuse reflectance in the visible range, using an optical fiber probe. By working in the visible instead of the IR range of the spectrum, light penetration was restricted to approximately 0.5 mm, which focused on the important tissue layer (mucosa) where precancerous changes occur. Using

the model, we have shown that it is possible to obtain quantitative information characterizing the tissue studied, such as hemoglobin concentration, hemoglobin oxygen saturation, effective scatterer size, and effective scatterer density. These tissue parameters were calculated for normal mucosa and adenomatous polyps in the colon. The information obtained shows that diffuse reflectance may be potentially useful for the *in vivo* analysis of biological tissues, and ultimately, for the detection of disease.

The basic approximation made in the model is that, hemoglobin is the major absorber in the visible range of the spectrum. Even though there is no direct proof for such an assumption, the fact that the diffuse reflectance spectra measured on tissue strongly exhibit the characteristic features of the hemoglobin absorption spectrum clearly indicates that hemoglobin is a major absorber. In addition, the diffuse reflectance spectra measured on tissue phantoms in which hemoglobin was the only absorber closely resemble the tissue data. Finally, to our knowledge, there are no published reports identifying major light absorbers in tissue other than hemoglobin and melanin. Melanin is found only in skin, which leaves hemoglobin as the major absorber in the case of colon tissue, and in the case of mucosal tissues in general.

In a similar way, tissue scattering was modeled as if caused by perfectly spherical scatterers with known refractive index. This approximation, which obviously does not reflect the actual picture of the microscopic origin of tissue scattering, permits however the convenient quantitative characterization of the scattering properties in terms of basic parameters such as the effective scatterer size and the effective scatterer density. These parameters provide an estimate of the average scattering properties of tissue and facilitate comparison between different tissue types (in this particular case, normal mucosa vs. adenomatous polyps). The fact that the spectra measured on tissue phantoms reproduce accurately and consistently the real tissue spectra, serves again (as in the case of hemoglobin), as an indirect confirmation for the validity of this approximation.

According to the data analysis, adenomatous colon polyps were found to be characterized by increased hemoglobin concentration. It is known that tumors and cancerous tissues exhibit increased microvasculature, and hence increased blood content

[Jain 1988]. It is also reported, using morphometry and vascular casting in combination with scanning electron microscopy techniques, that precancerous tissues such as adenomatous polyps of the colon are also characterized by increased microvascular volume [Skinner *et al* 1995, Tipoe and White 1995]. Our results are in good agreement with these reports, confirming their findings by observing increased hemoglobin concentration in adenomatous colon polyps. Other researchers report increased microvasculature of the colon mucosa associated with Crohn's disease [Carr *et al* 1986] and ulcerative colitis [Tsujii *et al* 1995]. Even though these tissue types were not included in the present study, the technique employed here could prove useful for the *in vivo* study of these diseases.

The hemoglobin oxygen saturation was found to be on average approximately 60% for both normal mucosa and adenomatous polyps. This result is reasonable, since the measurements were essentially performed in the capillary blood vessel network of the mucosa i.e. within the first one half millimeter below the tissue surface. Oxygen is transferred from hemoglobin to tissue in the capillaries, therefore hemoglobin oxygen saturation drops within the capillaries from approximately 97% (arterial blood) to about 40 % (venous blood) [Horrobin 1968]. The measured values which were around 60-70%, fall in the middle of this range. Even though we are not aware of any published *in vivo* measurements of hemoglobin oxygen saturation in adenomatous colon polyps with which to compare our findings, the fact that there was no difference observed between adenomatous polyps and normal mucosa in terms of the Hb oxygen saturation can probably be attributed to the fact that adenomatous polyp metabolism is not significantly altered, so as to introduce changes in Hb oxygenation. On the other hand, it is known that tumors are in general characterized by abnormally low Hb oxygenation [Vaupel 1996], which is probably related to the disturbed metabolism of such tissues. The technique presented here could be used *in vivo* for the assessment and study of tumors or for the study of other tissue types when knowledge of Hb saturation is required.

Finally, we have observed an intrinsic differentiation in the scattering properties between the two tissue types studied. For adenomatous polyps, the average effective scattering size was found to be larger, and the average effective scatterer density was

found to be smaller, as compared to normal mucosa. The exact details of how scattering arises in tissue are not very well known. There are a number of hypotheses attributing scattering to various microstructures, both extracellular such as collagen fibers [Ferdman and Yannas 1993], and intracellular such as mitochondria [Beauvoit *et al* 1994] and cell nuclei [Perelman *et al* 1998]. Further investigations into the origins of elastic light scattering in tissues is needed to provide the explanation for the differences observed in the present study. One possible explanation could be the fact that contributions to light scattering from intracellular structures is increased in adenomatous polyps because cells occupy a higher volume ratio. In addition, the submucosa, in which collagen is more densely packed [Thomson *et al* 1986] than it is in the mucosa, is usually located too far away from the polyp surface in order to be able to contribute to light scattering. This could explain the lower scatterer density in adenomatous polyps, provided that intracellular scatterers are larger than extracellular ones, on average. These hypotheses remain to be investigated by more detailed studies. Nevertheless, these observations could prove useful for the detection of precancerous conditions because these are usually characterized by cellular proliferation, and hence increased volume occupied by cells in tissue.

The present model assumes the tissue to be a semi-infinite homogeneous turbid medium, and provides information in that approximation. In the case of the colon, and especially for non-polypoid tissues, an improved model would take into account the tissue layered structure. In particular, a model taking into account the top two layers (mucosa, submucosa) independently is expected to provide relevant information about specific tissue layers. For example, when looking for early precancerous changes, one would want to focus on the study of the mucosal layer rather than other deeper layers, because this is where these changes first appear.

In summary, we have demonstrated the potential of diffuse reflectance spectroscopy to obtain quantitative biochemical (hemoglobin) and morphological (scatterers) information *in vivo* and in real time. We expect that further development of the technique could increase the quantity, quality, and accuracy of the information obtained. We are currently investigating such prospects and we have already reported on a related

technique which is capable of detecting the size and density of cell nuclei *in vivo* [Perelman *et al* 1998].

CHAPTER 7

CONCLUSIONS & FUTURE DIRECTIONS

7.1 Conclusions and thesis accomplishments

In this study we have dealt with the task of obtaining tissue information based on the analysis of diffuse reflectance spectra. To accomplish this task a methodology was developed consisting of the following parts: (i) a physical model describing diffusive light propagation in tissue, (ii) two fundamental approximations regarding colon tissue optics, attributing absorption to hemoglobin, and scattering to spherical microparticles, and (iii) implementation of data collection through the use of an optical probe with a well defined delivery/collection geometry which facilitated the independent determination of the scattering and absorption coefficients of tissue. Furthermore, to test the consistency and validity of this modeling approach, tissue simulating materials (phantoms) were build implementing the two fundamental approximations i.e. hemoglobin for absorption and polystyrene microspheres for scattering. Spectra measured on the phantoms closely resembled those measured on real tissue, which confirmed the validity of our modeling approach.

In summary, this study has shown that: (a) it is possible to measure the optical properties of human colon tissue *in vivo* by employing a physical model describing the tissue diffuse reflectance, and (b) the optical properties measured can be correlated with the biochemical and morphological composition of tissue, which can be useful for the detection of disease. Even though the results of the study are very promising in terms of

these fundamental observations, several aspects of the tissue analysis technique presented here need to be investigated further in order to make the technique more accurate, reliable, and flexible. In addition to possible refinements, several alternative and more general prospects open for tissue analysis, having this study as the starting point.

7.2 Application to other tissue types

In this study, human colon tissue has been investigated *in vivo* using diffuse reflectance spectroscopy. The results indicate that the same technique could be applied for the analysis of other tissue types of the human body, particularly those on the surfaces of the internal hollow organs. The gastrointestinal (GI) tract (oral cavity, esophagus, stomach, intestines) is a potential ground for future applications of the method described here. The general structure and morphology of the GI tract is such, so as to permit application of *in vivo* diffuse reflectance spectroscopy for the early diagnosis of cancer and other pathological conditions. In addition, other hollow organs such as the bladder could be investigated.

In the case of colon, there are two particular tissue types which would be interesting to investigate with the presented technique. The first is a special type of polyps, the *hyperplastic* polyps [Ming and Goldman 1992, Fenoglio-Preiser *et al* 1989]. These polyps appear under gross examination to be very similar to adenomatous polyps examined in this study, but histologically are not classified as dysplastic and are essentially harmless because they do not evolve into cancer. It would be very interesting to investigate the possibility of discriminating hyperplastic from adenomatous polyps *in vivo* using diffuse reflectance. Preliminary results on two hyperplastic polyps indicate that they appear similar to the adenomatous polyps, based on the analysis of the parameters of the diffuse reflectance model, but a more detailed study examining a larger number of hyperplastic polyps would be required to draw definite conclusions.

The other type of pathological condition which arises in the colon and could be immediately studied with the present technique is *Ulcerative Colitis* [Tsujii *et al* 1995].

This is an extended chronic inflammation of the colon mucosa, of unknown etiology, which frequently leads to cancer. Due to the fact that inflammation is involved i.e. potential increase in Hb concentration, ulcerative colitis could be detected and characterized by the present method. Because this condition covers rather extended areas of the colon mucosa it would be interesting to study it with a generalization of the present technique which employs imaging, to survey large tissue areas.

7.3 Real time data acquisition & analysis - imaging techniques

In this study, it has been shown that it is possible to obtain quantitative tissue information, by analyzing the diffuse reflectance spectra of tissue using an appropriate model. However, because of the preliminary character of this study, data were collected *in vivo* but analyzed at a later time. An obvious step in making the technique much more powerful would be to implement data analysis in *real time*. In such a case, important tissue information would be available immediately during endoscopic examination and diagnostic decisions could be made based on this information. For example, conventional biopsy techniques could be directed towards the tissue sites suspected for disease, instead of employing the present day random biopsy scheme. This would reduce the number of biopsy samples collected, therefore making the biopsy process more cost efficient with the simultaneous reduction of stress and discomfort to the patient. In addition, diseased tissue areas could be identified, which would otherwise evade detection.

The presented study employed an optical fiber probe to deliver and collect light. The average optical properties were measured from a tissue volume of approximately one cubic millimeter. This is a relatively small tissue volume; cancer surveillance usually requires the examination of extended surface areas of the internal hollow organs of the human body. Such a task becomes impractical when using an optical probe similar to that employed in the present study. For this reason, an imaging system is required capable of examining relatively wide areas of tissue, and also capable of measuring the diffuse reflectance spectra corresponding to every tissue spot. Such a system could be used for

the quick and efficient examination of tissues for cancer surveillance and possibly for other diseases.

Imaging systems have been already developed for the detection of tissue fluorescence signals [Wang 1996]. This last system was employed to study the human colon, using adenomatous polyps as a test ground in a manner similar to this study. The results were promising, but the system provided limited capability for resolving various wavelengths of the light collected from tissue i.e. limited spectroscopic capability. A generalized version of this system combining diffuse reflectance spectroscopy with imaging of extended tissue areas could prove a powerful tool for early diagnosis of cancer. Such a system would be capable of producing an image of the tissue optical properties in real time, with the additional option of producing an image of the cell nuclear size and density distributions. To implement such a device however, the difficult problem of obtaining spectroscopic information on pixel by pixel basis would have to be solved first.

7.4 Additional tissue information

The present model assumed the tissue to be a semi-infinite homogeneous turbid medium. This is clearly an approximation; the real tissue is composed of several layers, as discussed in the introduction. Although light propagation is mainly confined to the top layers, some small part of it penetrates into the submucosa which due to its distinctly different morphology and composition [Thomson *et al* 1986] is expected to be characterized by different optical properties, as compared to the mucosal layer. A model that explicitly takes into account the tissue layered structure would be able to provide more specific information in terms of the variation of the tissue optical properties as a function of depth in tissue. This information could prove very important for the detection of cancer, because it is known that the early precancerous changes occur in the mucosa, while frank cancer is usually characterized by invasion of the submucosal layer.

Attempts to develop a two-layer diffuse reflectance model have been reported [Takatani and Graham 1979, Swathi *et al* 1987, Dayan *et al* 1992] but unfortunately, these models are mathematically complicated requiring extensive numerical calculations, and providing little flexibility and insight into the physics of the problem. However, an optimized version of these models, or a new model based on photon migration or path integral techniques could prove more appropriate for application to tissue diffuse reflectance problem.

In addition to the generalization of the model for the description of multilayer tissues, the model parameters can be also generalized in a way that it would be able to provide more specific information. For example, the spherical scatterer approximation of fixed diameter, d_s , employed in this study, can be modified in a way such that a distribution of scatterer sizes is obtained. This would be closer to the realistic case since it is known that tissue scattering arises from a variety of microstructures and organelles, and it would also provide more specific and accurate information.

As already reported [Perelman *et al* 1998] it is possible to measure the size and density of the cell nuclei located in the mucosal layer of esophagus tissue using diffuse reflectance spectroscopy. This technique is based on modeling techniques presented in section 6.1. In particular, careful inspection of the model fits in figures 6.1. and 6.4 illustrates the nature of the imperfect fit of the model. If the model fit is subtracted from the actual tissue data, a periodic residual remains which is due to scattering by cell nuclei. Analysis of this residual enables the calculation of the nuclear size distribution and the nuclear size density.

The ability to measure these quantities is of fundamental importance for the early detection of cancer. One of the main characteristics of precancerous formations in tissue, is the increase in size and density of cell nuclei located in the epithelium of most of the hollow body organs. Early detection using diffuse reflectance spectroscopy, could lead to prevention of cancer by timely removal of the affected tissue areas. Refinements in the modeling approaches presented in this thesis, could lead to improved and more accurate determination of the size and density of the cell nuclei.

7.5 Probe geometry

In chapter 5 it was shown that the probe geometry is very important in terms of defining the exact sampling depth characteristics, the overall intensity of the light collected, and finally the extent at which absorption affects the observed spectra. Even though this study employed a well defined optical probe geometry (described in detail in chapter 3), the fundamental observations made about the basic characteristics of the optical probe, can be used for the efficient design of new optical probes, tailored for a particular application.

For example, a probe with large diameter could be used to both increase the amount of total light collected and the absorption sensitivity of the probe. In contrast, a small diameter probe such a probe which employs the same optical fiber for both delivery and collection of the light would be more sensitive in terms of detecting the backscattered light. In a similar way, probe characteristics for fluorescence spectroscopy can be defined, which are expected to be qualitatively the same as those of the diffuse reflectance case, but more detailed analysis is needed to isolate the differences between fluorescence and diffuse reflectance.

7.6 Fluorescence spectroscopy

Several research groups have investigated colon tissue employing fluorescence spectroscopy [Cothren *et al* 1996, Schomacker *et al* 1992, Kapadia *et al* 1990], in a way very similar to that of the present study i.e. by studying adenomatous polyps. Fluorescence spectroscopy has the potential to offer more detailed and specific information as compared to diffuse reflectance spectroscopy [Zonios *et al* 1996]. However, modeling of the light propagation process is more complicated since both exciting and emitted fluorescence light must be modeled appropriately. In addition, detailed knowledge about the nature of the intrinsic fluorescence of the tissue is required. Diffuse reflectance spectroscopy can be a useful ancillary method for modeling light transport processes involved in fluorescence spectroscopy. For instance, tissue optical

properties can be first determined using diffuse reflectance and this knowledge can then be applied to modeling the propagation of the fluorescence excitation and emission signals. In this way, the intrinsic tissue fluorescence can be measured. One such example which characteristically illustrates the connection between modeling of diffuse reflectance and calculation of the intrinsic fluorescence has been already reported [Wu *et al* 1993b].

APPENDIX

DERIVATION OF THE DIFFUSION EQUATION FOR LIGHT PROPAGATION IN TURBID MEDIA.

We begin with the radiative transport equation (A.1) [Ishimaru 1978]

$$\hat{s} \cdot \nabla I(\vec{r}, \hat{s}) = -(\mu_s + \mu_a) I(\vec{r}, \hat{s}) + \mu_s \int_{4\pi} p(\hat{s}, \hat{s}') I(\vec{r}, \hat{s}') d\omega' \quad (\text{A.1})$$

and the diffusion approximation (A.2) for the specific intensity $I(\vec{r}, \hat{s})$

$$I(\vec{r}, \hat{s}) = \frac{1}{4\pi} \phi(\vec{r}) + \frac{3}{4\pi} \vec{F}(\vec{r}) \cdot \hat{s} \quad (\text{A.2})$$

Substituting the diffusion approximation (A.2) into (A.1) we have:

$$\begin{aligned} \hat{s} \cdot \nabla \left(\frac{1}{4\pi} \phi(\vec{r}) + \frac{3}{4\pi} \vec{F} \cdot \hat{s} \right) = & -(\mu_s + \mu_a) \left(\frac{1}{4\pi} \phi(\vec{r}) + \frac{3}{4\pi} \vec{F} \cdot \hat{s} \right) \\ & + \mu_s \int_{4\pi} p(\hat{s}, \hat{s}') \left(\frac{1}{4\pi} \phi(\vec{r}) + \frac{3}{4\pi} \vec{F} \cdot \hat{s}' \right) d\omega' \end{aligned} \quad (\text{A.3})$$

Multiplying (A.3) by \hat{s} and integrating over $d\omega$ we have:

$$\begin{aligned}
\int_{4\pi} \hat{s} \left\{ \hat{s} \cdot \nabla \left(\frac{1}{4\pi} \phi(\vec{r}) + \frac{3}{4\pi} \vec{F} \cdot \hat{s} \right) \right\} d\omega &= -(\mu_s + \mu_a) \int_{4\pi} \hat{s} \left(\frac{1}{4\pi} \phi(\vec{r}) + \frac{3}{4\pi} \vec{F} \cdot \hat{s} \right) d\omega \\
&+ \frac{\mu_s}{4\pi} \phi(\vec{r}) \int_{4\pi} p(\hat{s}, \hat{s}') d\omega' \int_{4\pi} \hat{s} d\omega \\
&+ \frac{3}{4\pi} \mu_s \int_{4\pi} p(\hat{s}, \hat{s}') (\hat{s} \cdot \hat{s}') d\omega' \int_{4\pi} \hat{s} (\vec{F} \cdot \hat{s}) d\omega
\end{aligned} \tag{A.4}$$

(A.4) becomes:

$$\frac{1}{3} \nabla \phi(\vec{r}) = -(\mu_s + \mu_a) \vec{F}(\vec{r}) + \mu_s g \vec{F}(\vec{r}) \tag{A.5}$$

or

$$\vec{F}(\vec{r}) = -D \nabla \phi(\vec{r}) \text{ with } D = \frac{1}{3(\mu_a + (1-g)\mu_s)} \tag{A.6}$$

Equation (A.6) is analogous to Fick's law for diffusion.

Taking the divergence of (A.6) and using the definition for the flux

$$\vec{F}(\vec{r}) = \int_{4\pi} I(\vec{r}, \hat{s}) \hat{s} d\omega$$

we arrive at the diffusion equation:

$$D \nabla^2 \phi(\vec{r}) - \mu_a \phi(\vec{r}) = 0$$

Note:

In deriving (A.4) from (A.3) the following relation has been used:

$$\int_{4\pi} p(\hat{s}, \hat{s}') \vec{F} \cdot \hat{s}' d\omega' = \vec{F} \cdot \hat{s} \int_{4\pi} p(\hat{s}, \hat{s}') (\hat{s} \cdot \hat{s}') d\omega'$$

which is in general true if $p(\hat{s}, \hat{s}') = p(\hat{s}', \hat{s})$.

In deriving (A.5) from (A.4), the following relations have been used:

$$\int_{4\pi} p(\hat{s}, \hat{s}') d\omega' = 1$$

$$\int_{4\pi} p(\hat{s}, \hat{s}') (\hat{s} \cdot \hat{s}') d\omega' = g$$

$$\int_{4\pi} \hat{s} (\hat{s} \cdot \vec{F}) d\omega = \frac{4\pi}{3} \vec{F}$$

$$\int_{4\pi} \hat{s} (\hat{s} \cdot \nabla (\vec{F} \cdot \hat{s})) d\omega = 0$$

$$\int_{4\pi} \hat{s} d\omega = 0$$

REFERENCES

American Cancer Society 1998 *Cancer Facts & Figures*

Anderson R R and Parish J A 1981 The optics of human skin *J. Invest. Dermatol.* **77** 13-19

Araki K, Furuya Y, Kobayashi M, Matsuura K, Ogata T and Isozaki H 1996 Comparison of mucosal microvasculature between the proximal and distal human colon *J. Electron. Microsc.* **45** 202-206

Arnfield M R, Tulip J and McPhee M S Optical propagation in tissue with anisotropic scattering *IEEE Trans. Biomed. Engin.* **35** 372-381

Beauvoit B, Kitai T and Chance B 1994 Contribution of the mitochondrial compartments of the optical properties of the rat liver: a theoretical and practical approach *Biophys. J.* **67** 2501-2510

Benedek G B and Villars F M H 1974 *Physics, with illustrated examples from medicine and biology* (Reading, MA: Addison Wesley)

Beuthan J, Minet O, Helfmann J, Herrig M and Muller G The spatial variation of refractive index in biological cells *Phys. Med. Biol.* **41** 369-382

Bolin F P, Preuss L E, Taylor C R and Ference R J 1989 Refractive index of some mammalian tissues using a fiber optic cladding method *Appl. Opt.* **28** 2297-2303

Born M and Wolf E 1975 *Principles of optics* (New York: Pergamon Press)

Brennan J F III 1995 *Near infrared raman spectroscopy for human artery histochemistry and histopathology*, (Ph.D. thesis, Massachusetts Institute of Technology)

Brennan J F, Zonios G I, Wang T D, Rava R P, Hayes G B, Dasari R R and Feld M S 1993 Portable laser spectrofluorimeter system for *in vivo* human tissue fluorescence studies *Appl. Spectrosc.* **47** 2081-2086

Campbell I and Dwek R 1984 *Biological Spectroscopy* (Menlo Park, CA: Benjamin/Cummings)

Carr N D, Pullan B R and Schofield P F 1986 Microvascular studies in non-specific inflammatory bowel disease *Gut* **27** 542-549

Cheong W, Prael S A and Welch A J 1990 A review of optical properties of biological tissues *IEEE J. Quant. Elect.* **26** 2166-2185

- Cothren R M, Hayes G B, Kramer J R, Sacks B A, Kittrell C and Feld M S 1986 A multifiber catheter with an optical shield for laser angiography *Lasers Life Sci.* **1** 1-12
- Cothren R M, Sivak M V, Van Dam J, Petras R E, Fitzmaurice M, Crawford J, Wu J, Brennan J F, Rava R P, Manoharan R and Feld M S 1996 Detection of dysplasia at colonoscopy using laser-induced fluorescence: a blinded study *Gastroint. Endosc.* **44** 168-176
- Dayan I, Havlin S and Weiss G H 1992 Photon migration in a two-layer turbid medium: A diffusion analysis *J. Modern Optics* **39** 1567-1582
- Ditchburn R W 1976 *Light* (New York: Academic Press)
- Duck F A 1990 *Physical Properties of Tissue: A Comprehensive Reference Book* (London: Academic Press)
- Duderstadt J J and Hamilton L J 1976 *Nuclear reactor analysis* (New York: Wiley)
- Egan W G and Hilgeman T W 1979 *Optical properties of inhomogeneous materials* (New York: Academic)
- Eide T J 1986 A morphometric analysis of dysplasia in small adenomas of the large intestine *Virchows Arch. A* **410** 119-124
- Farrel T J, Patterson M S and Wilson B C 1992 A diffusion theory model of spatially resolved, steady-state diffuse reflectance for the non-invasive determination of tissue optical properties *Med. Phys.* **19** 879-888
- Fenoglio-Preiser C M, Lantz P E, Davis M, Listrom M B and Rilke F O 1989 *Gastrointestinal Pathology, An atlas and text* (New York: Raven Press)
- Ferdman A G and Yannas I V 1993 Scattering of light from histologic sections: a new method for the analysis of connective tissue *J. Invest. Dermatol.* **100** 710-716
- Feynman R P and Hibbs A R 1965 *Quantum mechanics and path integrals* (New York: McGraw-Hill)
- Groenhuis, R A J, Ferwerda H A, Ten Bosch J J 1983 Scattering and absorption of turbid materials determined from reflection measurements. I. Theory *Appl. Opt.* **22** 2456-2462
- Haggitt R C, Glotzbach R E, Soffer E E and Wruble L D 1985 Prognostic factors in colorectal carcinomas arising in adenomas: implications for lesions removed by endoscopic polypectomy *Gastroent.* **89** 328-336
- Hale G M and Querry M R 1973 Optical constants of water in the 200-nm to 200- μ m wavelength region *Appl. Opt.* **12** 555-563
- Haskell R C, Svaasand L O, Tsay T, Feng T, McAdams M S and Tromberg B J 1994 Boundary conditions for the diffusion equation in radiative transfer *J. Opt. Soc. Am.* **11** 2727-2741
- Henry L G and Greenstein J L 1941 Diffuse radiation in the galaxy *Astrophys. J.* **93** 70-83

- Horrobin D F 1968 *Medical physiology and biochemistry* (London: Edward Arnold) p 384
- Hosmer D W Jr and Lemeshow S 1989 *Applied logistic regression* (New York: John Wiley)
- Hull E L and Foster T H 1997 Noninvasive near-infrared hemoglobin spectroscopy for *in vivo* monitoring of tumor oxygenation and response to oxygen modifiers *SPIE Proc.* **2979** 355-364
- Ikeda M and Matsushita A 1980 Reflectance of rat brain structures mapped by an optical fiber technique *J. Neurosci. Methods* **2** 9-17
- Ishimaru A 1978 *Wave propagation and scattering in random media* (Orlando: Academic Press)
- Jacques S L, Alter C A and Prahl S A 1987 Angular dependence of He-Ne laser light by human dermis *Lasers Life Sci.* **1** 309-333
- Jain R K 1988 Determinant of tumor blood flow: a review *Cancer Res.* **48** 2641-2658
- Kapadia C R, Cutruzolla F W, O'Brian K M, Stetz M L, Enriquez R and Deckelbaum L I 1990 LIF spectroscopy of human colonic mucosa *Gastroent.* **99** 150-157
- Kienle A, Lilge L, Patterson M S, Hibst R, Steiner R and Wilson B C Spatially resolved absolute diffuse reflectance measurements for noninvasive determination of the optical scattering and absorption coefficients of biological tissue *Appl. Opt.* **35** 2304-2314
- Knoefel W T, Kollias N, Rattner D W, Nishioka N S and Warshaw A L 1996 Reflectance spectroscopy of pancreatic microcirculation *J. Appl. Physiol.* **80** 116-123
- Kortum G 1969 *Reflectance spectroscopy. Principles, methods, applications.* (New York: Springer)
- Kubelka P 1948 New contributions to the optics of intensely light scattering material. Part I *J. Opt. Soc. Am.* **38** 448-457
- Kumar G and Schmitt J M 1997 Optimal probe geometry for near-infrared spectroscopy of biological tissue *Appl. Opt.* **36** 2286-2293
- Lekner J and Dorf M C 1988 Why some things are darker when wet *Appl. Opt.* **27** 1278-1280
- Leonard D W and Meek K M 1997 Refractive indices of the collagen fibrils and extrafibrillar material of the corneal stroma *Biophys. J.* **72** 1382-1387
- Liu H, Boas D A, Zhang Y, Yodh A G and Chance B 1995 Determination of optical properties and blood oxygenation in tissue using continuous NIR light *Phys. Med. Biol.* **40** 1983-1993
- Loh C S, Vernon D, MacRobert A J, bedwell J, Bown S G and Brown S B 1993 Endogenous porphyrin distribution induced by 5-aminolaevulinic acid in tissue layers of the gastrointestinal tract *J. Photochem. Photobiol. B* **20** 47-54

- Manoharan R, Wang Y and Feld M S 1996 Histochemical analysis of biological tissues using Raman spectroscopy *Spectrochimica Acta A* **52** 215-249
- Marchesini R, Brambilla M, Clemente C, Maniezzo M, Sichirollo A E, Testori A, Venturoli D R and Cascinelli N 1991 *In vivo* spectrophotometric evaluation of neoplastic and non-neoplastic skin pigmented lesions-I reflectance measurements *Photochem. Photobiol.* **53** 77-84
- Marchesini R, Pignoli E, Tomatis S, Fumagalli S, Sichirollo A E, Di Palma S, Dal Fante M, Spinelli P, Croce A C and Bottioli G 1994 *Ex vivo* optical properties of human colon tissue *Lasers Surg. Med.* **15** 351-357
- Marx E and Mulholland G W 1983 Size and refractive index determination of single polystyrene spheres *J. Res. Natl. Bur. Stand.* **88** 321-338
- Meyer R A 1979 Light scattering from biological cells: dependence of backscatter radiation on membrane thickness and refractive index *Appl. Opt.* **28** 585-588
- Ming S C and Goldman H 1992 *Pathology of the Gastrointestinal Tract* (Philadelphia, PA: Saunders Co)
- Morse P M and Feshbach H 1953 *Methods of Theoretical Physics* (New York: McGraw-Hill) p 184
- Mourant J R, Bigio I J, Boyer J, Conn R L, Johnson T and Shimada T 1995 Spectroscopic diagnosis of bladder cancer with elastic light scattering *Lasers Surg. Med.* **17** 350-357
- Mourant J R, Bigio I J, Boyer J, Johnson T M and Lacey J 1996 Elastic scattering spectroscopy as a diagnostic for differentiating pathologies in the gastrointestinal tract: preliminary testing *J. Biomed. Opt.* **1** 192-199
- Panjehpour M, Overholt B F, Vo-Dinh T Haggitt R C, Edwards D H and Buckley III F P 1996 Endoscopic fluorescence detection of high-grade dysplasia in Barrett's esophagus *Gastroenterol.* **111** 93-101
- Perelman L T, Backman V, Wallace M, Zonios G, Manoharan R, Nusrat A, Shields S, Seiler M, Lima C, Hamano T, Itzkan I, Van Dam J, Crawford J M and Feld M S 1998 Observation of periodic fine structure in reflectance from biological tissue: a new technique for measuring nuclear size distribution *Phys. Rev. Lett.* **80** 627-630
- Perelman L T, Winn J N, Wu J, Dasari R R and Feld M S 1997 Photon migration of near-diffusive photons in turbid media: a Lagrangian-based approach *J. Opt. Soc. Am.* **14** 224-229
- Perelman L T, Wu J, Itzkan I and Feld M S 1994 Photon migration in turbid media using path integrals *Phys. Rev. Lett.* **72** 1341-1344
- Reif F 1965 *Fundamentals of statistical and thermal physics* (New York: McGraw Hill)
- Robey-Cafferty S S, el-Naggar A K, Grignon D J, Cleary K R and Ro J Y 1990 Histologic parameters and DNA ploidy as predictors of survival in stage B adenocarcinoma of colon and rectum *Mod. Pathol.* **3** 261-266

- Sato N, Takenobu K, Motoaki S, Sunao K, Hiroshi A and Hagihara B 1979 Measurement of hemoperfusion and oxygen sufficiency in gastric mucosa *in vivo Gastroent.* **76** 814-819
- Schmitt J M 1991 Simple photon diffusion analysis of the effects of multiple scattering on pulse oximetry *IEEE Trans. Biomed. Engin.* **38** 1194-1203
- Schmitt J M and Kumar G 1996 Turbulent nature of refractive-index variations in biological tissue *Opt. Lett.* **21** 1310-1312
- Schomacker K T, Frisoli K J, Compton C C, Flotte T J, Richter J M, Nishioka N S and Deutsch T F 1992 Ultraviolet laser-induced fluorescence of colonic tissue: basic biology and diagnostic potential *Lasers Surg. Med.* **12** 63-78
- Skinner S A and O'Brien P E 1996 The microvascular structure of the normal colon in rats and humans *J. Surg. Res.* **61** 482-490
- Skinner S A, Frydman G M and O'Brien P E 1995 Microvascular structure of benign and malignant tumors of the colon in humans *Digest. Dis. Sci.* **40** 373-384
- Statacorp. 1997 Stata statistical software: release 5.0 (College Station TX: Stata Corporation)
- Stryer L 1995 *Biochemistry* (New York: Freeman)
- Swathi P S, Tong T W and Cunnington G R 1987 Reflectance of two-layer composite porous media with linear-anisotropic scattering *J. Quant. Spectrosc. Radiat. Transfer* **38** 273-279
- Takatani S and Graham M 1979 Theoretical analysis of diffuse reflectance from a two-layer tissue model *IEEE Trans. Biomed. Engin.* **26** 656-664
- Takatani S and Ling Jian 1994 Optical oximetry sensors for whole blood and tissue *IEEE Eng. Med. Biol.* **3** 347-357
- Tearney G J, Brezinski M E, Southern J F, Bouma B E, Hee M R and Fujimoto J G 1995 Determination of the refractive index of highly scattering human tissue by optical coherence tomography *Opt. Lett.* **20** 2258-2260
- Thomson H J, Busuttil A, Eastwood M A, Smith N A and Elton R A 1986 The submucosa of the human colon *J. Ultr. Mol. Struct. Res.* **96** 22-30
- Tipoe G L and White F H 1995 Blood vessel morphometry in human colorectal lesions *Histol. Histopathol.* **10** 589-596
- Tsujii M, Kawano S, Tsuji S, Kobayashi I, Takei Y, Nagano K, Fusamoto H, Kamada T, Ogihara T and Sato N 1995 Colonic mucosal hemodynamics and tissue oxygenation in patients with ulcerative colitis: Investigation by organ reflectance spectrophotometry *J. Gastroenterol.* **30** 183-188
- van Assendelft O W 1970 *Spectrophotometry of Haemoglobin Derivatives* (Springfield, Ill.: C C Thomas)

- Van Gemert M J C and Star W M 1987 Relations between the Kubelka-Munk and the transport equation models for anisotropic scattering *Lasers Life Sci.* **1** 287-298
- Van Gemert M J C, Jacques S L, Sterenborg H J C M and Star W M 1989 Skin optics *IEEE Trans. Biomed. Eng.* **36** 1195-1201
- Vaupel P 1996 Oxygen transport in tumors: characteristics and clinical implications *Adv. Exp. Med. Biol.* **388** 341-351
- Wang L, Jacques S L, Zheng L 1995 MCML-Monte Carlo modeling of light transport in multi-layered tissues *Comp. Meth. Progr. Biomed.* **47** 131-146
- Wang T D 1996 *Fluorescence endoscopic imaging system for detection of colonic adenomas*, Ph.D. thesis, Department of Health Sciences and Technology, Massachusetts Institute of Technology
- Wilson B C and Adam G 1983 A Monte Carlo model for the absorption and flux distributions of light in tissue *Med. Phys.* **10** 824-830
- Wiscombe W J 1979 Mie scattering calculations: Advances in technique and fast vector speed computer codes, NCAR Technical Note, NCAR/TN-140+STR, National Center for Atmospheric Research, Boulder, Colorado, June 1979
- Woodward H Q and White D R 1986 The composition of body tissues *Br. J. Radiol.* **59** 1209-1219
- Wu J, Feld M S and Rava R P 1993b Analytical model for extracting intrinsic fluorescence in turbid media *Appl. Opt.* **32** 3585-3595
- Wu J, Partovi F, Feld M S and Rava R P 1993a Diffuse reflectance from turbid media: an analytical model of photon migration *Appl. Opt.* **32** 1115-1121
- Zangaro R A, Silveira Jr L, Manoharan R, Zonios G, Itzkan I, Dasari R R, Van Dam J and Feld M S 1996 Rapid multiexcitation fluorescence spectroscopy system for *in vivo* tissue diagnosis *Appl. Opt.* **35** 5211-5219
- Zerull R 1976 Scattering measurements of dielectric and absorbing nonspherical particles *Beitr. Phys. Atmos.* **49** 166-188
- Zonios G I, Cothren R M, Arendt J T, Wu J, Van Dam J, Crawford J M, Manoharan R and Feld M S 1996 Morphological model of human colon tissue fluorescence *IEEE Trans. Biomed. Eng.* **43** 113-122